UNIVERSITY OF CALIFORNIA

Los Angeles

Isotopic and Trace Element Investigations of Crustal Processes

A dissertation submitted in partial satisfaction of the

requirements for the degree Doctor of Philosophy

in Geology

Heather Margaret Kirkpatrick

2022

ABSTRACT OF THE DISSERTATION

Isotopic and Trace Element Investigations of Crustal Processes

by

Heather Margaret Kirkpatrick

Doctor of Philosophy in Geology, 2022

University of California, Los Angeles

Professor T. Mark Harrison, Chair

Knowledge of crustal architecture, and the distribution of rock types within, did not by itself provide geologists unambiguous evidence of its evolution. It was not until the advent of modern geochemical and petrologic methods in the 1960s that the mechanisms and timescales of continental crustal evolution began to be delimited. Chapter 1 of this thesis introduces the historical background of modern geological studies and places my three principal investigations in that broader context. These studies range from understanding interactions between climate, rock strength, topographic form, and erosion to unraveling the controls of magmatic processes which control trace element partitioning.

Chapter 2 investigates how erosion rate, topography, and rock properties control the landform evolution in eastern Tibet. Tectonic deformation can influence spatiotemporal patterns of erosion by changing both base-level and the mechanical state of bedrock. Although base-level change and the resulting erosion are well understood, the impact of tectonic damage on bedrock erodibility has rarely been quantified. Eastern Tibet, a tectonically active region with diverse lithologies and multiple active fault zones, provides a suitable field site to understand how tectonic deformation controls erosion and topography. In this study, I quantified erosion coefficients using the relationship between millennial erosion rates and the corresponding channel steepness. This work shows a two-fold increase in erosion coefficients between basins within 15 km of major faults and those beyond 15 km, suggesting that tectonic deformation through seismic shaking and rock damage significantly affects eastern Tibet erosion and topography. It demonstrates a field-based, quantitative relationship between rock erodibility and fault damage, which has important implications for improving landscape evolution models.

In Chapter 3, I investigate the influences of Zr stable isotope variations in samples from the Peninsular Ranges Batholith, southern California. Zr isotopic measurements were undertaken on zircon, titanite, biotite, amphibole, and whole rocks from the La Posta pluton together with trace element analyses and U-Pb ages to understand the controls on Zr isotope fractionation in igneous rocks, including temperature, co-crystallizing phases, and kinetic effects. Middle rare earth element (MREE) depletions are present that could indicate that a co- or formerly crystallizing phase impacted the subsequent Zr isotope composition of zircon. Large (>0.6 ‰) Zr isotope fractionations (expressed as $\delta^{94/90}$Zr) were found between titanite and zircon forming at approximately the same temperature. Using equilibrium fractionation factors calculated from ionic and ab initio models, we inferred the controls on Zr isotope evolution to include

crystallization order, with titanite fractionation resulting in isotopically lighter melt and zircon fractionation resulting in isotopically heavier melt. While these models of Zr fractionation can explain $\delta^{94/90}$Zr variations of up to ~1.5‰, crystallization order, temperature and presence of co-crystallizing phases do not explain all aspects of the intracrystalline Zr isotopic distribution in zircons in the La Posta pluton. Without additional constraints, Zr stable isotopic investigations of zircons are not yet unambiguous proxies of magmatic evolution.

While the Ti-in-Quartz thermobarometer is one of the most widely used trace element methods in the geosciences to simultaneously obtain temperature and pressure information, recent studies have called its accuracy into question. In Chapter 4, I present six new experimental results and review the critiques of this thermobarometer. With regard to the latter, the effects of secondary fluorescence, supersaturation, and quenching rates appear to provide first order explanations for the differences in the varied results. My results broadly agree with the earlier calibrations but further experimental and modeling of the many controls on Ti concentrations in quartz appear warranted.

The dissertation of Heather Margaret Kirkpatrick is approved.

Craig Manning

Edward D. Young

Seulgi Moon

T. Mark Harrison, Committee Chair

University of California, Los Angeles

2022

To those who have helped me along the way, thank you

Table of Contents

ABSTRACT OF THE DISSERTATION ii
Committee Page. v
Dedication vi
Table of Contents vii
List of Figures and Tables xi
Acknowledgements xvii
Curriculum Vita xix
Chapter 1: Introduction 1
1.1 Background 1
1.2 Trace element chemistry 4
1.3 Models 5
1.4 References: 8
Chapter 2: Impact of fault damage on eastern Tibet topography 13
2.1 Introduction 13
2.1.1 Geologic Background 14
2.2 Methods 14
2.2.1 Determination of Erosion Rates 14
2.2.2 Quantification of topographic, geologic, climatic, and ecologic parameters 16
2.2.3 Calculating controls on erosional coefficients 17
2.2.3.1 Calculating the erosional coefficient 17
2.2.3.2 Calculating lithologic distributions and understanding rock strength 18
2.2.3.3 Calculating other potential controls on erosional coefficients 20
2.2.4 Fault compilation and impacts from earthquakes 21
2.2.4.1 Active and inactive faults in eastern Tibet 21
2.2.4.2 Distance to major faults calculation 23
2.2.4.3 Determining the impact from earthquakes 23
2.3 Results 25
2.3.1 Erosion rates 25
2.3.2 Topographic metric and lithology results 25
2.4 Discussion and conclusions 27

2.4.1 Future work and importance 29
2.5 Figure Captions 31
2.6 References 34
Chapter 3: Temperature and co-crystallization effects on Zr isotopes: A case study of the La Posta igneous complex 44
3.1 Introduction 44
3.2. The La Posta plutonic suite 46
3.3. Zr distribution in granitoid rocks 47
3.4. Methods 48
3.4.1 Sample collection and preparation 48
3.4.2 Zr isotopic measurements by SIMS 49
3.4.3 In situ trace elements analyses 50
3.4.4 In situ U-Pb analyses 51
3.4.5 Zr isotope analyses by double-spike MC-ICPMS: 51
3.4.6 Modeling the impact of co-crystallizing phases on zircon isotopic composition 54
3.5. Results 55
3.5.1 In situ standards 55
3.5.2 Zr isotopic compositions 55
3.5.3 Zircon trace elements in the La Posta Pluton 57
3.5.4 Zircon U-Pb ages 58
3.5.5 Petrography 59
3.6. Discussion 60
3.6.1 Zircon-melt fractionation factors 60
3.6.2 Titanite-melt fractionation factors 62
3.6.3 Modeling melt evolution 64
3.6.4 Difference between fractionation factors 65
3.6.5 Spatial effects 66
3.6.6 Potential impacts of kinetic mass dependent effects 69
3.6.7 Zr isotopic fractionation between zircon and melt 70
3.6.8 Impact of temperature 72
3.6.9 Impact of co-crystallizing phases 73

3.6.10 Modeling the impact of Zr in co-crystallizing phases and impact of crystallization order 74
3.6.11 Combined temperature and co-crystallization impacts on zircon profiles 76
3.6.12 Relationship between zircon and titanite 77
3.6.13 Applications to understanding magmatic evolution 79
3.6.14 Applications to detrital studies and future directions 80
3.7. Summary 81
3.8 Figures 82
3.9 References 97
Chapter 4: Reevaluating the Ti-in-quartz thermobarometer 110
4.1 Introduction and background 110
4.1.1 Previous studies 111
4.2 Thermodynamics of Ti substitution in the quartz lattice 112
4.3 Methods 113
4.3.1 Experiments 113
4.3.2 Characterization and measurements 114
4.3.3 Calculation of Ti concentration variability in a slowly cooled system 116
4.3.4. Choice of glass standard concentrations 116
4.4 Results 117
4.5 Discussion 117
4.5.1 Disequilibrium 118
4.5.1.1 Ti solubility in melt 118
4.5.1.3 Quartz and rutile supersaturation 119
4.5.2 The impact of cooling on Ti solubility in quartz 121
4.5.3 Secondary fluorescence 123
4.5.4. Ti-in-quartz calibration 126
4.6. Conclusions 127
4.7 Figures 129
4.8 Tables 135
4.9 References 138
Chapter 5: Summary 143
5.1. Using models to understand crustal processes 143

5.2 References 146
Appendix A for Chapter 2: Impact of fault damage on eastern Tibet Topography 147
2.7. Quantification of Erosion Coefficients and Rate Constants 147
2.7.1. Calculating channel steepness 149
2.8 Statistical Analysis 150
2.9 Figures 156
2.10 References: 168
Appendix B for Chapter 3: Temperature and co-crystallization effects on Zr isotopes: A case study of the La Posta igneous complex 171

List of Figures and Tables

Figure 2.1. Maps of eastern Tibet showing elevation with sampled basins color-coded by (A) ^{10}Be-derived erosion rates and (B) erosion coefficients, (C) local relief within a 1 km radius circular moving window, and (D) lithology from Hartmann and Moosdorf (2012). The box in the inset map in A shows our study area. Major active and inactive faults are shown with solid brown and dashed blue lines, respectively. Brown dashed lines show active faults for which the last activity is unclear. Full names and detailed information about our fault compilation are in the Data Repository. Locations of Songpan (SP), Ganze (GZ), and Chengdu are shown with blue dots in B. Mountain range names are shown in C. 31

Figure 2.2. Erosion rates versus (A) slope, (B) local relief with a 1 km radius range, and C, D) k_{sn} color-coded by (C) distance to major faults and (D) dominant lithologic groups. Blue, cyan, and salmon circles in D represent small basins dominated by siliciclastic sedimentary, mixed composition sedimentary, and plutonic rocks, respectively. White circles show all other basins, including those with areas >200 km^2. Long dash lines show the minimum and maximum slope ranges for the linear fit. At similar values of topographic metrics, basins near faults have higher erosion rates than those farther from faults..... 32

Figure 2.3. (A) Erosion coefficient versus distance to major faults, color-coded for small basins dominated by different lithologic groups. (B) Boxplots showing erosion coefficient ranges from different lithologies grouped by distance to major faults (D_{mf}). All basins, small basins (area <200 km^2), and small basins dominated by siliciclastic sedimentary, mixed composition sedimentary, and plutonic rocks are shown in white, gray, blue, cyan, and salmon, respectively. The line, box, and circle show the extent within 99.3%, the 25th and 75th percentiles, and the median, respectively. On average, erosion coefficients are ~2 times higher for basins with $D_{mf} \leq 15$ km than those >15 km. 33

Figure 3.1: Geologic map of the La Posta region of the Peninsular Ranges batholith with an inset map showing the location in relation to state lines in the southwestern United States. Geologic map and units are from Todd (2004). The green dots show sample locations. From left to right, the units are hornblende-biotite facies (LP3 and LP7), large-biotite facies (LP1), small-biotite facies (LP2 and LP5), and muscovite-biotite facies (LP6). For reference, the light pink unit is the La Posta pluton. 82

Figure 3.2: Petrographic images of thin sections from the small biotite facies of the La Posta pluton. Top images show plane polarized light images and bottom images show cross-polarized light images of samples. Within the black boxes, the images are showing the same area of a thin section (apatite has first order grey birefringence; zircon has 3rd order birefringence). The distribution of zircon is inconsistent with the 'pileup' model. 83

Figure 3.3: Images showing the mineralogy of sample LP7 (A) and LP5 (B and C) from the hornblende-biotite and small biotite facies of the La Posta pluton, respectively. A1, B1, C1) Backscatter electron images of the studied area with some mineralogy labeled. A2 and 3) show elemental compositions with Zr-Ti-Ca (A2) and Mg-K-Ca (A3) as red-green-blue. Of note, the light blue color and pink in (B) shows titanite and apatite, respectively. P and Zr emit similar x-

rays, so these two elements often show up on the others' patterns. The mineral showing red and green in (A3) is biotite. Chlorite is shown in red. Green shows K-rich feldspar, and dark blue shows titanite and apatite. Na-rich feldspar is black-blue. A1, 2, and 3 show the same field of view. B2) and 3) show Zr-Ti-Ca and Mg-K-Ca, respectively, as red-green-blue. In (B2), light blue shows titanite, green shows ilmenite, pink shows apatite, and red shows zircon. In (B3), blue shows titanite and apatite and red-green shows biotite. C2) shows elemental compositions with Fe-Ca-Zr as red-green-blue. Red shows ilmenite and green shows titanite. Bluish-green shows apatite. ... 84

Figure 3.4: Figure shows all Zr isotope analyses in this study: zircons (averaged from all analyses for each rock, yellow), whole rock (cyan), amphibole (blue), titanite/sphene (green), and biotite (pink). Error bars on zircon analyses, which were conducted by SIMS, are 1 s.d. Error bars for other measurements, which were conducted by DS-MC-ICPMS, are smaller than the plotted symbols. 85

Figure 3.5: Figure shows all Zr isotope analyses of zircon in this study vs. whole rock SiO_2: the zircon with the heaviest Zr isotopic composition (green circle), zircon with the lightest Zr isotopic composition (blue circle), and all zircons measured for each rock (grey cross). Best fit line of each rocks' minimum isotopic composition vs. whole rock SiO_2 shown with a dot-dash line. 86

Figure 3.6: The bottom image shows a titanite-rich portion of the LP13 outcrop, close to the LP2 sampling location. The burgundy dashed box in the lower image shows the location of the upper image. The vertical measurement of each square on the left side corresponds to 1 cm. 87

Figure 3.7: Isotopic profiles of grains from the La Posta pluton. 0 on the x-axis corresponds to the core of the grain, and the dotted black lines show the edges of grains. Cathodoluminescence images of these grains can be found in the Supplementary Material. Error bars are showing 1 s.d. The width of an analytical spot is less than the horizontal length of a spot. 88

Figure 3.8: Cathodoluminescence image of LP2 grain 1 with Zr isotopic analyses, trace element (*ims*1290), trace element (*ims*1270), and U-Pb spots shown in red, blue, light blue, and green, respectively. U-Pb analyses from the November and December 2020 sessions are shown with thicker and thinner dotted lines, respectively. White numbers adjacent to spots show analysis numbers in Table S5. This grain contains an inherited core which is Proterozoic in age surrounded by Cretaceous growth. 89

Figure 3.9: Gd/Gd* vs. Ti-in-zircon temperature for all zircons analyzed. Different units within the zoned La Posta pluton are shown in different colors. Generally, less silicic rocks have both lower Gd/Gd* and lower Ti-in-zircon temperatures showing indicating a higher degree of titanite fractionation prior to zircon crystallization. The heatmap shows an increase in Ti-in-zircon temperature with increasing Gd/Gd*. Titanite depletes MREE in glasses (Colombini et al., 2011), and Gd/Gd* is used to represent that depletion here. Square boxes represent analyses made using the *ims*1270 and circle boxes show analyses made using the *ims*1290. 90

Figure 3.10: U-Pb ages vs. Zr stable isotope values of zircons from the La Posta pluton with different colors showing different samples. All analyses contain >95% $^{206}Pb^*$ and are within 30% of concordance. 91

Figure 3.11: A-D show relationships as modeled using the ionic model (Young et al., 2015); E-H show relationships modeled using force constants calculated by Chen et al. (2020); A, B, C. E, F, G) Modeled zircon isotope profiles showing the impacts of constant vs. changing T on Zr isotope evolution for a tabular zircon that we model as a rectangle. B and F) shows a system where all three zircon axis are the same length (x = y = z) and C and G) shows a system where x = y and z= 5x. D and H) shows a grain where z = 200 µm and x = y = 40 µm along with the approximate size of LA-ICPMS and SIMS beams in blue and green, respectively. Red and black lines show the isotopic composition of melt and zircon, respectively and solid and dotted lines show the isotopic trajectory of a system with a constantly changing T and an isothermal system, respectively..... 92

Figure 3.12: Modeled evolution curves if only a single phase is crystallizing. A) shows isotope evolution of zircon if zircon crystallizes as a result of Rayleigh fractionation and B) shows the resultant melt evolution. C) shows the Zr isotopic evolution of sphene if it crystallizes alone and D) shows the isotopic evolution of the melt as a result of titanite crystallization. All profiles show a 100 K change (1006 → 906 K). In the upper two subfigures, zircon is the only phase crystallizing. In the bottom two, titanite is the only phase crystallizing. 94

Figure 3.13: Influence of co-crystallizing phases on isotope profiles shown through fraction of Zr remaining (f) vs. $\delta^{94/90}$Zr (‰) for a modeled zircon for a system with a constant change in temperature. Red, blue, and black lines show the isotopic composition of melt, titanite, and zircon, respectively. Figures A-C show fractionation factors calculated using the ionic model. Figures D-F show profiles calculated using fractionation factors calculated using values from Chen et al. (2020). 95

Figure 3.14: Fraction of Zr remaining (f) vs. $\delta^{94/90}$Zr (‰) for a modeled zircon for two systems with 50% of Zr in zircon and 50% of Zr in titanite, both with a constant change in T. Figures A and C show all Zr partitioning into titanite until $f = 0.75$ followed by co-crystallization of titanite and zircon where 1/ 3 of Zr partitions into titanite and 2/3 partitions into zircon. In Figures B and D, Zr partitions into titanite until $f = 0.5$ followed by Zr partitioning into zircon until $f = 0$. Red, blue, and black lines show the isotopic composition of melt, titanite, and zircon, respectively. Figures A-B show fractionation factors calculated using the ionic model. Figures C-D show profiles calculated using fractionation factors calculated using values from Chen et al. (2020). 96

Figure 4.1: Backscatter electron images of 6 of the run products with row 1 showing experiments performed at 10 kbar and row 2 showing those performed at ~15 kbar. Experimental temperature increases from the left to the right. The major phase in all of these images is quartz with some also showing zircon and rutile. The dark background is epoxy. 129

Figure 4.2: Comparison of measured and recalculated Ti concentrations in quartz. The three regression lines show relationships between temperature and concentration for each pressure regime with at least three measurements. Measurements made in this study are in large circles and recalculated concentrations are shown in small circles. The upper right side shows what pressure each color corresponds to. Vertical bars represent 1 s.e. 130

Figure 4.3: Comparison of Ti-in-quartz measurements between multiple sessions based on sample and session. Green, aqua, blue, and grey represent the 2022, 2018, 2017, and previously published concentrations, respectively. 131

Figure 4.4: Relationship between original concentrations and recalculated concentrations. 132

Figure 4.5: Calculated change in concentration with monotonic cooling from 800 °C to 25 °C over 2 hours (first 80 minutes shown) and 1 kbar to 1 bar over 15 minutes. Calculation used the calibration of Thomas et al. (2010). Note the rapid decrease in composition over the course of the first 30 minutes. 133

Figure 4.6: Thin lines represent the calibration proposed by Osborne et al. (2022). Thin lines show linear regressions from this study. 134

Table 4.1: List of newly grown experiments with temperature, pressure, name, and run duration. 135

Table 4.2: Experimental run products used in this calibration with pressure, temperature, Ti concentration, and 1 s.e. of Ti concentrations. Samples in italics are reanalyzed run products from Thomas et al. (2010) or Thomas et al. (2015)..... 136

Table 4.3: Calculations of Ti concentrations in experimental run products using a glass-only calibration, QTiP-only calibration, and a calibration with both glass and QTiP standards. 137

Figure 2.4. Elevation map of the Min Shan area with the 11 new sample collection sites and basin outlines from this study. Sample names are shown in black, channel networks are shown in blue, and sample collection sites are shown with green dots. Note that all samples except for ET05, 08, 10-12 have nested basins. Erosion rates from basins which are not from nested basins are shown on top of those which are from nested basins. 156

Figure 2.5. Maps showing (A) slope, (B) mean annual precipitation from Bookhagen and Burbank (2010), and (C) channel steepness shown for channel sections with drainage areas larger than 10 km^2 in eastern Tibet, and (D) peak ground acceleration (*PGA*) from the 2008 Wenchuan earthquake (from USGS ShakeMap v4). Black outlines represent all basins compiled from previous studies and measured in this study. A white box in (A) represents the area shown in Fig. 2.4..... 157

Figure 2.6. Maps showing basin-averaged (A) slope, (B) mean annual precipitation from Bookhagen and Burbank (2010), and (C) channel steepness from the integral method in eastern Tibet. (D) Elevation map with earthquakes from M_w 5 to 8 with larger circles showing higher magnitude earthquakes. Earthquakes before the 2008 Wenchuan earthquake are shown with green circles and those after the 2008 Wenchuan earthquake are shown with red circles. Earthquakes shown in the compilation occurred from 1970 through July 2018. Earthquakes were retrieved from www.iris.edu. 158

Figure 2.7. Scatter plots (A, C, E, G, I, K, M, O, Q, S) and box plots (B, D, F, H, J, L, N, P, R, T) showing how erosion coefficients vary with (A, B, E, F, I, J, M, N, Q, R) the distance to major faults and (C, D, G, H, K, L, O, P, S, T) distance to major active faults for A-D) all basins, E-H) small basins with area < 200 km^2, and small basins dominated by I-L) siliciclastic sedimentary

rock, M-P) mixed composition sedimentary rock, and Q-T) plutonic rock. All basins, small basins, and small basins dominated by siliciclastic sedimentary, mixed composition sedimentary, and plutonic rocks are shown in circles with white, gray, blue, cyan, and salmon colors, respectively in the scatter plots. The top and bottom of the blue sides of the box plots show the 25th and 75th percentiles, respectively. The central red mark in the box shows the median. The whiskers show the extent of data within 99.3%, and red crosses show outliers. 159

Figure 2.8. Scatter plots showing erosion coefficient vs. (A) erosion rate and (B) channel steepness (k_{sn}), color-coded for distance to major faults, and distance to major faults vs (C) erosion rate and (D) channel steepness (k_{sn}), color-coded for erosion coefficient. The control of distance to major faults on erosion coefficients is observed in a wide range of erosion rates and k_{sn} values. 161

Figure 2.9. Relationships between basin-averaged erosion coefficient and (A) basin-averaged mean annual precipitation rates, (B) basin-averaged *NDVI*, and (C) peak ground acceleration (*PGA*) from the 2008 Wenchuan earthquake from all basins in this study. The colors represent distance to major faults. 162

Figure 2.10. Plots of (A, D) erosion rates vs. the product of discharge and slope and (B,C,E,F) erosion coefficients vs. distance to major faults, color-coded for small basins dominated by different lithologic groups. Erosion coefficients K_{ss} and K_{sp} are based on river incision models assuming A-C) shear stress and D-F) stream power, respectively. Symbols are the same as in Fig. 2.3..... 163

Figure 2.11. A,C) Erosion coefficient versus distance to major faults, color-coded for small basins dominated by different lithologic groups. B,D) Boxplots showing erosion coefficient ranges from different lithologies separated by distances to major faults. The plots show results from A,B) samples collected before the 2008 Wenchuan earthquake and C,D) samples collected before and after the 2008 Wenchuan earthquake but outside of the severe shaking range (*PGA* < 0.34 g). Symbols are the same as in Fig. 2.3. In both cases, we see that both the all basins grouping and the small basins grouping for $D_{mf} \leq 15$ km have ~1.5 to 1.8 times higher erosion coefficients than those basins with $D_{mf} > 15$ km. 164

Figure 2.12. Conceptual diagram of fault core and damage zones and idealized topographic expression. Rock strength increase from fault core zones (e.g., gauge, cataclasite) to fault damage zones (e.g., jointed or fractured rocks) to unfractured intact bedrock. The topographic slope near the fault zone is gentler due to greater rock damage. Map not to scale. 165

Figure 2.13. Lithology of the northeastern Longmen Shan and Min Shan area (Hartmann and Moosdorf, 2012) with the locations of Schmidt hammer measurements shown in black dots. The numbers in white are the average Schmidt hammer rebound values, and those in parenthesis show two standard deviation values. Brown lines show the active faults and blue lines shown inactive faults compiled in this study. The blue dot shows the location of the city of Songpan. 166

Figure 2.14. Boxplots showing the ranges of Schmidt hammer rebound values (*H*-values) for 8 sites. The top and bottom of the blue sides of the box show the 25th and 75th percentiles, respectively. The central red mark shows the median. The whiskers show the extent of data within 99.3%, and red crosses show outliers. 167

Figure 3.15: A-D show relationships as modeled using force constants calculated in Méheut et al. (2021); E-H show relationships modeled using the temperature regression shown in Guo et al. (2020); A, B, C. E, F, G) Modeled zircon isotope profiles showing the impacts of constant vs. changing T on Zr isotope evolution for a tabular zircon that we model as a rectangle. B and F) shows a system where all three zircon axis are the same length (x = y = z) and C and G) shows a system where x = y and z= 5x. D and H) shows a grain where z = 200 µm and x = y = 40 µm along with the approximate size of LA-ICPMS and SIMS beams in blue and green, respectively. Red and black lines show the isotopic composition of melt and zircon, respectively and solid and dotted lines show the isotopic trajectory of a system with a constantly changing T and an isothermal system, respectively. 171

Figure 3.16: Fraction of Zr remaining (f) vs. $\delta^{94/90}$Zr (‰) for a modeled zircon where α_{Ti}=0.7 (black) and α_{Ti}=1.0 (blue) for constant (solid lines) vs. a constantly changing T (dot-dash lines). 173

Figure 3.17: A physical model showing the two geometries of our hypothetical crystals. 174

Figure 3.18: Schematic showing the impact of a diffusive boundary layer forming on crystal composition. 175

Acknowledgements

First, thank you to my advisor, Mark Harrison, for allowing me the freedom to explore my many scientific interests during graduate school. Seulgi Moon, thank you for teaching me how to be careful and pay attention to detail. Craig Manning, Ed Young, and An Yin, thank you for your insightful comments while serving on my committees and for answering my questions. Beth Ann Bell, your friendship has made graduate school orders of magnitude better; I aspire to have your level of intelligence, kindness, and critical eye. Ming-Chang Liu and Kevin McKeegan, thank you for all your time spent tuning the ion probe and answering my ion probe questions. Lvcian Vltava, thank you for not only keeping the ion probes functional, but also for all the work you do to make the machines better. Dustin Trail, thank you for mentoring me since my 2nd year, listening to my ideas, and for performing the experiments in the fourth chapter. I have also had excellent collaborators during graduate school including Ben Weiss, Caué Borlina, Francois Tissot, Tamara Carley, and Mauricio Ibañez-Mejia, so thank you to them! Carolina Lithgow-Bertelloni, thank you for encouraging me, having an open door, and being an excellent example for me and other young scientists. Thanks to the EPSS administrative staff, especially Eric Wessenauer, Lauri Holbrook, and Rick Fort.

I have also benefited from many other scientists and friends while at UCLA. Thank you to former and current members of the ion probe group including Melanie Barboni, Patrick Boehnke, Rita Economos, Haolan Tang, Nozomi Matsuda, Emilie Dunham, Andreas Hertwig, Ellen Alexander, and Andrew Parisi. In addition, thank you to current and former members of the Geomorphology group including Jessica Lin, Kevin Shao, Justin Higa, Gen Li, Nathan Brown, and Marina Argueta. I have also had the opportunity to work with hundreds of undergraduates during my time at UCLA who have taught me to be a better teacher and science communicator, so thank you to them. Nicole Jewell and Amanda Hunt, thank you for all your hard work on Mt. Alfred and for allowing me to mentor you. Beyond my research groups, thank you to the fantastic group of graduate students who I have spent time with. Krista Sawchuk, Ashley Schoenfeld, Ashna Aggarwhal, Valeria Jaramillo-Hernandez, Ariel Graykowski, Colin Wilkins, Akash Gupta, Sebastian Kraus, Abijah Simon, Daniel Fineman, Mojhgan Haghnegahdar, Leslie Insixiengmay, Tyler Powell, Elisha Jhoti, Taylor Dorn, Jordan Breztfelder, Amanda Garcia, Ky Hughson, Sarah Marcum, Will Meisner, Allie Doyle, and Lauren Tafla, thank you for your friendship; I cannot wait to see what you all do. Members of SWG, thank you for advocating for women+ and for allowing me the opportunity to be a part of it. Lastly, thanks to Kaitlyn McCain for being an excellent roommate and friend.

Thank you to the friends outside of UCLA who allowed me to root myself in something not academic. Mareike, Guillaume, Lia, and Paulina, thank you for your jokes and friendship over these last seven years. Layla, Jenna, Klaus, Blake, and Grace thanks for listening and always being available when I suddenly find myself in Michigan.

Last but certainly not least, thank you to my family. Mom and Dad, thank you for, while not understanding my choice to move to California, none-the-less supporting that decision and always providing encouragement during the last six years. Brian, thank you for answering my frantic calls when my computer decides to do something weird. Grandma Kirkpatrick, thank you for your kindness throughout my life. Grandma Schultz, thank you for always being strong. Final thanks to those who let me pet their dogs.

For Chapter 2, we thank H. Beeson, S. Gallen, E. Kirby, T. Schildgen, P. Upton, P. van der Beek, and an anonymous reviewer for constructive reviews, E. Alexander, A. Simon, D. Yin, J.-L. Chen, and W. Chen for field assistance, V. Godard for sharing data, G. Li, M. Lamb, and G. Hilley for discussion, W. Kang for graphic assistance, and A. Simon for assistance with the fault compilation. S.M acknowledges the support of NSF EAR-1945431 and EAR-1728145. We thank PRIME lab for providing a seed grant and sample analysis.

For Chapter 3, we thank Ed Young for help with the ionic model and Ming-Chang Liu and Andreas Hertwig for assistance with the ion probe. This work was supported by a UCLA Dissertation Year Fellowship and a Geological Society of America student research grant to H.M.K., NSF-EAR 2131632 and 2131643 grants to M.I.-M., and by NSF grants EAR-1824002 and MGG-2054892, a Packard Fellowship and Caltech start-up funds to F.L.H.T. The ion microprobe laboratory at UCLA is partially funded by grant EAR-1734856 from NSF's Instrumentation and Facilities program.

For Chapter 4, I think Dustin Trail for performing the piston cylinder experiments, Jay Thomas for providing experimental mounts, Craig Manning for discussion, and Ming-Chang Liu and Elizabeth Bell for instrument set-up.

Curriculum Vita

Heather M. Kirkpatrick

Education

University of California, Los Angeles — Fall 2016 – Spring 2022
PhD Candidate, Geology
Candidacy Exam, September 2020 (C.Phil. awarded)
Qualifying Exam, June 2018 (M.S. awarded)

University of Michigan — Fall 2011-Winter 2015
B.S. in Earth and Environmental Sciences and the Environment (Program in the Environment)

Awards and Grants

UCLA Dissertation Year Fellowship — 2021-2022
Geologic Society of America Student Research Grant — 2021
3rd place for talk at 12th UCLA Annual Earth and Planetary Science Student Research Symposium, 2021
Certificate of Appreciation from the UCLA Division of Physical Sciences for community engagement activities — 2020
UCLA EPSS Harold and Mayla Sullwold Scholarship — 2020
Geologic Society of America Student Research Grant — 2020
UCLA EPSS Outreach Award — 2018
UCLA EPSS Department Scholarship — 2016
Robert Owen Fund Scholarship — 2014
University of Michigan Shell Corporation Scholarship — 2014
University of Michigan University honors — Fall 2013, Winter 2014, Fall 2014, Winter 2015

Publications

Borlina, C.S., Weiss, B.P., Lima, E.A., Tang, F., Taylor, R.J.M., Einsle, J.F., Harrison, R.J., Fu, R.R., Bell, E.A**.,** Alexander, E.W.**, Kirkpatrick, H.M.**, Wielicki, M.M., Harrison, T.M., Ramezani, J., and Maloof, A.C., 2020, Reevaluating the evidence for a Hadean-Eoarchean dynamo: Science Advances, v. 6, no. 15, pp. 1-9, doi:10.1126/sciadv.aav9634.

Kirkpatrick, H.M., Moon, S., Yin, A., and Harrison, T.M., 2020, Impact of fault damage on eastern Tibet topography: Geology, v. 49, no. 1, pp. 30-34, doi:10.1130/G48179.1.

Bell E. A. and **Kirkpatrick H. M.,** 2021, Effects of crustal assimilation and magma mixing on zircon trace element relationships across the Peninsular Ranges Batholith. Chem. Geol. 586, 120616.

Carley, T.L., Bell, E.A., Miller, C.F., Claiborne, Hunt, A., **Kirkpatrick, H.M.**, and T.M. Harrison, Zircon-modeled melts clarify the formation of Earth's crust from the Hadean to the Archean, 2022, Geology, In press.

Bell, E.A. **Kirkpatrick, H. M.**, and Harrison, T.M., Crystallization order effects on inclusion assemblages in magmatic accessory minerals and implications for the detrital record,

Submitted to Chemical Geology.

Kirkpatrick, H.M., Harrison, T.M., Bell, E.A., Liu, M.-C., Tissot, F.L.H., MacLennan, S.A., and Ibanez-Mejia, M., Petrologic Controls on Zr isotope fractionation, *Submitted to Geochimica Cosmochimica Acta*.

Bell, E.A. and **Kirkpatrick, H.M.** Accessory mineral micro-zircon inclusions yield more complete magma compositional evolution records, *Submitted to Contributions in Mineralogy and Petrology*.

Selected Conference Abstracts

Bell, E.A. and **H. Kirkpatrick** (2021), Petrologic and geochemical records of late magmatic processes in a shallow highly silicic granite, Abstract V35B-0138 presented at 2021 Fall Meeting, AGU, New Orleans, LA, 13-17 Dec.

Kirkpatrick, H., T.M. Harrison, E.A. Bell, M.-C.- Liu, F. Tissot, S.A. MacLennan, and M. Ibanez-Mejia (2020), Are Zr stable isotopes tracking magmatic differentiation in the zoned La Posta pluton?, Abstract V032-0004 presented at 2020 Fall Meeting, AGU, San Francisco, CA

Moon, S., **H. Kirkpatrick**, G. Li, A. Yin, and T.M. Harrison (2020), Influence of tectonic damage on erosion and topography of eastern Tibet, Abstract EP032-05 presented at 2020 Fall Meeting, AGU, San Francisco, CA

Kirkpatrick H., Harrison T.M., Liu M.-C., Tissot F. and Ibanez-Mejia M (2019), *In situ* $d^{94/90}Zr$ Variations in Zircon, Goldschmidt Abstracts, 2019 1696, Barcelona, Spain

Teaching Experience

University of California, Los Angeles — Fall 2016-Summer 2021

- Introduction to Geology (Primary instructor) (EPS SCI 1): Summer 2021
- Igneous Petrology (EPS SCI 103A): Winter 2021
- Mineralogy: Earth and Planetary Materials (EPS SCI 51): Fall 2021
- Introduction to Geology (EPS SCI 1): Fall 2016, 2017, 2018, 2019 and Winter 2019, 2020
- Tectonic Geomorphology (EPS 165): Spring 2017

Chapter 1: Introduction

1.1 Background

Throughout human history, our species have surely looked at the stars and our world in an effort to understand why we are here and where we came from; we weave our surroundings into stories – models – to explain our existence in the cosmos. Early quasi-scientific observations gave us existential answers regarding Earth's relationship to other planetary bodies but also lessons in enhancing crop yields and other techniques to advance civilization (Erickson, 2003; Kendall, 2013). Hundreds of years after the dawn of the Enlightenment, we are still seeking to understand those and other questions. While geology is a relatively old scientific discipline, it is not the most mature. In fact, its greatest revelation – plate tectonics – akin to the theory of evolution in biology was only adopted within the last 60 years (McKenzie and Parker, 1967). Since this discovery, geology has grown more interconnected with the enabling sciences (i.e., physics, chemistry, and biology; NSF Decadal Report, 2020). These quantitative ties to the observations humans have been making for thousands of years has allowed unparalleled insights into both our planet and, increasingly, to other planetary bodies in and beyond our solar system.

For fifty years following their discovery just over a century ago (Thomson, 1912), isotopes contributed little to our understanding of Earth history. Then, beginning in the 1960s, tools including precise isotope ratio mass spectrometry (Nier, 1960), isochron dating (Nicolaysen, 1961), and cosmogenic nuclide analysis (Lal and Peters, 1962) revolutionized our understanding of marine paleo-thermometry (Clayton and Epstein, 1961), continental evolution (Tilton and Hart, 1963) and global tectonics (McDougall and Tarling, 1964). Today, isotope geochemistry is at the heart of virtually all advances in understanding timescales of magmatic processes (e.g., Rivera et

al., 2014) and landscape evolution (e.g., Herman et al., 2010), the tempo of biologic change (e.g., Whiteside et al., 2007; Schoene et al., 2014), and the timing of abrupt climate change (Wang et al., 2001). Geochemical tools developed over the last several decades have not only led to a greater understanding of the world around us, but also facilitated a glimpse into Earth's deepest past (e.g., Harrison 2020). Specifically, in situ methods, including secondary ion mass spectrometry (SIMS) and laser ablation inductively coupled plasma mass spectrometry (LA-ICPMS), allow faster data collection and improved spatial resolution compared to other methods like thermal ionization mass spectrometry (TIMS). Notably, Hadean and Archean zircons ($ZrSiO_4$) have been extensively examined via SIMS and LA-ICPMS (Holden et al., 2009; Pullen et al., 2014) revealing surprising observations, including the existence of surface water (Mojzsis et al., 2001), potentially biogenic carbon in Hadean zircons (Bell et al., 2015), and possible evidence of plate boundary interactions (Hopkins et al., 2008, 2010) on early Earth. These ideas contrast with the long-held belief that Hadean Earth's surface was a molten hellscape (see Harrison, 2020) as represented by its name.

These discoveries would not be possible without the development of zircon as a geochronometer and geochemical proxy for environmental conditions of formation. Due to the beneficial characteristics of zircon, a common accessory mineral in felsic rocks, including it being conducive to U-Pb dating (Hanchar and Hoskin, 2003) and its resistance to abrasion and resorption, it is common in sedimentary and metasedimentary rocks (Fedo et al., 2003). Indeed, no other mineral has been used as effectively as zircon to understand Earth's deep history (Harrison, 2020). Because of these many benefits, it has proven to be the mineral of choice to develop as a record of past formation environments and the chemistry of the magmatic and metamorphic hosts from which it crystallizes. Zircon comprises the only known lithic record of the Hadean (>4 Ga; Harrison, 2020) Eon making it the sine qua non of early Earth investigations.

While studies of the earliest terrestrial lithic record can shed light on this poorly understood phase of Earth history, in some ways they represent the least challenging of geochronologic investigations. That's because the signal to noise ratio in a radiogenic decay system increases exponentially with time. Furthermore, those studies are carried out in the absence of known field relations which could otherwise provide further constraints on interpretive models. In contrast, radionuclide studies of Quaternary processes are far more technically demanding than ancient systems due to their relative youth and are almost invariably associated with a geologic context that can place important limits on physical models of their evolution. This is reflected in the questions we ask for each time period. For example, in Quaternary investigations we question why mountain ranges have specific topographic forms. As we go back further in time, we have progressively fewer geologic constraints and therefore ask different types of questions such as: was there water on Hadean Earth? In Quaternary studies, we typically have the benefit of high-resolution digital elevation models, a largely intact rock record, lithologic maps, and modern vegetation and precipitation datasets that lend themselves to limited back extrapolation. These rich collections allow us to measure and test different ideas about the catalyst for different geologic phenomena.

Laboratory experiments have different but coequally beneficial qualities. We can, for example, examine thermodynamic controls on trace element partitioning among different minerals that could provide constraints on past geologic processes that might otherwise remain occult. As we go further back in time, we lose resolution and even access to knowledge about past surface processes. This loss, however, can be compensated by knowledge of deeper crustal processes. For example, extending along much of southwestern North America, igneous rocks recording nearly 100 Ma of magmatism are exposed to us allowing us to examine controls on geochemical

variations within a single batholith. Our Hadean samples to date do not come with an intact rock context making investigations such as these impossible. However, the tools developed to geochemically and geochronologically characterize the exposed rock record, can be refined to examine the tiny remnants we possess of earliest Earth. While the conclusions we draw from analysis of our most ancient samples cannot be as certain or detailed as those from younger materials because of their lack of an intact rock context, we can test ideas about this formative period and perhaps move the boundaries of human understanding.

This thesis describes isotopic investigations of geologic phenomena that range in age by many orders of magnitude – from the Pleistocene epoch to the Cretaceous. A consistent theme among these studies is their use of the properties of trace element geochemistry and quantitative physical models.

1.2 Trace element chemistry

The emergence of isotope geochemistry over the past 60 years, as noted in the previous section, has drawn attention to the inverse relationship between chemical concentration and interpretive power: it is often the species of low abundance that contain the most powerful historical and environmental records. Each of the studies that comprise this thesis revolves around trace elements. Chapter 2, which examines the impact of tectonic damage on mountainous landscapes in eastern Tibet, relies on measurements of cosmogenic nuclides in quartz. Specifically, the concentration of ^{10}Be, which forms from spallation of oxygen nuclei by cosmic rays in quartz, is used to determine recent, basin-averaged erosion rates (von Blanckenberg, 2005; Brown et al., 1981). In general, sedimentary basins with a lower concentration of ^{10}Be in quartz are from faster eroding basins whereas higher concentrations of ^{10}Be in quartz are seen to derive from slower

eroding terrains. These erosion rates are then used to understand the controls that tectonics, climate, and lithology have on the evolution of river channels and basins.

Chapter 3, which seeks to understand controls on Zr stable isotope chemistry in zircon, also relies on trace elements in three ways. First, resolving the mineralogical controls on the isotopic evolution of a magmatic complex is important if we wish to leverage knowledge of that system to understand out-of-context igneous rocks or minerals (e.g., detrital zircons). To understand the specific controls on the Zr-isotope evolution of a zircon, we perform in situ trace element analyses at the individual grain level. Interpretation of these trace element patterns permits insight into co-crystallizing phases. Secondly, we can measure the Zr isotopic composition and concentration of other phases where Zr is only a minor constituent of the mineral. Both the relatively high concentration of Zr in certain phases (up to several hundred ppm in titanite) and their isotopic composition can impact the Zr isotopic budget of a system. Third, we use the trace U and Pb in zircons to obtain crystallization ages. Together, these different aspects of trace elements allow us to piece together the history and controls on Zr isotope evolution.

Chapter 4, initially an effort at intercalibrating multiple thermobarometers, relies on substitution of trace elements into different mineral structures. The concentrations of these different trace elements are then used to understand the temperature and pressure of formation conditions for each phase that in turn can be used to infer past magmatic environments.

1.3 Models

A second connecting link between these chapters is the use of interpretive physical models. While each of the studies is driven primarily by analytical results, whether obtained in the field or laboratory, each involves testing a model proposed to integrate a suite of observations. Perhaps

the simplest models are geochronological frameworks, although these models range in complexity from that described in Chapter 2, in which calculation of a cosmogenic nuclide exposure age requires assumptions or estimates of the spallation reactions in quartz and topographic shielding (Lal, 1991; Bierman and Steig, 1996; Granger et al., 1996; Balco et al., 2008; Dunai, 2010) in order to calculate an erosion rate, to the more straightforward paired decay in the U-Pb decay system which utilizes a variant of the classic age equation (Rutherford and Soddy, 1902).

In Chapter 2, we also use models to calculate topographic metrics, including channel steepness, hillslope, and relief and perform statistical analyses. In this chapter and it associated appendix we discuss various methods used to determine erosional coefficients, keeping in mind that each calculation relies on model assumptions. Indeed, each topographic calculation relies on our digital elevation model, itself computed from incomplete data.

To understand controls on Zr stable isotope fractionation in zircon in Chapter 3, we utilize fractionation models derived from ab initio calculations, a model assumption of the geometry of ionic solids, and an empirical regression model put forward in a published study. Each method of calculating the fractionation factor makes different assumptions and approximations.

Chapter 4 investigates a trace element thermobarometer calibrated experimentally at pressure, temperature, and composition in the laboratory: specifically, the co-crystallization of quartz and rutile lends to the Ti-in-quartz thermobarometer. A model relating pressure, temperature, and Ti composition of run products is developed and can be used to constrain magmatic and metamorphic conditions throughout Earth history. Recent investigations (Acosta et al., 2020) have questioned the validity of earlier proposed models and in this chapter, we discuss underlying model assumptions in context of our new results.

In summary, virtually all results presented in this thesis are either derived through a model framework or used to infer geologic context through a physical model. But what is a model in this context? It is a physical or mathematical representation of an actual geophysical phenomenon that can explain or predict the behavior of a set of observations. Thus, they are only ever approximations of the systems that they are designed to represent. As Box and Draper (1987) famously wrote: "All models are wrong; the practical question is how wrong do they have to be to not be useful". My view is that each study must be interpreted and validated through the lens of geologic history. For example, while a spot analysis of Ti in quartz from a granite might imply a temperature of several thousand °C, we can be certain that this model calculation is incorrect and likely due to the presence of a Ti-rich inclusion. In Chapter 3, I conclude that an empirical model proposed to describe the temperature dependence of Zr isotopic fractionation (Guo et al., 2020) is aphysical. In short, throughout the investigations that comprise this thesis we must continuously ask ourselves whether our model results are geologically plausible and continuously refine them until high fidelity with natural observation is realized.

1.4 References:

Acosta, M. D., Watkins, J. M., Reed, M. H., Donovan, J. J., and DePaolo, D. J., 2020, Ti-in-quartz: Evaluating the role of kinetics in high temperature crystal growth experiments. Geochimica et Cosmochimica Acta, 281, 149–167. https://doi.org/10.1016/j.gca.2020.04.030

Balco, G., Stone, J.O., Lifton, N.A., and Dunai, T.J., 2008, A complete and easily accessible means of calculating surface exposure ages or erosion rates from 10Be and 26Al measurements: Quaternary Geochronology, v. 3, p. 174–195, doi:10.1016/j.quageo.2007.12.001.

Bell, E.A., Boehnke, P., Harrison, T.M., and Mao, W.L., 2015, Potentially biogenic carbon preserved in a 4.1 billion-year-old zircon: Proceedings of the National Academy of Sciences of the United States of America, v. 112, p. 1–4, doi:10.1073/pnas.1517557112.

Bierman, P. and Steig, E.J., 1996, Estimating rates of denudation using cosmogenic abundances in sediment: Earth Surface Processes and Landforms, v. 21, p. 125–139.

Box, G. E. and Draper, N. R., 1987, Empirical model-building and response surfaces. Wiley.

Brown, L., Klein, J., Middleton, R., Sacks, I.S., and Tera, F., 1981. 10Be as a geochemical and geophysical probe. Carnegie Instit. Wash. Year Book 80, 443-448.

Clayton, R.N. and Epstein, S., 1961, The use of oxygen isotopes in high-temperature geological thermometry. Journal of Geology 69, 447-452.

Dunai, P.T., 2010, Cosmic ray-produced radionuclides in Earth Sciences Primary Nature: High-energy charged particles: Cambridge, Cambridge University Press, 14 p.

Erickson, C. L., 2003, Agricultural landscapes as world heritage: raised field agriculture in Bolivia and Peru. *Managing change: sustainable approaches to the conservation of the built environment. The Getty Conservation Institute, Los Angeles, California, USA*, 181-204.

Fedo, C.M., Sircombe, K.N., and Rainbird, R.H., 2003, Detrital Zircon Analysis of the Sedimentary Record: Reviews in Mineralogy and Geochemistry, v. 53, p. 277–303, doi:https://doi.org/10.2113/0530277.

Granger, D.E., Kirchner, J.W., Finkel, R., 1996, Spatially Averaged Long-Term Erosion Rates Measured from in Situ-Produced Cosmogenic Nuclides in Alluvial Sediment, The Journal of Geology v. 104, p. 249-257.

Guo J.-L., Wang Z., Zhang W., Moynier F., Cui D., Hu Z. and Ducea M. N., 2020, Significant Zr isotope variations in single zircon grains recording magma evolution history. Proceedings of the National Academy of Sciences. 117, 21125–21131. Available at: https://www.pnas.org/content/117/35/21125.

Hanchar, J.M., and Hoskin, P.W.O. (Eds.), 2003, ZIRCON: Reviews in Mineralogy and Geochemistry, 1–500 p.

Harrison, T.M., 2020, Hadean earth: 1–291 p., doi:10.1007/978-3-030-46687-9.

Herman, F., Copeland, P., Avouac, J.P., Bollinger, L., Mahéo, G., Le Fort, P., Rai, S., Foster, D., Pêcher, A., Stüwe, K. and Henry, P., 2010, Exhumation, crustal deformation, and thermal structure of the Nepal Himalaya derived from the inversion of thermochronological and thermobarometric data and modeling of the topography. Journal of Geophysical Research: Solid Earth, 115(B6).

Holden, P., Lanc, P., Ireland, T.R., Harrison, T.M., Foster, J.J., and Bruce, Z., 2009, Mass-spectrometric mining of Hadean zircons by automated SHRIMP multi-collector and single-collector U/Pb zircon age dating: The first 100,000 grains: International Journal of Mass Spectrometry, v. 286, p. 53–63, doi:10.1016/j.ijms.2009.06.007.

Hopkins, M.D., Harrison, T.M., and Manning, C.E., 2008, Low heat flow inferred from >4 Gyr zircons suggests Hadean plate boundary interactions: Nature, v. 456, p. 493–496, doi:10.1038/nature07465.

Hopkins, M.D., Harrison, T.M., and Manning, C.E., 2010, Constraints on Hadean geodynamics from mineral inclusions in >4Ga zircons: Earth and Planetary Science Letters, v. 298, p. 367–376, doi:10.1016/j.epsl.2010.08.010.

Kendall, A., 2013, Applied Archaeology in the Andes: The Contribution of Pre-Hispanic Agricultural Terracing to Environmental and Rural Development Strategies. In: Humans and the Environment: New Archaeological Perspectives for the Twenty-First Century. First Edition. Edited by Matthew I. J. Davies and Freda Nkirote M'Mbogori, Oxford University Press.

Lal, D. and Peters, B., 1962. Cosmic ray produced isotopes and their application to problems in geophysics. Progr. Elem. Particle Cosmic Ray Phys., 6.

Lal, D., 1991, Cosmic ray labeling of erosion surfaces: in situ nuclide production rates and erosion models: Earth and Planetary Science Letters, v. 104, p. 424–439.

McDougall, I. and Tarling, D.H., 1963, Dating of polarity zones in the Hawaiian islands. Nature 200, 54-56.

McKenzie, D., Parker, R., 1967, The North Pacific: an Example of Tectonics on a Sphere. Nature 216, 1276–1280. https://doi.org/10.1038/2161276a0

Mojzsis, S.J., Harrison, T.M., and Pidgeon, R.T., 2001, Oxygen-isotope evidence from ancient zircons for liquid water at the Earth's surface 4,300 Myr ago: Nature, v. 409, p. 178–181.

National Academies of Sciences, Engineering, and Medicine, 2020, A Vision for NSF Earth Sciences 2020-2030: Earth in Time. Washington, DC: The National Academies Press. https://doi.org/10.17226/25761.

Nicolaysen, L.O., 1961, Graphic interpretation of discordant age measurements on metamorphic rocks. Annals of the New York Academy of Sciences 91198-20, 6.

Nier, A.O., 1960, Small general purpose double focusing mass spectrometer. Review of Scientific Instruments 31, 1127-1132.

Pullen, A., Ibañez-Mejia, M., Gehrels, G.E., Ibañez-Mejía, J.C., and Pecha, M., 2014, What happens when n= 1000? Creating large-n geochronological datasets with LA-ICP-MS for geologic investigations: Journal of Analytical Atomic Spectrometry, v. 29, p. 971–980, doi:10.1039/c4ja00024b.

Rivera, T.A., Schmitz, M.D., Crowley, J.L., and Storey, M., 2014, Rapid magma evolution constrained by zircon petrochronology and 40Ar/39Ar sanidine ages for the Huckleberry Ridge Tuff, Yellowstone, USA. Geology, 42, 643–646.

Rutherford, E. and Soddy, F., 1902, The cause and nature of radioactivity. Part I. The London, Edinburgh, and Dublin Philosophical Magazine and Journal of Science 4, 370-396.

Schoene, B., 2014, U-Th-Pb Geochronology. In Treatise on Geochemistry, 341–378.

Thomson, J.J., 1912, Further experiments on positive rays. Philosophical Magazine, 24. 209–253.

Tilton, G.R. and Hart, S.R., 1963, Geochronology: New techniques provide knowledge of the time and mode of formation and subsequent evolution of rock systems. Science 140357-3 66.

von Blanckenburg, F., 2005, The control mechanisms of erosion and weathering at basin scale from cosmogenic nuclides in river sediment: Earth and Planetary Science Letters, v. 237, no. 3-4, 462-479.

Wang, Y.G., Cheng, H., Edwards, R.L., An, Z.S., Wu, J.Y., Shen, C.-C., and Dorale, J.A., 2001, A high resolution absolutedated late Pleistocene monsoon record from Hulu Cave, China. Science 294, 2345-2348.

Whiteside, J.H., Olsen, P.H., Kent, D.V., Fowell, S.J. and Et-Touhami, M., 2007, Synchrony between the Central Atlantic magmatic province and the Triassic–Jurassic mass-extinction event? Paleogeography, Palaeoclimatology, Palaeoecology. 244, 345-367.

Chapter 2: Impact of fault damage on eastern Tibet topography

Note: This chapter is modified from Kirkpatrick, H.M., Moon, S., Yin, A., and Harrison, T.M., 2020, Impact of fault damage on eastern Tibet topography: Geology, v. 49, no. 1, pp. 30-34, doi:10.1130/G48179.1.

2.1 Introduction

Relationships between topography and millennial erosion rates derived from cosmogenic ^{10}Be isotopes are typically interpreted to be controlled by tectonics or climate (von Blanckenburg, 2005; Portenga and Bierman, 2011). The topography of the eastern margin of the Tibetan plateau, which exhibits a >4000 m elevation change over a lateral distance of <100 km (Figure 2.1), has also been attributed to interactions between tectonic uplift, climate, and surface processes (Burchfiel et al., 1995; Ouimet et al., 2009; Kirby and Ouimet, 2011; Scherler et al., 2017). The important role of lithologic compositions and bedrock weathering on erosion and landscape evolution in eastern Tibet was emphasized by Godard et al. (2010) and Gallen et al. (2015). However, impacts of tectonic deformation through seismic shaking and bedrock damage (Faulkner et al., 2010; Huang et al., 2014; Ben-Zion and Zalipin, 2019), which can potentially lead to enhanced erosion (Molnar et al., 2007; Koons et al., 2012; Gallen et al., 2015; Roy et al., 2015, 2016; Duvall et al., 2020), has not been quantified in this tectonically active region. Here, we address this issue by showing how erosion coefficients, which quantify the relationship between topography and millennial-averaged erosion rates, vary as a function of distance to faults in eastern Tibet. To do so, we used cosmogenic ^{10}Be-derived erosion rates compiled from the literature and our own new measurements. We find a systematic increase in erosion coefficients within 15 km of major faults with this signal stronger than that induced by lithologic variation alone.

2.1.1 Geologic Background

In the northeastern part of the Tibetan Plateau near the Longmen Shan region, Triassic and Paleozoic siliciclastic and carbonate strata dominate (Kirby and Ouimet, 2011; Hartmann and Moosdorf, 2012; Tian et al., 2018). Precambrian basement rock and Mesozoic plutons are exposed in the hanging walls of thrust faults as gneiss domes or metamorphic massifs in the frontal Longmen Shan region (Tian et al., 2018). The dominant rock types in the Min Shan range to the north are Triassic and Paleozoic sedimentary rocks (Kirby and Ouimet, 2011). In addition, small areas (a few km^2) of volcanic rocks, plutonic rocks, and unconsolidated surficial deposits are scattered across eastern Tibet (Hartmann and Moosdorf, 2012). Compared to the dominance of sedimentary rocks to the north, the southwestern part of our study area has a higher proportion of metamorphic and plutonic rocks including the Gongga and Luding granites (Hartmann and Moosdorf, 2012; Zhang et al., 2017).

2.2 Methods

2.2.1 Determination of Erosion Rates

In situ production of cosmogenic radionuclides, such as ^{10}Be and ^{26}Al, mostly occurs within 1-2 m of Earth's surface and decreases exponentially with depth (Lal, 1991; Bierman and Steig, 1996; Granger et al., 1996; Balco et al., 2008; Dunai, 2010). We first compiled erosion rates using ^{10}Be isotopes from previous studies (Ouimet et al., 2009; Godard et al., 2010; Ansberque et al., 2015). Following the approaches of previous studies (Ouimet et al., 2009, Kirby and Ouimet, 2011, Scherler et al., 2017), we excluded 11 basins which are glaciated (wbo549, wbo550, and wbo633) and affected by landslide derived sediments (wbo523, wbo637, and wbo639). This is because

basins affected by landslides and glaciers likely have biased ^{10}Be-derived erosion rates due to a significant input of sediment with low ^{10}Be concentrations (Hallet and Hunter, 1996; Niemi et al., 2005). In addition, we excluded basins with areas larger than 6000 km^2 due to potentially inconsistent sediment delivery over time (LM254, LM261, LM263, SC049, and SC086). Previous studies have also removed samples with large basin areas (Kirby and Ouimet, 2011; Scherler et al., 2017). We used averaged erosion rates for duplicate samples from 3 basins (LM253 and SC082; wbo610s and wbo610q; wbo624s and wbo624q). We only used basin-averaged erosion rates of the original sampled basins and did not recalculate erosion rates for partial areas of nested basins. This resulted in a total of 100 erosion rate measurements compiled from previous studies (Table S1) (Ouimet et al., 2009; Godard et al., 2010; Ansberque et al., 2015).

We measured millennial erosion rates using ^{10}Be isotopes for 11 basins from the Min Shan. We collected sand samples from nine basins in the Fu Jiang catchment (ET01-ET06, ET08-ET10), one basin from the Min Jiang catchment (ET12), and one basin draining the Bailong He catchment (ET11) in September 2016 (Fig. 2.4). Our collected samples were sieved at UCLA, and the 250-500 μm size fraction was used for measurements. Quartz was purified by a series of chemical leaching steps using concentrated HNO_3 and an ~1% HNO_3 and ~1% HF mixture with DI water, and samples were separated using a magnetic separator and LST at PRIME Lab, Purdue University. A total of 1.5 – 23.3 g quartz was dissolved after adding 0.235-0.261 mg of ^{9}Be carrier. Be fractions were extracted using ion-exchange chromatography. The ^{10}Be/^{9}Be ratios were measured by Accelerator Mass Spectrometry at PRIME Lab, Purdue University based on the calibration of Nishiizumi et al. (2007) (Table S2). Two full process blanks for ^{10}Be/^{9}Be were measured as (1.1-1.5) × 10^{-15}, and the averaged ^{10}Be atoms per mg of ^{9}Be carrier was 85,408. The total ^{10}Be atoms in the blanks include ^{10}Be from the carrier and additions from chemical and

measurement processes. ^{10}Be atoms from the carrier were subtracted from measured total concentrations to calculate carrier-corrected ^{10}Be atoms per g of quartz.

Topographic metrics required for erosion calculations including topographic shielding, mean latitude, mean longitude, and mean elevation were calculated via TopoToolbox in Matlab (Schwanghart and Scherler, 2014). These values along with measured concentrations of ^{10}Be and an assumed rock density of 2.7 g cm^{-3} were then used to compute erosion rates assuming the Lal (1991)-Stone (2000) time-dependent production model from the CRONUS online calculator version 3 (Lifton et al., 2014; Balco et al., 2008) (Table S1 and S2). The recalculation of erosion rates was needed to standardize data for the same ^{10}Be half-life (Nishiizumi et al., 2007), production rate scaling schemes (Balco et al., 2008), rock density, and topographic shielding. On average, the newly calculated erosion rates are ~0.08 mm yr^{-1} (0.07 mm yr^{-1}, 1 s.d.) less than the previously published values but show a strong linear correlation (R^2 = 0.99) with previous measurements.

In total, we recalculated previously published ^{10}Be-derived erosion rates (E) from 100 basins across eastern Tibet (Ouimet et al., 2009; Godard et al., 2010; Ansberque et al., 2015) and measured E from an additional 11 basins in the Min Shan area of eastern Tibet. These additional samples are from a tectonically active region underlain mostly by sedimentary rocks (Figures 1 and DR1, Tables DR1-2).

2.2.2 Quantification of topographic, geologic, climatic, and ecologic parameters

We calculated topographic metrics, including slope, local relief, and channel steepness, for each basin using ArcGIS and TopoToolbox in Matlab (Schwanghart and Scherler, 2014) (Table S3). We primarily used the 90 m void filled SRTM DEM (https://earthexplorer.usgs.gov/). For portions

of basins where the 90 m void filled STRM DEM did not have data, we used the DEM provided by de Ferranti (2018) (~6% of studied basins).

We compared *K* with geologic, climatic, and ecologic factors. We first compiled and quantified the distance to regional-scale (>50 km in length) fault systems (hereafter, major faults) systematically documented by previous studies (e.g., Burchfiel and Chen, 2013). The compiled faults include both inactive and active (i.e., since the Quaternary) structures because damage zones of inactive faults could also play a role in shaping present-day topography (Figure 2.1A, see Data Repository). Most of the major faults mapped in this study area are active (86% in total length).

We also calculated basin-averaged mean annual precipitation rates (*MAP*) (Bookhagen et al., 2010), normalized-difference-vegetation index (*NDVI*) (Didan et al., 2015), and peak ground acceleration (*PGA*) from the 2008 M_w 7.9 Wenchuan earthquake (Data Repository, Figures DR2-3, Table DR3). Basin-averaged values were obtained by averaging all pixel values within studied drainage basins.

2.2.3 Calculating controls on erosional coefficients

2.2.3.1 Calculating the erosional coefficient

We quantified erosion coefficients based on the relationship between *E* and normalized channel steepness (k_{sn}). We assume that (1) river incision into bedrock controls erosion and (2) detachment-limited bedrock erosion is a function of shear stress or stream power (Howard and Kerby, 1983; Howard et al., 1994; Whipple and Tucker, 1999). Then, we relate erosion rate as a function of measurable topographic attributes by:

$$E = KA^mS^n \quad (2.1)$$

where E [L t^{-1}] is erosion rate, K [L^{1-2m} t^{-1}] is erosion coefficient (a function of climate, channel geometry, and rock erodibility), A is drainage area [L^2], S is channel slope [unitless], and m and n are constants. In natural landscapes, local channel slope S can be expressed as,

$$S = k_s A^{-\theta} \quad (2.2)$$

where k_s is channel steepness ([$L^{2\theta}$]) and θ is concavity (Flint, 1974; Howard and Kerby, 1983). We extracted channel points with drainage areas larger than 1 km^2 and calculated normalized channel steepness (k_{sn}) assuming a reference concavity of 0.45, which is consistent with previous studies of this area (Ouimet et al., 2009; Kirby and Ouimet, 2011; Scherler et al., 2017).

By combining eq. 2.1 and 2.2, erosion coefficient K can be quantified as:

$$K = \frac{E}{k_{sn}^n} \quad (2.3)$$

The above relationship holds whether E is in steady state with uplift rate or not. We assume that sediment production and mixing and grain size distributions are not significantly affected by local effects. We calculated K assuming a linear relationship between k_{sn} and E (n = 1) following Kirby and Ouimet (2011) and Scherler et al. (2017). We calculated slope as the steepest descent gradient in an 8-cell neighborhood and local relief as the elevation difference between highest and lowest elevations within a 1-km radius circular moving window (see Data Repository; Table DR3). For sensitivity tests, we also calculated erosion coefficients based on different assumptions of river incision models (e.g., a non-linear relationship between k_{sn} and E, incorporation of discharge, and different power-law exponents based on stream power or shear stress incision models) or rate constants calculated from slope and local relief (see Data Repository; Table DR4).

2.2.3.2 Calculating lithologic distributions and understanding rock strength

We quantified percent areas of lithologies for each basin based on a lithologic map by Hartmann and Moosdorf (2012). We defined 7 rock classifications (metamorphic rocks, plutonic rocks, carbonate rocks, mixed composition sedimentary rocks that include both siliciclastic and carbonate sedimentary rocks (hereafter, mixed composition sedimentary rocks), siliciclastic sedimentary rocks, unconsolidated sedimentary rocks, and volcanic and pyroclastic rocks). We quantified areal percentages of each lithologic group for our studied basins (Table S5). Most basins consist of multiple lithologic groups. The number of basins that are dominated by (>50% in area) or composed entirely of a single lithologic group are listed in Table S6. To provide statistical significance, we focus on small basins with areas (A) <200 km^2 dominated by three dominant single lithologic groups (i.e., plutonic rocks, mixed composition sedimentary rocks, and siliciclastic sedimentary rocks) that have more than 10 basins. We use an area of 200 km^2 as the largest basin size for our "small basin" group following Ouimet et al. (2009) who used small catchments from the eastern margin of the Tibetan Plateau. We quantified the areal percent of seven lithologic groups for each basin (Table DR5) and identified basins dominated by single (defined by >50% of area) lithologies (Table DR6).

To understand the relative strengths of different lithologies, we measured Schmidt hammer rebound values, hereafter *H*-values, which represent rock hardness or strength at eight sites in eastern Tibet (Figs. 2.13-2.14) (Aydin and Basu, 2005). We used the N-type Proceq Original Schmidt hammer. According to the manufacturer, *H*-values from 25 to 55 correspond to compressive strengths from 14 to 59 MPa on a cylinder with 6 in bore and 12 in stroke (www.proceq.com/). For each site, we made between 30 and 50 measurements with typical equal distance spacings of 0.3 – 1 m.

Of the eight measurement sites, two were located close to the Longmen Shan region (1 in the Pengguan metamorphic complex; 1 in Silurian folded strata). The other 6 measurements were from near the Huya fault in the Min Shan region, which includes two measurements taken in areas containing Permian limestone and four measurements taken in areas containing mixed composition sedimentary rocks including sandstone, phyllite, and interbedded limestone.

2.2.3.3 Calculating other potential controls on erosional coefficients

To examine various controlling factors on erosion coefficients, we quantified basin-averaged values of fault distance, mean annual precipitation (*MAP*), normalized difference vegetation index (*NDVI*), and peak ground acceleration from the 2008 Wenchuan earthquake (*PGA*) by averaging corresponding values from all pixels within drainage areas. To do this, we first quantified the distance to faults as the linear horizontal distance between each pixel to its closest point among the major faults (Fig. 2.1). We quantified the distance to major faults (D_{mf}) considering both active and inactive faults and the distance to major active faults considering only active faults. We quantified mean annual precipitation rates based on the Tropical Rainfall Measuring Mission (*TRMM*) precipitation measurements averaged from 1998 to 2008 (Bookhagen et al., 2010). In addition, we quantified basin-averaged *NDVI*, a measure of vegetation amount and health, as,

$$NDVI = \frac{(NIR-VIS)}{(NIR+VIS)} \qquad (2.4)$$

where NIR and VIS stand for the surface reflectance measurements of near-infrared and visible (red) bands, respectively. *NDVI* ranges from -1 to +1. Areas with low or negative *NDVI* indicate no or sparse vegetation while those with high *NDVI*, or values close to 1, indicate dense and healthy vegetation. We used a 250 m-resolution *NDVI* derived from a 16-day period (07/28/2019 to

08/12/2019 without clouds), which was downloaded from the Terra Moderate Resolution Imaging Spectroradiometer (MODIS) Vegetation Indices (MOD13Q1) Version 6 (Data accessed on 08/29/19; Didan et al., 2015).

2.2.4 Fault compilation and impacts from earthquakes

2.2.4.1 Active and inactive faults in eastern Tibet

To examine the impact of fault damage on erosion, we compiled faults and fault systems located in eastern Tibet. Because detailed, local-scale fault maps are not consistently available throughout our study area, we only consider regional-scale (>50 km in length) faults and fault systems (hereafter, major faults) systematically documented by previous studies (Burchfiel et al., 1998; Chen and Wilson, 1996; Kirby et al., 2002; Burchfiel and Chen, 2012; Yan et al., 2011; Yan et al., 2018). In addition, we consider both inactive and active faults because damage zones of both active and inactive faults could have an influence on shaping present-day topography. Most major faults mapped in this study area are active faults based on current literature (86% in total length). Only a few inactive structures are present in the frontal Longmen Shan, which include (1) the low-angle shear zones separating the basement rocks from the sedimentary sequence, and (2) narrow klippen structures duplicated by the Cenozoic thrusts and placing Late Paleozoic strata over Jurassic strata (Chen and Wilson, 1996; Kirby et al., 2002; Yan et al., 2011).

We use fault maps from Burchfiel et al. (1995), Chen and Wilson (1996), and Kirby et al. (2002) as base maps and extend our compilation to include faults from Pan et al. (2004), Wang et al. (2012), Ren et al. (2013a, b), Long et al. (2015), Ansberque et al. (2015), Zhang et al. (2015), Chavalier et al. (2016), Ren et al. (2018), Yan et al. (2011) and Yan et al. (2018). The faults and fault systems considered in this study include the Beichuan-Yingxiu fault (B.-Y.F.), the Guanxian-

Anxian fault (G.-A.F), the Huya fault (H.F.), the Jiulong fault system (J.F.S.), the nappes and klippen belts near the frontal Longmen Shan (n.k.), the Kunlun fault system (K.F.), the Litang fault system (L.F.), the Longriba fault system (L.F.S.), the Maerkang fault (Ma.F.), the Minjiang fault (Mi.F.), the Maowen fault (Mao.F.), the Muli fault (Mu.F.), the Qingchuan-Pingwu fault (Q.-P.F.), the Xianshuihe fault system (X.F.S.), and the Xueshan fault (XS.F).

Faults that have been active during the Quaternary (hereafter, active faults) and for which we have records of historic or recent seismic activity are discussed below. The Beichuan, Wenchuan, and Pengguan fault zones near the frontal Longmen Shan region have experienced several $M_w > 6.5$ earthquakes over the last 50 years, including the 2008 M_w 7.9 Wenchuan earthquake (Chen et al., 1994; Xu et al., 2017). To the north, the Min Shan region also has several active faults including the north-striking Min Jiang fault (1933 M_w 7.38 earthquake; International Seismology Centre), the east-striking Xueshan fault which was possibly reactivated from a Mesozoic structure (Kirby et al., 2000), the northwest-striking Huya fault, and the northeast-striking Qingchuan fault (Chen et al., 1994; Burchfiel et al., 1995; Taylor and Yin, 2009; Xu et al., 2017). Four $M_w \geq 6.5$ earthquakes have occurred along the Huya fault in the last ~50 years: three in 1976 (Chen et al., 1994) and one, the M_w 6.5 Jiuzhaigou earthquake, in 2017 (Xu et al., 2017; IRIS, www.iris.edu). North of the Longmen Shan, a M_w 6.1 earthquake occurred along the Maerkang fault on September 22, 1989 indicating that this fault is also active (IRIS, www.iris.edu). There is no record of historic earthquakes occurring along faults in the Longriba fault system (the Longriqu fault and the Maoergai fault), but Ren et al. (2013a, 2013b) determined from trenching, landform mapping, radiocarbon dating, and OSL dating that the Maoergai fault (southern) last ruptured about 5170 ± 80 years ago and the Longriqu fault (northern) last ruptured about 5080 ± 90 years ago. The Daxue Shan region in the southern part of our study area contains the Xianshuihe fault system consisting

of four segments: Ganzi, Xianshuihe, Anninghe, and Zemuhe-Xiajiang (Allen et al., 1991; e.g. Zhang et al., 2017) along which several $M_w < 6.5$ earthquakes occurred in the last 50 years (IRIS, www.iris.edu). The Litang fault, south of the Xianshuihe fault, has hosted several $M_w > 5$ earthquakes since 1976 (IRIS, www.iris.edu). The spatial distributions of active and inactive faults are shown in brown solid lines and blue dashed lines in Fig. 2.1, respectively.

2.2.4.2 Distance to major faults calculation

Distance to major faults (D_{mf}) is calculated as the linear horizontal distance between each 90-m-DEM pixel to the nearest fault. We performed statistical tests to evaluate controls on K (Table S4). First, we examined correlations between various controls and erosion coefficients based on different model assumptions and rate constants from topographic metrics (Data Repository; Table DR7). Then, we performed *t*-tests and *F*-tests to examine how K is different for subsets of basins divided by D_{mf}, lithologic groups, and basin area (Tables DR8-9). Since large basins may not represent basin-averaged erosion rates due to incomplete sediment mixing (Ouimet et al., 2009; Kirby and Ouimet et al., 2011), we performed analysis for five basin groups: (1) all basins, (2) basins with A <200 km^2 (hereafter, small basins), and small basins dominated by single lithologies of (3) plutonic, (4) mixed composition sedimentary rocks that include both siliciclastic and carbonate sedimentary rocks, and (5) siliciclastic sedimentary rocks. We focused on 3 single lithologies that have more than 10 sampled basins. We then used basins that were not significantly affected by the 2008 Wenchuan earthquake for further analysis. A *p*-value of less than 0.05 is used as the threshold for statistical significance for all tests (see Data Repository).

2.2.4.3 Determining the impact from earthquakes

Lastly, we quantified the basin-averaged peak ground acceleration (*PGA*) that was simulated for the 2008 M_w 7.9 Wenchuan earthquake that ruptured ~270 km of the frontal Longmen Shan fault system. A previous study by Li et al., (2017) showed that earthquake-induced landslides from large magnitude earthquakes similar to the 2008 Wenchuan earthquake contribute significantly to the long-term denudation rates inferred from cosmogenic nuclides and low temperature thermochronology. In this case, seismic shaking from large earthquakes can enhance erosion by generating coseismic landslides and influence erosion coefficients. To examine this, we quantified the basin-averaged *PGA* based on simulated *PGA* from USGS ShakeMap Atlas v4 (Data accessed on 06/08/20). Basin-averaged *PGA* varies from 0.02 g to 0.92 g. For reference, *PGA* values < 0.0017 g, 0.0017-0.014 g, 0.014-0.039 g, 0.039-0.092 g, 0.092-0.18 g, 0.18-0.34 g, 0.34-0.65 g, and 0.65-1.24 g correspond to a perceived shaking of not felt, weak, light, moderate, strong, very strong, severe, and violent, respectively.

In addition, West et al. (2014) showed that input from earthquake-induce landslides from the 2008 M_w 7.9 Wenchuan earthquake diluted ^{10}Be concentrations in quartz, especially in areas with high *PGA* and extensive coseismic landslides (> ~0.3 % of the upstream catchment area affected by landslides). However, in areas with low landslide occurrences, there were no systematic changes in ^{10}Be concentration in quartz. Significant inputs from earthquake-induced landslides can result in increased ^{10}Be-derived erosion rates which may not be representative of long-term millennial erosion rates. Most coseismic landslides from the 2008 Wenchuan earthquake occurred within ~30 km of the Beichuan-Yingxiu fault surface rupture and have a *PGA* greater than 0.2 g (Xu et al., 2014; Li et al., 2017). Thus, we performed sensitivity analyses using (1) basins sampled before the 2008 Wenchuan earthquake and (2) basins sampled before the 2008 Wenchuan earthquake or

sampled outside of the severe shaking range after the 2008 Wenchuan earthquake (i.e. *PGA* < 0.34 g). This follows a similar criterion to what is used in Ansberque et al. (2015).

2.3 Results

2.3.1 Erosion rates

Erosion rates from 11 basins measured in this study vary from 0.24 ± 0.06 mm yr^{-1} to 0.76 ± 0.08 mm yr^{-1}. The highest erosion rates in the Min Shan region, ET06 (0.62 ± 0.08 mm yr^{-1}), ET09 (0.76 ± 0.08 mm yr^{-1}), and ET10 (0.53 ± 0.08 mm yr^{-1}), correspond to basins near the Huya fault (Fig. 2.1A; Fig. 2.4). The lowest erosion rate (ET12, 0.24 ± 0.06 mm yr^{-1}) presented here corresponds to sediment collected from the headwaters of rivers that flow into the Longmen Shan. ET11 (0.31 ± 0.03 mm yr^{-1}), which is partially on the low relief portion of the plateau and has an erosion rate similar to those on the plateau, was collected in a tributary to a river north of the Fu Jiang (Bailong Jiang).

^{10}Be-derived erosion rates (*E*) range from 0.020 ± 0.002 to 0.76 ± 0.08 mm yr^{-1} (1σ) (Table DR2). The highest *E* is from near the Huya fault in the Min Shan region (ET09: *E* = 0.76 ± 0.08 mm yr^{-1}), and the lowest *E* is from the southern portion of our study area (wbo545: *E* = 0.020±0.002 mm yr^{-1}) (Ouimet et al., 2009) (Figure 2.1A). Basins in the hinterland or low relief portion of the plateau generally have lower *E* compared to those from the Longmen Shan and Min Shan range fronts.

2.3.2 Topographic metric and lithology results

The dominant lithology in studied basins are sedimentary rocks (Tables DR5 and DR6). Averaged D_{mf} range from 0.8 to 109.4 km. E shows positive correlations with slope, local relief, and channel steepness with a wide spread of data (Figure 2.2). Both linear and nonlinear models similarly explain relationships between E and topographic metrics (Table DR4).

Basin-averaged slopes range from 0.07 (± 0.05) to 0.89 (± 0.42), and basin-averaged local relief range from 130 (± 88) to 1268 (± 173) m. Basin-averaged channel steepness, k_{sn}, from the integral method range from 14 (1 s.e., ± 0.1) to 465 (1 s.e., ± 10) $m^{0.9}$ (Table S3; Fig. 2.2).

Both distance to major faults (D_{mf}) and active faults show statistically significant correlations with erosion coefficient K and various rate constants for all basins, small basins, and small basins dominated by siliciclastic sedimentary rock (Figures 3 and DR4, Table DR7). The control of D_{mf} on K is observed in wide ranges of E and k_{sn}, which indicates this result is not from a systematic bias from either E or k_{sn} (Figures 3 and DR5). Correlations between these various rate constants and *MAP*, *NDVI*, and *PGA* are statistically insignificant or weaker than those with D_{mf} (Figure DR6, Table DR7). We find that mean K from basins with $D_{mf} \leq 15$ km are ~2 times higher than those >15 km for all basins and small basins (Figure 2.3B). These results are consistent when using erosion coefficients from (1) different river incision model assumptions, (2) different rate constants from topographic metrics, and (3) basins not significantly affected by the 2008 Wenchuan Earthquakes (Figures DR7-8, Tables DR8-9).

Depending on D_{mf}, similarities between mean K from small basins with different lithologic groups varies. For $D_{mf} > 15$ km, we find no significant differences in mean K for small basins from different lithologies, but there is a statistically significant difference between mean K from siliciclastic sedimentary rock and those from plutonic rocks for $D_{mf} \leq 15$ km. Lastly, the modeled relation

between E and k_{sn} is significantly improved when we consider K varying with D_{mf}, but not with different lithologic groups (F-test, p <0.05) (Table DR9).

All eight sites where Schmidt Hammer measurements were performed are within 15 km of major faults. We show the average and 2 s.d. of all measurements and rock type descriptions from each location in Table S13 and show the spread of the data using box plots in Fig. 2.14. The Pengguan metamorphic complex site has an H-value of 48 ± 18 (2 s.d.). The two sites composed of carbonate rocks (Permian limestone) have H-values of 44 ± 19 and 53 ± 10. The five locations where we obtain measurements for mixed composition sedimentary rock have values of 24 ± 24, 30 ± 22, 26 ± 23, 26 ± 21, and 24 ± 15 (Table S2.8, Figure 2.14, Figure 2.15). All values from measurements taken on mixed composition sedimentary rocks lie within two standard deviations of each other. The results of Schmidt hammer H-values indicate that the mean, median, and maximum values from the metamorphic rock site and carbonate rock sites are higher than those from mixed composition sedimentary rock sites. Since we have not calibrated our H-values with the compressive or tensile rock strength measurements in the laboratory (e.g., Murphy et al., 2016), our measured H-values should be considered to represent the relative strengths of rocks at these sites.

2.4 Discussion and conclusions

Our results indicate that a wide zone (~15 km) of fault damage significantly impacts erosion coefficients in eastern Tibet, which is consistent with theoretical and numerical studies that emphasize the control of fault damage on erosion and topography (Koons et al., 2012; Roy et al., 2015; Roy et al., 2016). For example, strain generated by faulting may be expressed as newly formed cracks with lengths and density increasing towards faults (Molnar et al., 2007). Bedrock

near active or inactive faults that accumulated damage over time is readily detached and transported by erosional processes and significantly influences landscape forms and patterns (Duvall et al., 2020). Considering that most major faults mapped in this area are active, our results are likely derived from impacts of active faults with potential contributions from inactive faults. However, our observed ~15 km width around faults is larger than the typical length scale of fault-damage zones characterized by seismic velocity reduction (e.g., 100-1500 m) (Huang et al., 2014) or slow-moving landslide distributions (e.g., 2000 m) (Scheingross et al., 2013). This indicates that the impact of tectonic deformation may go beyond localized fault-zone cores, which is likely due to combined effects from secondary fault systems or coseismic ground shaking (Figures DR2, DR3, and DR9) (Molnar, 2007; Faulkner et al., 2010; Pelties et al., 2015; Ben-Zion and Zalipin, 2019). Seismic shaking from large magnitude earthquakes (>M_w 6.5) can enhance erosion by generating widespread coseismic landslides (Li et al., 2018). In fact, most coseismic landslides from the Wenchuan earthquake occurred within ~30 km of the Beichuan-Yingxiu fault surface rupture (Xu et al., 2014). Based on analysis using these coseismic landslides, Gallen et al. (2015) showed that fractured or weathered bedrock due to high active fault density and precipitation rates may lower rock cohesive strengths (~65%) near the fault. This is similar to the 71% reduction in overall tensile strength in bedrock inferred from a factor of two increase in erodibility (Sklar and Dietrich, 2001). However, we observed high *K* values at locations beyond the frontal Longmen Shan, such as the Min Shan which has complex fault systems consisting of both thrust and strike-slip faults, along which several M_w 6 earthquakes occurred (Xu et al., 2017) (Figures 1B and DR3D). This implies that in addition to seismic shaking from earthquakes, long-term plastic deformation of bedrock can be pervasive near major fault zones due to complex fault geometry, kinematics, and tectonic histories.

Our results show that *K* from siliciclastic sedimentary rocks are statistically higher than those from plutonic rocks near major faults, which is similar to results obtained via Schmidt Hammer rebound measurements (Data Repository, Figures DR10-11, Table DR10). This may imply that impacts of fault damage on *K* vary with intrinsic strengths of lithologies. For example, clastic sedimentary rocks often have layered structures and low intrinsic rock strengths (Hoek and Brown, 1997), thus they will be more easily fractured due to static and dynamic stress perturbations near fault zones and likely produce fine-grained sediments which are easier to erode or transport (Stock and Montgomery, 1999; Stock et al., 2005). This may explain the pronounced impact of tectonic damage on *K* in siliciclastic sedimentary rocks from the northeastern region. However, the limited number (n = 12) and coverage (D_{mf} <32 km) of basins dominated by plutonic rocks precludes strong conclusions.

We acknowledge that our fault compilation and data analysis have limitations. First, our compilation may not be complete since there are likely unrecognized faults due to the long recurrence interval of earthquakes or inaccessibility of field sites. Second, we did not examine impacts from different fault geometries or kinematics due to limited data and complex reactivation histories in this region (e.g., Burchfiel et al., 1995). Certain fault geometries or types (e.g., hanging walls vs. footwalls of thrusts, restraining vs. releasing bends of strike-slip faults) may result in different extents and degrees of fault damage. Third, the quality of locations and geometry of faults varies due to uneven data quality of cited studies. Despite these limitations, our fault compilation provides information on the proximity of faults and allows us to recognize the impact of fault damage on erosion and topography in eastern Tibet.

2.4.1 Future work and importance

Our finding implies that the influence of fault damage need to be considered to model surface processes and examine feedbacks between tectonic deformation and landscape evolution in tectonically active areas (Koons et al., 2012; Roy et al., 2015; Roy et al., 2016). Future studies with more extensive field measurements, detailed information on faults, and increased spatial coverage and number of basins with uniform rock types will help to further clarify the interaction between fault damage, surface processes, and landscape evolution.

2.5 Figure Captions

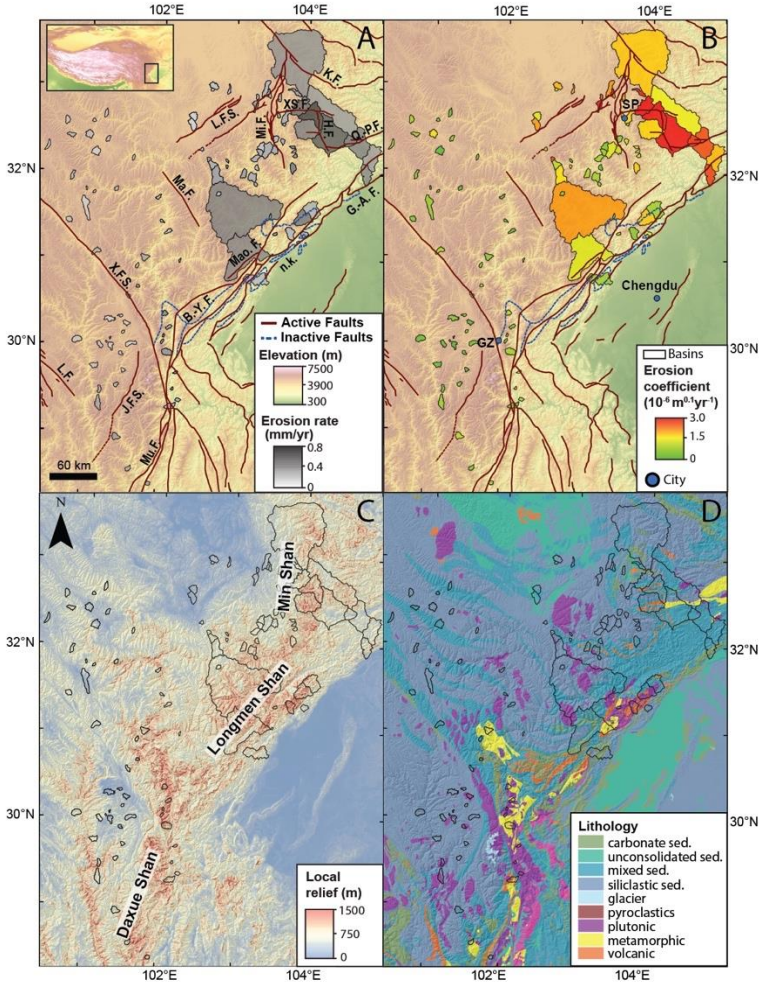

Figure 2.1. Maps of eastern Tibet showing elevation with sampled basins color-coded by (A) ^{10}Be-derived erosion rates and (B) erosion coefficients, (C) local relief within a 1 km radius circular moving window, and (D) lithology from Hartmann and Moosdorf (2012). The box in the inset map in A shows our study area. Major active and inactive faults are shown with solid brown and dashed blue lines, respectively. Brown dashed lines show active faults for which the last activity is unclear. Full names and detailed information about our fault compilation are in the Data Repository.

Locations of Songpan (SP), Ganze (GZ), and Chengdu are shown with blue dots in B. Mountain range names are shown in C.

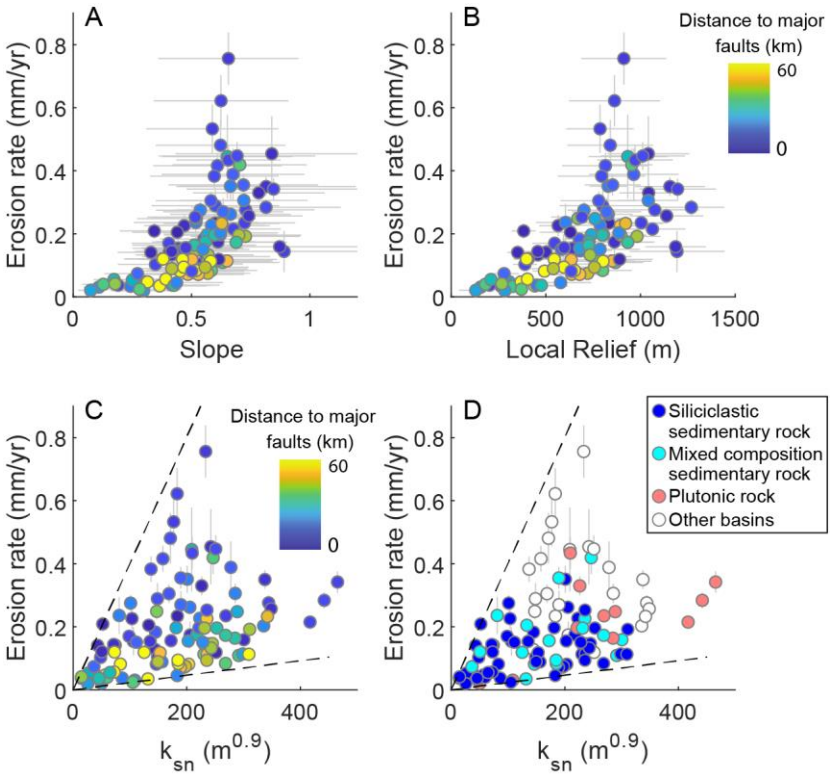

Figure 2.2. Erosion rates versus (A) slope, (B) local relief with a 1 km radius range, and C, D) k_{sn} color-coded by (C) distance to major faults and (D) dominant lithologic groups. Blue, cyan, and salmon circles in D represent small basins dominated by siliciclastic sedimentary, mixed composition sedimentary, and plutonic rocks, respectively. White circles show all other basins, including those with areas >200 km^2. Long dash lines show the minimum and maximum slope ranges for the linear fit. At similar values of topographic metrics, basins near faults have higher erosion rates than those farther from faults.

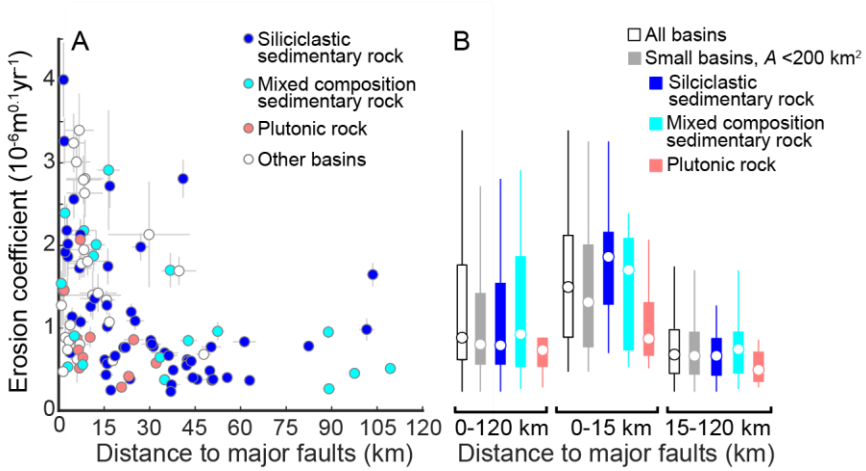

Figure 2.3. (A) Erosion coefficient versus distance to major faults, color-coded for small basins dominated by different lithologic groups. (B) Boxplots showing erosion coefficient ranges from different lithologies grouped by distance to major faults (D_{mf}). All basins, small basins (area <200 km^2), and small basins dominated by siliciclastic sedimentary, mixed composition sedimentary, and plutonic rocks are shown in white, gray, blue, cyan, and salmon, respectively. The line, box, and circle show the extent within 99.3%, the 25th and 75th percentiles, and the median, respectively. On average, erosion coefficients are ~2 times higher for basins with D_{mf} ≤15 km than those >15 km.

2.6 References

Allen, C.R., Zhouli, L, Hong, Q., Xueze, W., Huawei, Z., and Weishi, H., 1991, Field study of a highly active fault zone: The Xianshuihe fault of southwestern China: Geological Society of America Bulletin, v. 103, p.1178–1199, doi:10.1016/j.quageo.2007.12.001.

Ansberque, C., Godard, V., Bellier, O., Sigoyer, J.D., Liu-Zeng, Xu, X. Ren, Z., Li, Y., and A.S.T.E.R. Team, 2015, Denudation pattern across the Longriba fault system and implications for the geomorphological evolution of the eastern Tibetan margin: Geomorphology, v. 246, p. 542–557, doi:10.1016/j.geomorph.2015.07.017.

Aydin, A., and Basu, A., 2005, The Schmidt hammer in rock material characterization: Engineering Geology, v.81, no.1, p. 1-14.

Balco, G., Stone, J.O., Lifton, N.A., and Dunai, T.J., 2008, A complete and easily accessible means of calculating surface exposure ages or erosion rates from 10Be and 26Al measurements: Quaternary Geochronology, v. 3, p. 174–195, doi:10.1016/j.quageo.2007.12.001.

Ben-Zion, Y. and Zalipian, I., 2019, Spatial Variations of rock damage production by earthquakes in southern California: Earth and Planetary Science Letters, v. 152, p. 184-193. doi:10.1016/j.epsl.2019.02.006

Bierman, P. and Steig, E.J., 1996, Estimating rates of denudation using cosmogenic abundances in sediment: Earth Surface Processes and Landforms, v. 21, p. 125–139.

Bookhagen, B, and Burbank, D.W., 2010, Toward a complete Himalyan hydrologic budget: Spatiotemporal distribution of snowmelt and rainfall and their impact on river discharge: Journal of Geophysical Research, v. 115, F03019, p. 1-25, doi:10.1029/2009JF001426.

Burchfiel, B.C., and Chen, Z., 2013, Tectonics of the Southeastern Tibetan Plateau and Its Adjacent Foreland: Geological Society of America Special Paper 210, 164 p. doi:10.1130/MEM210

Burchfiel, B.C., Zhiliang, C., Yupinc, L., and Royden, L.H., 1995, Tectonics of the Longmen Shan and Adjacent Regions, Central China Tectonics of the Longmen Shan and Adjacent Regions, Central China: International Geology Review, v. 37, no. 8, p.661–735, doi: 10.1080/00206819509465424.

Chen, S. F., and Wilson, C. J. L., 1996, Emplacement of the Longmen Shan Thrust-Nappe Belt along the eastern margin of the Tibetan Plateau: Journal of Structural Geology, v. 18, no. 4, p. 413–430. doi: 10.1016/0191-8141(95)00096-V.

Chen, S.F., Wilson, C.J.L, Deng, Q.D., Zhao, X.L., and Luo, Z.L., 1994, Active faulting and block movement associated with large earthquakes in the Min Shan and Longmen Mountains, northeastern Tibetan Platea: Journal of Geophysical Research, v. 99, no. B12, p. 24025–24038.

Chevalier, M.-L., Leloup, P.H., Replumaz, A., Pan, J., Liu, D., Li, H, Gourbet, L, and Métois, M., 2016, Tectonic-geomorphology of the Litang fault system, SE Tibetan Plateau, and implication for regional seismic hazard: Tectonophysics, v. 682, p. 278-292. doi: 10.1016/j.tecto.2016.05.039.

de Ferranti, J.: Digital elevation data, Url: http://www. viewfinderpanoramas.org/dem3.html, accessed on 18 October 2018.

Didan, K., 2015, MOD13Q1 MODIS/Terra Vegetation Indices 16-Day L3 Global 250m SIN Grid V006. NASA EOSDIS Land Processes DAAC. (accessed 2019-08-29 from https://search.earthdata.nasa.gov)

Dunai, P.T., 2010, Cosmic ray-produced radionuclides in Earth Sciences Primary Nature: High-energy charged particles: Cambridge, Cambridge University Press, 14 p.

Duvall, A. R., Harbert, S. A., Upton, P., Tucker, G. E., Flowers, R. M., and Collett, C., 2020, River patterns reveal two stages of landscape evolution at an oblique convergent margin, Marlborough Fault System, New Zealand: Earth Surface Dynamics, v. 8, p. 177–194, doi:10.5194/esurf-8-177-2020.

Faulkner, D.R., Jackson, C.A.I., Lunn, R.J., Schlische, R.W., Shipton, Z.K., Wibberley, C.A.J., and Withjack, M.O., 2010, A review of recent developments concerning structure, mechanics, and fluid properties of fault zones: Journal of Structural Geology, v. 32, p. 1557-1575.

Flint, J.J., 1974, Stream Gradient as a Function of Order, Magnitude, and Discharge: Water Resources Research, v. 10, no. 5, p. 969-973.

Gallen, S.F., Clark, M.K., and Godt, J.W., 2015, Coseismic landslides reveal near-surface rock strength in a high-relief, tectonically active setting: Geology, v. 43, no. 1, p.11–14, doi:10.1130/G36080.1.

Godard, V., Lave, J. Carcaillet, J., Cattin, R., Bourles, D., and Zhu J., 2010, Spatial distribution of denudation in Eastern Tibet and regressive erosion of plateau margins: Tectonophysics, v. 491. p. 253–274. doi:10.1016/j.tecto.2009.10.026.

Granger, D.E., Kirchner, J.W., Finkel, R., 1996, Spatially Averaged Long-Term Erosion Rates Measured from in Situ-Produced Cosmogenic Nuclides in Alluvial Sediment, The Journal of Geology v. 104, p. 249-257.

Hallet, B. and Hunter, L., 1996, Rates of erosion and sediment evacuation by glaciers: A review of field data and their implication: Global and Planetary Change, v. 12, p. 213–235.

Hartmann, J. and Moosdorf, N., 2012, The new global lithological map database GLiM: A representation of rock properties at the Earth surface: Geochemistry, Geophysics, Geosystems, v. 13, no. 12, p. 1–37.

Hoek, E., and Brown, E.T, 1997, Practical estimates of rock mass strength: International Journal of Rock Mechanics and Mining Sciences, v. 34, no. 8, p. 1165–1186, doi:10.1016/S0969-4765(04)00066-9.

Howard, A.D. and Kerby, G., 1983, Channel changes in badlands: Geological Society of America Bulletin, v. 94, p. 739-752.

Howard, A.D., Dietrich, W.E., and Siedl, M.A., 1994, Modeling fluvial erosion on regional to continental scales: Journal of Geophysical Research, v. 99, no. B7, p. 13971-13986.

Huang, Y., Ampuero, J.-P., and Helmberger, D.V., 2014, Earthquake ruptures modulated by waves in damaged fault zones: Journal of Geophysical Research, Solid Earth, v. 119, p. 3133 – 3154. doi:10.1002/2013JB010724.

International Seismological Centre, 2019, ISC-GEM Earthquake Catalogue: https://doi.org/10.31905/d808b825.

Kirby, E. and Ouimet, W.B., 2011, Tectonic geomorphology along the eastern margin of Tibet: insights into the pattern and processes of active deformation adjacent to the Sichuan Basin: Geological Society, London, Special Publications, v. 353, no. 1, p.165–188, doi:10.1144/SP353.9.

Kirby, E., Reiners, P.W., Krol, M.A., Whipple, K.X., Hodges, K.V., Farley, K.A., Tang, W., Chen, Z., 2002, Late Cenozoic evolution of the eastern margin of the Tibetan Plateau: Inferences from 40Ar/39Ar and (U-Th)/He thermochronology: Tectonics, v. 21, no. 1001, p. 1-20.

Kirby, E., Whipple, K.X., Burchfiel, B.C., Tang, W., Berger, G., Sun, Z., and Chen, Z., 2000, Neotectonics of the Min Shan: Implications for mechanisms driving Quaternary deformation along the eastern margin of the Tibetan Plateau: Geologic Society of America Bulletin, v. 112, no. 3, p. 375–393, doi:10.1144/SP353.9.

Koons, P.O., Upton, P. and Barker, A.D, 2012, The influence of mechanical properties on the link between tectonic and topographic evolution: Geomorphology, v. 137, no. 1, p. 168-180.

Lal, D., 1991, Cosmic ray labeling of erosion surfaces: in situ nuclide production rates and erosion models: Earth and Planetary Science Letters, v. 104, p. 424–439.

Li, G., West, A.J., Densmore, A., Jin, Z., Zhang, F., Wang, J., Clark, M., and Hilton, R.G., 2017, Earthquakes drive focused denudation along a tectonically active mountain front: Earth and Planetary Science Letters, v. 472, p. 253-265.

Lifton, N., Sato, T., and Dunai, T.J., 2014, Scaling in situ cosmogenic nuclide production rates using analytical approximations to atmospheric cosmic-ray fluxes: Earth and Planetary Science Letters, v. 386, p. 149-160.

Long, F., Wen, X.Z., Ruan, X., Zhao, M., and Yi, G.X., 2015, A more accurate relocation of the 2013 Ms7.0 Lushan, Sichuan, China, earthquake sequence, and the seismogenic structure analysis: Journal of Seismology, v. 19, p. 653-665. doi: 10.1007/s10950-015-9485-0.

Molnar, P., Anderson, R.S. and Anderson, S.P., 2007, Tectonics, fracturing of rock, and erosion: Journal of Geophysical Research: v. 112, no. F03014, p.1–12, doi:10.1029/2005JF000433.

Murphy, B.P., Johnson J.P.L., Gasparini, N.M., and Sklar L.S., 2016, Chemical weathering as a mechanism for the climatic control of bedrock river incision: Nature, v. 532, p. 223-227.

Niemi, N.A., Oskin, M., Burbank, D.W., Heimsath, A.M., and Gabet, E.J., 2005, Effects of bedrock landslides on cosmogenically determined erosion rates: Earth and Planetary Science Letters, v. 237, p. 480–498.

Nishiizumi, K., Imamura, M., Caffee, M.W., 2007, Absolute calibration of 10Be AMS standards: Beam Interactions with Materials and Atoms, v. 258. p. 403-413, doi: 10.1016/j.nimb.2007.01.297

Ouimet, W.B., Whipple, K.X., and Granger, D.E., 2009, Beyond threshold hillslopes: Channel adjustment to base-level fall in tectonically active mountain ranges: Geology, v. 37, no. 7, p. 579–582, doi: 10.1130/G30013A.1.

Pan, G., Ding, J., Yao, D., Wang, L., Luo J., Yan Y., Yong, Y., Zheng, J., Liang, X., Qin, D., Jiang, X., Wang, Q., Li, R., Geng, Q., Liao, Z., and Zhu, D., 2004, Geological map of the Qinghai-Tibet Plateau and adjacent areas: Chengdu Map Publishing House, scale 1:1,500,000, 6 sheets.

Pelties, C., Huang, Y., and Ampuero, J. P., 2015, Pulse-like rupture induced by three-dimensional fault zone flower structures: Pure and Applied Geophysics, v. 172, no. 5. p. 1229-1241.

Portenga, E.W., and Bierman, P.R., 2011, Understanding Earth's eroding surface with 10Be: GSA Today, v. 21, no. 8, p. 4-10.

Ren, J., Xu, X., Yeats, R.S., and Zhang, S., 2013a. Latest Quaternary paleoseismology and slip rates on the Longriba fault zone, eastern Tibet: Implications for fault behavior and strain partioning: Tectonics, v. 32, no. 2, p. 216-238. doi: 10.1002/tect.20029.

Ren, J., Xu, X., Yeats, R.S., Zhang, S., Ding, R., and Gong, Z., 2013b. Holocene paleoearthquakes of the Maoergai fault, eastern Tibet: Tectonophysics, v. 590, p. 121-135. doi: 10.1016/j.tecto.2013.01.017.

Ren, J., Xu, X., Zhang, S., Yeats, R.S., Chen, J., Zhu, A., and Liu, S., 2018. Surface rupture of the 1933 M 7.5 Diexi earthquake in eastern Tibet: implications for seismogenic tectonics: Geophysical Journal International, v. 212, p. 1627-1644. doi: 10.1093/gji/ggx498.

Roy, S.G. Koons, P.O., Upton, P., and Tucker, G.E., 2015, The influence of crustal strength fields on the patterns and rates of fluvial incision: Journal of Geophysical Research: Earth Surface, v. 120, p. 275–299, doi:10.1002/2014JF003281.

Roy, S.G., Tucker, G.E., Koons, P.O., Smith, S.M., and Upton, P., 2016, A fault runs through it: Modeling the influence of rock strength and grain-size distribution in a fault-damaged landscape: Journal of Geophysical Research: Earth Surface, v. 121, p. 1911–1930. doi:10.1002/2015JF003662.

Scheingross, J. S., Minchew, B. M., Mackey, B. H., Simons, M., Lamb, M. P., and Hensley, S., 2013, Fault-zone controls on the spatial distribution of slow-moving landslides: GSA Bulletin, v.125, no. 3-4, p. 473-489, doi: 10.1130/B30719.1.

Scherler, D., Dibiase, R.A., Fisher, G.B., and Avouac, J.-P., 2017, Testing monsoonal controls on bedrock river incision in the Himalaya and Eastern Tibet with a stochastic-threshold stream power model: Journal of Geophysical Research: Earth Surface, v. 122, p. 1389–1429, doi:10.1002/2016JF004011.

Schwanghart, W. and Scherler, D., 2014, Short Communication: TopoToolbox 2 – MATLAB-based software for topographic analysis and modeling in Earth surface sciences: Earth Surface Dynamics, v. 2, p.1–7, doi:10.5194/esurf-2-1-2014.

Sklar, L.S. and Dietrich, W.E., 2001, Sediment and rock strength controls on river incision into bedrock: Geology, v. 28, no. 12, p.1087–1090.

Stock, J.D. and Montgomery, D.R., 1999, Geologic constraints on bedrock river incision using the stream power law: Journal of Geophysical Research, v. 104, no. B3, p. 4983-4993.

Stock, J.D., Montgomery, D.R., Collins, B.D., Dietrich, W.E., Sklar, L., 2005, Field measurements of incision rates following bedrock exposure: Implications for process controls on long profiles of valleys cut by rivers and debris flows: Geological Society of America Bulletin, v. 117, no. 11/12, p. 174-194.

Stone, J.O., 2000, Air pressure and cosmogenic isotope production: Journal of Geological Society of London, v. 105, no. B10, p.753–759.

Taylor, M. and Yin, A., 2009. Active structures of the Himalayan-Tibetan orogen and their relationships to earthquake distribution, contemporary strain field, and Cenozoic volcanism: Geosphere, v. 5, no. 3, p.199–214. doi: 10.1130/GES00217.1.

Tian, Y., Li, R., Tang, Y, Xu, X, Wang, Y, and Zhang, P., 2018, Thermochronological constraints on the late Cenozoic morphotectonic evolution of the Min Shan, the eastern margin of the Tibetan Plateau: Tectonics. v. 37, no. 6, p. 1733-1749, doi:10.1029/2017TC004868.

U.S. Geological Survey, 2017, ShakeMap – Earthquake Ground Motion and Shaking Intensity Maps: U.S. Geological Survey, doi: 10.5066/F7W957B2.

von Blanckenburg, F., 2005, The control mechanisms of erosion and weathering at basin scale from cosmogenic nuclides in river sediment: Earth and Planetary Science Letters, v. 237, no. 3-4, p. 462-479.

Wang, E., Kirby, E., Furlong, K.P., van Soest, M., Xu, G., Shi, X., Kamp, P.J.J., and Hodges, K.V., 2012. Two-phase growth of high topography in eastern Tibet during the Cenozoic: Nature Geoscience, v. 5, p. 640-645. doi: 10.1038/NGEO1538.

West, A.J., Hetzel, R., Li, G., Jin, Z., Zhang, F., Hilton, R.G., and Densmore, A.L., 2014, Dilution of 10Be in detrital quartz by earthquake-induced landslides: Implications for determining denudation rates and potential to provide insights into landslide sediment dynamics: Earth and Planetary Science Letters, v. 396, p. 143-153.

Whipple, K.X. and Tucker, G.E., 1999, Dynamics of the stream-power river incision model: Implications for height limits of mountain ranges, landscape response timescales, and research needs: Journal of Geophysical Research, v. 104, no. B8, p. 17661-17674.

Xu, C., Xu, X., Yao, X., Dai, F., 2014, Three (nearly) complete inventories of landslides triggered by the May 12, 2008 Wenchuan Mw 7.9 earthquake of China and their spatial distribution statistical analysis: Landslides, v. 11, p. 441–461, doi:10.1007/s10346-013-0404-6.

Xu, X., Gao, R., Guo, X., Li, W., Li, H., Wang, H., Huang, X, and Lu, Z., 2017, Outlining tectonic inheritance and construction of the Min Shan region, eastern Tibet, using crustal geometry: Scientific Reports, v. 7, no.13798, p.1–8, doi:10.1038/s41598-017-14354-4.

Yan, D.-P., Qiu, L., Wells, M.L., Zhou, M.-F., Meng, X., Lu, S., Zhang, S., Wang, Y., and Li, S.-B., 2018, Structural and Geochronological Constraints on the Early Mesozoic North Longmen Shan Thrust Belt: Foreland Fold-Thrust Propogation of the SW Qinling Orogenic Belt, Northeastern Tibetan Plateau: Tectonics, v. 37, no. 12, p. 4595-4624. doi: 10.1029/2018TC004986.

Yan, D.-P., Zhou, M.-F., Li, S.-B., and Wei, G.-Q., 2011, Structural and geochronological constraints on the Mesozoic-Cenozoic tectonic evolution of the Longmen Shan thrust belt, eastern Tibetan Plateau: Tectonics, v. 30, TC6005, p. 1-24. doi: 10.1029/2011TC002867.

Zhang, Y., Replumaz, A., Leloup, P.H., Wang, G., Bernet, M., van der Beek, P., Paquette, J.L. and Chevalier, M., 2017, Cooling history of the Gongga batholith: Implications for the

Xianshuihe Fault and Miocene kinematics of SE Tibet: Earth and Planetary Science Letters, v. 465, p. 1–15, doi:10.1016/j.epsl.2017.02.025.

Zhang, Y.-Z., Replummaz, A., Wang, G.-C., Leloup, P.H., Gautheron, C., Bernet, M., van der Beek, P., Paquette, J.L., Wang, A., Zhang, K.-X., Chevalier, M.-L., and Li, H.-B., 2015, Timing and rate of exhumation along the Litang fault system, implication for fault reorganization in Southeast Tibet: Tectonics, v. 34, p. 1219-1243. doi: 10.1002/ 2014TC003671.

Chapter 3: Temperature and co-crystallization effects on Zr isotopes: A case study of the La Posta igneous complex

Note: This chapter is modified from Kirkpatrick, H.M., Harrison, T.M., Bell, E.A., Tissot, F.L.H., MacLennan, S.A., and Ibanez-Mejia, M., Temperature and co-crystallization effects on Zr isotopes: A case study of the La Posta igneous complex, *Submitted to Geochimica Cosmochimica Acta*.

3.1 Introduction

While Zr was once considered to be isotopically uniform in both terrestrial and extraterrestrial materials (Minster and Ricard, 1981; Minster and Allègre, 1982; Hirata and Yamaguchi, 1999; Hirata, 2001), mass-independent (Schönbächler et al., 2003; Schönbächler et al., 2005; Akram et al., 2013) and mass-dependent isotopic variations have since been documented in igneous materials both at the crystal-scale (Ibañez-Mejia and Tissot, 2019; Zhang et al., 2019; Guo et al., 2020; Huang et al., 2021) and bulk rock-scale (Iizuka et al., 2016; Inglis et al., 2018; Inglis et al., 2019; Feng et al., 2020; Tian et al., 2020; Wu et al., 2020), and have thus become the focus of sustained attention as a potential tracer of igneous processes. While Zr^{4+} typically occurs in 6-fold coordination in silicate liquids (Farges et al., 1991; Louvel et al., 2013), it is 8-fold coordinated in zircon (Robinson et al., 1971), the host of most Zr in crustal rocks (Bea et al., 2006), resulting in relatively short, stiff bonds. For this reason, mass-dependent equilibrium Zr isotope fractionation is expected to preferentially partition the light isotope ^{90}Zr relative to ^{94}Zr in zircon, driving the melt to isotopically heavier values with increasing differentiation. A positive correlation reported by Inglis et al. (2018) between whole rock $\delta^{94/90}Zr$ and SiO_2 content among igneous rock standards

appeared to yield what would be expected if light Zr isotopes are preferentially fractionated into the solid.

Subsequent studies examining Zr isotope variations in natural zircons (Ibañez-Mejia and Tissot, 2019; Tompkins et al., 2020; Guo et al., 2020) and bulk rock samples (Inglis et al., 2019) reported differing apparent fractionation factors. At the bulk-rock scale, Inglis et al. (2019) found a positive correlation between Zr stable isotope values and whole rock SiO_2 for rocks above zircon saturation at Hekla volcano (Iceland), suggesting that Zr stable isotopes may track magmatic differentiation. However, at the mineral scale, zircons from the Duluth complex anorthosite (Ibañez-Mejia and Tissot, 2019) revealed >5‰ $\delta^{94/90}$Zr variations that were attributed to a Rayleigh-like removal of isotopically heavy zircon. Subsequently, Tompkins et al. (2020) found no resolvable intra-crystalline variability in a zircon megacryst from the Mud Tank carbonatite from which they inferred that no isotopic fractionation had occurred during zircon crystallization. These three studies imply values for zircon-melt fractionation ($\alpha_{zircon\text{-}melt}$) factors of +1‰ (Ibañez-Mejia and Tissot; 2019), 0 ‰ (Tompkins et al., 2020) and –0.5 ‰ (Inglis et al., 2019). Even more perplexing is the observation of $\delta^{94/90}$Zr variations from +1 to −4‰ in co-existing magmatic zircons (Ibañez-Mejia and Tissot, 2019). Guo et al. (2020) used intra-crystalline $\delta^{94/90}$Zr zoning in zircons from the Gangdese batholith to infer variable $\alpha_{zircon\text{-}melt}$ values less than unity, which they hypothesized reflect the strong temperature dependence of the equilibrium isotopic fractionation factor. To address these conflicting results, Chen et al. (2020) and Méheut et al., (2021) theoretically investigated possible vibrational equilibrium fractionation and nuclear field shift effects, but both predict isotopic variations more than an order of magnitude smaller than those observed in natural samples. Both studies suggested that kinetic effects in diffusive boundary layers that developed

during the crystallization of silicate magmas could provide a viable mechanism for producing ‰-scale $\delta^{94}Zr/^{90}Zr$ variations recorded in zircon.

Few phases besides zircon have previously been measured for Zr isotopes resulting in a lack of knowledge surrounding the effects of co-crystallization of zircon with other Zr-hosting phases. This study investigates these possible effects, by determining isotopic variations not only of zircon but also of other accessory and rock-forming phases in a differentiated plutonic complex. Specifically, we investigate $\delta^{94/90}Zr$ variations in the La Posta igneous suite, an intermediate to felsic suite of granitoids in the eastern Peninsular Ranges of southern California to find systematic controls on Zr isotopic variations.

3.2. The La Posta plutonic suite

The Peninsular Ranges batholith, which extends ~800 km from south of the Transverse Ranges in southern California through portions of Baja California, formed by Cretaceous arc magmatism (Fig. 3.1). The batholith is broadly calcic in nature (Silver et al., 1979) with compositions varying from gabbroic to granitic (Silver and Chappell, 1988). The Peninsular Ranges batholith has a distinct geochemical and petrologic step (the "I-S line") which strikes N-NW along much of its length and reflects: 1) chemical and isotopic compositional differences (Todd and Shaw, 1985; Silver and Chappell, 1988); 2) the magnetite-ilmenite line (Gastil et al., 1990); and 3) age differences (Krummenacher and Doupont, 1975; Silver et al., 1979; Silver and Chappell, 1988; Walawender et al., 1990; Grove et al., 2003; Ortega-Rivera, 2003; Miggins et al., 2014; Premo et al., 2014; Shaw et al., 2014).

Large, internally-zoned felsic bodies, of which the La Posta suite is the largest, dominate the eastern portion of the batholith (Gastil et al., 1975). These plutons formed by voluminous (75-100 km^3/km of batholith strike length/Ma) emplacement of magmas between 98 Ma and 93 Ma (Silver

and Chappell, 1988; Kimbrough et al., 2001; Grove et al., 2003). The La Posta pluton is concentrically zoned with whole rock SiO_2 values increasing inwards (Clinkenbeard and Walawender, 1989). The La Posta suite his characterized by ASI (aluminum saturation index: $Al_2O_3/(CaO + Na_2O + K_2O)$ (Zen, 1986) values of 0.94 to 1.20, initial $^{87}Sr/^{86}Sr$ of 0.70383 to 0.70563, and $\delta^{18}O$ ranging from 7.2 ‰ to 11 ‰, all indicative of a felsic source with variable sediment assimilation (Shaw et al., 2003). The suite is divided into five units ranging from banded border facies (Clinkenbeard and Walawender, 1989) to a muscovite-biotite granodiorite core with gradational contacts over tens of meters among the inner four units (Walawender et al., 1990). The four units explored here, hornblende-biotite facies, large biotite facies, small biotite facies, and muscovite-biotite facies, contain ilmenite and hornblende and titanite are common in the three outer units (Clinkenbeard and Walawender, 1989) (Fig. 3.2 and 3.3).

Zircons from the muscovite-biotite unit have high oxygen isotope ratios, lower redox state (Trail et al., 2011), and higher P concentrations than the outer units, which is consistent with it having assimilated significant pelitic sediment (Bell and Kirkpatrick, 2021). Zircons from the small and large biotite-facies units have lower oxygen isotope ratios and P concentrations, indicative of less sediment assimilation (Bell and Kirkpatrick, 2021). Zircons from the hornblende-biotite unit have higher Th/U, U/Yb, and Eu/Eu* indicating deeply forming magmas that experienced shallow fractionation (Bell and Kirkpatrick, 2021). The large- and small-biotite units display Eu/Eu* and Th-U/Yb values which fall between the inner and outmost La Posta units and generally display less clear fractionation trends. From this evidence, Bell and Kirkpatrick (2021) argue that magma mingling was important in the formation of the La Posta suite.

3.3. Zr distribution in granitoid rocks

While zircon is the principal Zr host in intermediate to felsic rocks, other minerals can accommodate Zr in their structures at relatively high concentrations. Bea et al. (2006) found that titanite and amphiboles from calc-alkaline granitoids contain an average of ~900 ppm (n = 74) and 41 ppm Zr (n = 124), respectively. Both minerals can cause MREE (middle rare earth element) depletion in coexisting melt (Simmons and Hedge, 1978; Harper et al., 2004; Colombini et al., 2011) which can then be reflected in co-crystallizing zircon. Thus, we can potentially use these REE (rare earth element) signatures to understand the influence of titanite and amphibole crystallization on zircon chemistry.

Colombini et al. (2011) examined REE patterns for glasses, whole rocks, and titanite from the Highland Range volcanic sequence of southern Nevada. They found that titanite in evolved melts can have a K_d (partition coefficient measured as the concentration of the solid divided by the concentration of the melt) greater than 1,000 for the MREE, which is generally higher than those partition coefficients in coexisting zircon. In addition, they found a rimward depletion in MREE in titanite indicating a depletion of MREE in the melt during crystallization and apparent partition coefficients for Zr into titanite between 7 and 11. Ti-in-zircon (Ferry and Watson, 2007) and Zr-in-titanite thermometry (Hayden et al., 2008) of these samples indicate relatively late crystallization.

3.4. Methods

3.4.1 Sample collection and preparation

La Posta rocks were collected during four field visits between November 2018 and August 2021 (Table S1; Fig. 3.1). They were initially processed using a jaw crusher and powdered with a disk mill. Once a whole rock split had been procured, the powder was sieved to <250 μm and that fraction panned to acquire the heavy mineral component. A non-magnetic fraction was obtained

via a Frantz magnetic separator and a heavy concentrate obtained using heavy liquids. Zircons were then picked from the heavy mineral separate and mounted onto double sided adhesive tape and fashioned into 1" epoxy disks. These discs were polished using SiC, diamond, and/or Al_2O_3 until the mount was optically flat. Whole rock sample preparation and XRF (x-ray fluorination) measurements were undertaken at Pomona College following the procedures of Poletti et al. (2016).

3.4.2 Zr isotopic measurements by SIMS

In order to measure variations in stable isotope ratios, at least two stable and abundant isotopes that are not interfered by adjacent peaks are required. Both ^{90}Zr and ^{94}Zr are abundant and stable. No interferences at these masses were found when high-resolution scans of both ^{90}Zr and ^{94}Zr on the *ims*1290 (mass resolving power ~18000) were performed and were therefore used for our measurements. Most mounts also included Mud Tank zircon standard, which is homogenous in $\delta^{94/90}Zr$ (Tompkins et al., 2020).

In situ isotopic measurements were undertaken during three sessions using the CAMECA *ims*1290 with the Hyperion II source (Liu et al., 2018). The first session mainly involved analysis of isotopic reference materials with the latter two sessions primarily focused on analysis of La Posta samples. During the October 2018 and June 2019 session, we used a 5 µm raster, and during the September 2019 session, no raster was used. Analyses were performed using an O^{3-} or O^- beam in multicollection mode. During the October 2018 and June 2019 sessions, we measured three masses: ^{90}Zr [C, FC], ^{94}Zr [H1, FC], and a dummy background mass. During the September 2019 session, we measured two masses: ^{90}Zr [C, FC] and ^{94}Zr [FC2, FC]. The first set of letters in each bracket denotes the specific detector where measurements were taken. All measurements were performed using a Faraday cup (FC). This change in procedure permitted better background

corrections. In the October 2018 and June 2019 sessions a ~15 to ~18 nA beam was used while the September 2019 session used a ~6 nA beam. These instrument conditions allowed for an ~8 μm spot in all sessions. Results are presented in $\delta^{94/90}$Zr notation defined as:

$$\delta^{94/90}Zr_{sample\ -standard} = \left(\left[\left({}^{94}Zr/{}^{90}Zr\right)_{sample} / \left({}^{94}Zr/{}^{90}Zr\right)_{standard}\right] - 1\right) \times 10^3 \quad (3.1)$$

where *standard* represents the value of NIST with Mud Tank zircon acting as our lab standard (Tompkins et al., 2020). $\delta^{94/90}$Zr for zircons were either calculated by assuming a linear change with analysis number (as a proxy for time; errors calculated using code from Mahon (1996)) of the Mud Tank zircon value to account for instrumental drift or taking the mean of all Mud Tank analyses in a session.

Following analysis, samples were examined for inclusions, topography, and cracks in backscatter mode on a Tescan Vega-3 XMU variable-pressure scanning electron microscope (SEM). Care was taken to ensure that inherited zircon cores were not analyzed. Imaging using the cathodoluminescence (CL) detector permitted internal structural details of the grains to be revealed.

3.4.3 In situ trace elements analyses

In-situ trace element analyses were performed on the CAMECA *ims*1270 (July 2020, December 2020) and *ims*1290 (December 2019). Measurements on both instruments followed the procedure outlined in Bell et al. (2016). After trace element analyses were performed, values with LREE-I <30 (light rare earth index; LREE-I =Dy/Nd+Dy/Sm) and Ti >30 ppm, both of which indicate likely alteration, were removed from further consideration (Bell et al., 2016; Bell et al., 2019). Most analysis spots for trace elements were targeted to be very near to or overlapping with Zr

isotope analytical spots, so trace element, U-Pb (discussed later), and Zr analyses can be directly correlated. For the Ti-in-zircon temperature calculations we used a Si activity (a_{Si}) of 1 as quartz is present in these rocks (Ferry and Watson, 2007). We represented the range of Ti-rich phases (titanite, ilmenite, rutile; Clinkenbeard and Walawender, 1989; this study) present in the these rocks with an a_{Ti} of 0.7 representing an average of the range expected for those phases from ~0.5 to 1.0 (Watson and Harrison, 2005; Reid et al., 2011). However, to understand the impact of Ti activity on temperature-dependent fractionation calculations, we also calculated Ti-in-zircon crystallization temperatures for $a_{Ti} = 1$. We computed the correlation between $\delta^{94/90}$Zr and various trace elements at the inter- and intragrain levels using standard statistical methods. To assess MREE depletion, we calculated a modified Gd/Gd* (Gd/√(Nd*Yb)) (Colombini et al., 2011).

3.4.4 In situ U-Pb analyses

We performed U-Pb measurements of zircon following the procedures outlined in Quidelleur et al. (1997) to ensure that inherited zircon cores were not included in our analyses. Measurements of our primary age standard, AS3 and FC1 (1099.1 Ma; Schmitz et al., 2003) were interspersed with every few unknown analyses to monitor instrument drift. All analyses with >95% radiogenic ^{206}Pb are included in the compilation and those with both >95% radiogenic ^{206}Pb and which are within 30% of concordance ($Age_{206/238}/Age_{207/235}$ x 100) are used when comparing ages with zircon isotopic composition. In addition to measurements of AS3 and FC1, we measured Plešovice (Oct, Dec), TanBra (Oct, NovC, Dec), 91500 (Oct, NovA, NovB, NovC), R33 (Oct, NovA, NovB, NovC), and OG1 (Oct, NovA) to assess accuracy. Lastly, mineral identification was performed through use of the energy-dispersive X-ray analysis attachment on the SEM and analysis of thin sections using a petrographic microscope.

3.4.5 Zr isotope analyses by double-spike MC-ICPMS:

For bulk rock analyses, half a gram of sample powder was mixed with 1 gram of trace metal grade Li tetraborate flux and 0.3 g of high-purity LiBr non-wetting solution. The mix was fluxed in high purity graphite crucibles at 1100 °C for 10 minutes, before being quenched in air at room temperature. The resulting glass beads were then fragmented and between 10 and 150 μg of clean fragments (i.e., away from the surface where graphite residues can be found) were dissolved in a volume of 3 M HNO_3 + 2 M HF calculated to dissolve the glass.

For mineral separates, handpicked grains were rinsed in a mild (1M) HCl solution for 3 hours at 75˚C, sonicated, and rinsed twice with MQ-H_2O prior to digestion. Full dissolutions were achieved using five steps: 1) samples were first attacked overnight using 3 ml of 28 M HF + 1 ml 16 M HNO3 at 130˚C on a hotplate, and then dried to a salt; 2) 4 ml of concentrated aqua regia were added and samples were fluxed overnight at 130˚C until no solids were visible, and then dried to a salt; 3) samples were attacked again using 3 ml of 28 M HF + 1 ml 16 M HNO3 at 130˚C for 48 hours, and then dried to a salt; 4) step 2 using concentrated aqua regia was repeated, and then dried to a salt; 5) 2 mL of 3 M HNO_3 + 0.4 M H_3BO_3 were added to completely re-digest any remaining fluoride salts. If a solid residue was still visible after fluxing overnight, an additional 2 ml of 3 M HNO_3 + 0.4 M H_3BO_3 were added. In all cases this procedure resulted in complete dissolution of the mineral fractions and fluoride salts. Samples were dried one last time to remove fluorine by the preferential production of volatile BF_3 gas, and re-digested using 2 ml of 3 M HNO_3 + 0.28 M HF prior to aliquoting for concentration measurement.

After digestion, a small aliquot (~5% of solution) was taken for Zr concentration determinations on an Agilent 7900 inductively coupled plasma mass spectrometer (ICP-MS) at University of Rochester (e.g., Ibañez-Mejia and Tissot, 2019). Once Zr concentrations in the sample solutions

were known, samples were spiked with our in-house ^{91}Zr-^{96}Zr isotopic tracer in optimal proportions (i.e., 0.45:0.55 spike-to-sample Zr mass ratio; see Tompkins et al., 2020).

Zirconium purification for all bulk-rock samples and mineral separates followed a four-step ion-exchange procedure where Zr and Hf are first separated from major elements using Eichrom DGA resin. A "matrix clean-up" step was then performed using AG1-X8 resin to ensure complete removal of Fe and other major elements. Subsequently, Zr was separated from Hf using Eichrom Ln-spec resin, and from Mo and Ru, which produce isobaric interferences on several Zr isotopes, using a final clean-up step with AG1-X8 resin. More details on the ion-exchange purification procedure are provided in Ibañez-Mejia and Tissot (2019) and Tompkins et al. (2020).

Zr isotope measurements were performed on the Thermo-Scientific Neptune*Plus* MC-ICP-MS at the Isotoparium (Caltech) using the same setup and methods as Tompkins et al. (2020) and Klaver et al. (2021). In brief, measurements were made in static mode with faraday detectors monitoring masses 90 to 98. All cups used 10^{11} Ω feedback resistors except for H1 (^{95}Mo) and H4 (^{98}Mo), which used 10^{12} Ω feedback resistors to improve measurement accuracy for Mo isobaric interference monitoring and corrections. Cup gain calibrations and electronic baselines (60 s, deflecting the ion beam using the Electrostatic Analyser) were performed daily.

Sample solutions containing 70-108 ng/mL Zr in 0.59 M HNO_3 + 0.28 M HF matrix were introduced with an Aridus 3 desolvating nebuliser using a nominal 100 µL/min PFA nebuliser (actual flow rate of 118 µL/min), which yielded a total Zr ion beam intensity (sample + double spike) of 26-40 V (or about 375 V/ppm of Zr). Each sample was measured two to five times during the session in a non-consecutive fashion. Each unknown measurement was bracketed (linear interpolation) by measurements of a NIST Zr iRM. Bracketing standards were spiked at the same level as the samples. On-peak-zeros (OPZ) were measured using a 55 s uptake and 20 s on-peak

measurement of clean acid solution from the same batch used to dilute the samples, allowing monitoring of memory effects of the sample introduction system. Sample and bracketing standard measurements consisted of 55 s of sample uptake, followed by 50 cycles of 4.192 s integration time each, for a total of ca. 210–250 s of static on-peak sample measurement, consuming ~550 μL of solution. The sample introduction system was rinsed for 360 s between samples using 0.59 M HNO_3 + 0.28 M HF, before repeating the cycle for the next standard/unknown.

Data were processed offline employing a minimization approach using all five measured Zr isotopes to solve the double spike equations (see Tompkins et al., 2020). Unlike the conventional DS reduction which only uses 4 isotopes, this approach allows us to check that all ratios are mass-dependently related to one another after DS data reduction. Data are reported as $\delta^{9x/90}Zr_{NIST}$ (hereafter abbreviated to $\delta^{9x/90}Zr$), where x can be 1, 2, 4 or 6 depending on the Zr isotope considered in the numerator, relative to a novel Zr reference material (provisionally named RM8299 Zr iRM, interlaboratory calibration ongoing, see Tompkins et al., 2020, for details), and referred to hereafter as Zr NIST. For simplicity, only the $\delta^{94/90}Zr$ values are shown in figures, but for completeness and to demonstrate the mass dependency of our measurements the $\delta^{91/90}Zr$, $\delta^{92/90}Zr$ and $\delta^{96/90}Zr$ values obtained after DS inversion are also included in Table S2. Sample-standard bracketing was performed by linear interpolation using the bracketing standards measured immediately before and after the unknown solution.

For each day of analyses, the dispersion of the standard-bracketed-standard (2SD) for each isotope ratio was calculated using linear interpolation. Uncertainties for individual sample measurements are reported as the 2 SE daily external reproducibility of the standard, rather than the internal precision (*i.e.*, from counting statistics) of each measurement.

3.4.6 Modeling the impact of co-crystallizing phases on zircon isotopic composition

To assess the effect of multiple Zr-bearing phases on Zr isotopic evolution of zircon, we undertook a series of calculations to assess the potential impact of titanite on the Zr isotopic composition of La Posta zircons. In our illustrative examples, we assume: 1) titanite and zircon temporally co-crystallize; 2) Zr is drawn from within a spherical reservoir assuming its diffusivity is high with respect to growth rate of zircon and titanite; 3) the radius of the reservoir sphere is equal to the final mass of zircon and titanite (i.e., $M_{Zr\text{-}zircon} + M_{Zr\text{-}titanite} = 2 \times (4/3\ \pi\ r^3\ [Zr]_{melt})$); and 4) the growth of titanite and zircon occurs in steps with a constant lowering of temperature (over 100°C such that 1°C reflects a 0.01 change in f) resulting in the partitioning of two isotopes between three reservoirs as the melt reservoir decreases in size and material is constantly removed with instantaneous solid-melt fractionation represented by α.

3.5. Results

3.5.1 In situ standards

Multiple traditional geochemical standards (including AS3, FC-1, Mud Tank, Fishtank, Temora, 91500) were first measured with several being found to exhibit $\delta^{94/90}$Zr homogeneity and were within uncertainty of measurements performed using double-spike (DS) MC-ICPMS (Table S3). Two exceptions to this case are AS3 and FC-1 (both from the Duluth anorthosite in Minnesota) which both showed large, multi-‰ variations as previously reported (Ibañez-Mejia and Tissot, 2019; Zhang et al, 2019).

3.5.2 Zr isotopic compositions

Seven La Posta granitoid whole rock Zr isotope analyses range in $\delta^{94/90}$Zr from -0.050 ± 0.012 ‰ (LP2) to +0.013 ± 0.013 ‰ (LP1-1) (Fig. 4; Table S2). Sample CG1 from the cumulate Cuyamaca gabbro, which is largely exposed to the west of the I-S line, yields $\delta^{94/90}$Zr of -0.101 ± 0.017 ‰

(Table S2). No clear relationship between whole rock SiO_2 (Table S1) and either average zircon (Table S1) or whole rock (Table S2) $\delta^{94/90}Zr$ is observed (Fig. 4).

Compositions on mount PR3 were calculated by taking into consideration instrumental drift. All other analyses were calculated by averaging our in-situ standard (Table S3; Table S4). As noted earlier, a change in analysis protocol conditions was implemented for the September 2019 session yielding an improved background correction. All La Posta zircon isotopic measurements are from that September 2019 session (Table S4), but we report standards from all three sessions to demonstrate reproducibility (Table S3).

We report 153 measurements of Zr isotopes in zircons measured by SIMS from the La Posta suite (Table S4). Apart from LP3, all rocks have mean $\delta^{94/90}Zr_{zircon}$ between ~-0.2 and ~-0.3 ‰ (Fig. 4), and the difference in maximum and minimum $\delta^{94/90}Zr_{zircon}$ for each rock are between 1.0 and 1.9‰ (Fig. 3.5). While both LP3 and LP7 are from the hornblende-biotite unit and have approximately the same minimum value, LP7 has a smaller range of values than LP3 (LP3: 1.54 ‰; LP7: 1.10 ‰). In addition, the two samples from the small-biotite unit, LP2 and LP5, have ranges of 1.51‰ and 1.01‰, respectively. While we see essentially no correlation between mean (R^2 = 0.17) and maximum (R^2 = 0.05) values for each rock and the associated whole rock SiO_2, we observe a stronger correlation between minimum $\delta^{94/90}Zr_{zircon}$ and whole rock SiO_2 (R^2 = 0.73) (Fig. 3.5).

Results from MC-ICPMS measurements show the $\delta^{94/90}Zr$ of biotite is indistinguishable from the whole rock average (average $\Delta_{bio\text{-}wr}$= -0.004 ‰) while titanite and amphibole preferentially incorporate heavier isotopes into their structures (Table S2; Fig. 4). Samples LP1, LP3, and LP7 have average $\Delta_{hbl\text{-}wr}$ of 0.313, 0.302, and 0.250 ‰, respectively (Table S2; Fig. 4). All three values are remarkably similar. The partitioning of Zr isotopes between titanite and whole rock is even greater, with average $\Delta_{tit\text{-}wr}$ of 0.592 and 0.563 ‰, observed in LP2 and LP7, respectively (Table

S2; Fig. 4). Concentrations of Zr in amphibole are relatively low (36-59 ppm from three samples; Table S2) thus fractionation of this phase is less likely to strongly influence zircon Zr isotopic compositions given the typical size and modal abundance of amphibole observed in our samples. In contrast, titanite contains higher Zr concentrations (LP2, 656 ppm; LP7, 320 ppm) and is sufficiently abundant in La Posta granitoids (up to 10% locally; see LP13 outcrop image in Fig. 3.6) to potentially influence zircon $^{94}Zr/^{90}Zr$ ratios during fractional crystallization (Table S2; Fig. 4). Of course, unseen amphibole and titanite cumulates could have influenced the Zr isotopic budget in a fashion for which we have no controls.

Isotopic profiles of La Posta grains do not all show similar patterns (Fig. 3.7). For example, LP2 grain 1, LP3 grain 12, and LP7 grain 7 have profiles which show no isotopic change among the different growth zones. Other grains, including LP3 grain 6, LP3 grain 9, and LP5 grain 5 have slightly heavier isotopic compositions on the outer portion of their respective grains. LP6 grain 8, which appears to have a metamorphic texture, has values mostly between -0.5 ‰ and 0.5 ‰ yet there is not a distinguishable relationship between location and isotopic composition, even when considering analyses taken on either metamorphic or igneous textured locations. However, if we only look at the region of the core which contains oscillatory zoning, all spots are within uncertainty of one another. LP6 grain 7 has three spots in the core and mantle with almost uniform isotopic compositions yet the core spot has a lower Ti-in-zircon temperature. The outer-mantle of this grain has a spot which is ~1 ‰ higher than the core. LP6 grain 2 has a slightly heavier inner mantle than core and a lighter outer mantle than inner mantle. Information on grain numbers can be found in Table S5.

3.5.3 Zircon trace elements in the La Posta Pluton

Following screening for alteration, 182 trace element measurements of La Posta zircons remained in consideration (Table S6) with 132 of them matching a U-Pb dating spot (Table S5; Table S7). We observe large variations of $\delta^{94/90}$Zr among zircons within a single rock but little correlation with paired trace elements (the highest R^2 values are between $\delta^{94/90}$Zr and Th/U (R^2=0.05), Eu_N (R^2 = 0.05), and Sm (R^2 = 0.05)). Hf, generally a strong indicator of magmatic differentiation, shows an even weaker correlation (R^2 = 0.01). Although we observe significant intra-zircon $\delta^{94/90}$Zr variations, these variations do not obviously correlate with CL zoning either (Fig. 3.8). At the intragrain level, the highest correlations are between $\delta^{94/90}$Zr and Th/U (R^2 = 0.16), Yb_N/Gd_N (R^2 = 0.10), and Mg (R^2 = 0.07). This low correlation coefficients show lack of correlation between Zr stable isotopes and trace element markers. The correlation between $\delta^{94/90}$Zr and Hf is even weaker (R^2=0.03). Using the modified Gd anomaly (Colombini et al., 2011), we observe MREE depletions in zircons from the less differentiated parts of the La Posta suite indicating the presence of one or more additional phase(s) sequestering MREE (Fig. 3.9).

3.5.4 Zircon U-Pb ages

Over five sessions (October 2020, November 2020A, November 2020B, November 2020C December 2020), we performed 218 U-Pb analyses on La Posta zircons with 145 analyses having % radiogenic ^{206}Pb greater than 95%, and 69 analyses of those analyses being within 30% of concordance (Table S7). Of those 145 spots, 89 spots were matched with a $\delta^{94/90}$Zr analysis. Of the 69 spots within 30% of concordia, 47 are associated with a $\delta^{94/90}$Zr analysis spot (Fig. 3.10). In total, 81 spots have trace element and $\delta^{94/90}$Zr spots collocated with the U-Pb age with 47 of those analyses being within 30% of concordance (Table S5).

Most U-Pb ages are Late (n=3, 11 without Zr isotopes) or Early Cretaceous (n=12, 6 without Zr isotopes) (Table S4, Table S5, Table S7; Fig. 3.10). However, three ages are Late Jurassic (n=2

without Zr isotopes) and one each are early Jurassic, Late Devonian, Early Devonian, and Proterozoic (Table S4, Table S5, Table S7). Among the paired (U-Pb + $^{94/90}$Zr) analyses, U-Pb ages range between 74 Ma and 148 Ma with the exception of the single Proterozoic age from LP2@3 (LP2 grain 1) where the Zr analysis spot may be impacted by an inherited core as indicated by textural evidence (Fig. 3.8).

While it appears that the Zr isotopic composition of zircon may be becoming lighter with age, the data are highly variable (Fig. 3.10). The Late Jurassic (PR3_LP3@4: 0.24±0.11 ‰ (1σ) and oldest Early Cretaceous (PR3_LP3@11: 0.41±0.13‰ (1σ)) analyses are comparatively heavier than the three analyses with ~120 Ma ages (~-0.4‰) (Table S7). However, there is a weak correlation between $\delta^{94/90}Zr_{zircon}$ and age for spots with U-Pb ages between ~74 Ma and 108 Ma. To understand whether there is a relationship between age and isotopic composition at the rock unit scale, we compare paired analyses from the hornblende-biotite unit (samples LP3 and LP7) as well as those from LP3 and LP7 individually. The two isotopically heavy LP3 spots discussed earlier result in a spuriously strong correlation between age and isotopic composition (R^2 = 0.48, n=7). LP7, however, shows no correlation between age and isotopic composition (R^2 = 0.06, n=19). Similarly, the small-biotite unit (LP2 and LP5) have no correlation when either analyzed together (R^2 = 0.03, n=10) or with LP2 alone (R^2 = <0.01, n = 8).

3.5.5 Petrography

Thin section examination of a variety of La Posta suite rocks show that zircon are characteristically found either in clumps (likely formed in late crystallization melt pockets) or as single grains uniformly distributed through the rock (Fig. 3.2). SEM petrographic observations of thick sections reveal isolated small to large euhedral to subhedral zircon grains included in a variety of host grains (Fig. 3.3). Crystal textures indicate that titanite forms over a broad range of the crystallization

sequence including early (Fig. 3.3C) and late (Fig. 3.3B) forming grains. Of note are the euhedral, early forming titanite grains in LP13 (Fig. 3.6).

3.6. Discussion

3.6.1 Zircon-melt fractionation factors

To model the variable intra-crystalline Zr isotopic composition during crystallization, we assumed Rayleigh distillation in a spherical melt reservoir of a radius containing the total Zr mass in the zircon, with the crystal forming at its center. In our model, isotopic fractionation and zircon growth occur in: (1) isothermal steps and (2) at a constant change in temperature, both in a closed system resulting in the partitioning of ^{94}Zr and ^{90}Zr between the solid and melt Zr reservoirs (Fig. 3.11A and E; Fig. 3.15A and E).

Due to the discrepancy in calculations of zircon-melt fractionation factors (Méheut et al., 2021; Chen et al., 2020; Guo et al., 2020), we calculate temperature-dependent fractionation factors using three general models: (1) ab initio calculations, (2) an ionic model, and (3) the regression reported in Guo et al. (2020) between 1000 $\ln\alpha_{zircon\text{-}melt}$ and $10^6/T^2$ (Fig. 3.12).

Two studies report force constants calculated using ab initio methods (Chen et al., 2020; Méheut et al., 2021). To model the melt, Chen et al. (2020) used Ca-catapleiite as a model structure for silicate melts. They calculated the ab initio force constant <F> of zircon and Ca-catapleiite as 334.7 N/m and 369.2 N/m, respectively. Méheut et al. (2021) used Vlasovite as their model structure for the melt due to both it and silicate melts having the same Zr coordination number (C.N. = 6) and similar Zr-O bond lengths. They determined the <F> of zircon and Vlasovite as 392.7 N/m and 407.8 N/m, respectively. Using these force constants, we calculate the β factor for both melt and zircon as:

$$1000 \ln \beta (^{94}Zr/^{90}Zr) \simeq 2081.6 <F>/T^2 \quad (3.2)$$

where <F> is the force constant, β is the reduced partition function ratio, and T is the temperature in Kelvin. We then calculate the zircon-melt fractionation factor for each set of force constants using

$$\ln \alpha_{\text{product-reactant}} = \ln \beta_{\text{product}} - \ln \beta_{\text{reactant}} \quad (3.3)$$

where the product is zircon and the reactant is melt (Figs. 3.11, Fig. 3.12, Fig. 3.15).

Second, we calculate isotope fractionation factors using an ionic model. Ionic force constants, K_f (Young et al., 2015) were determined using

$$K_f = \frac{z_i z_j e^2 (1-n)}{4\pi \epsilon^o r_o^3} \quad (3.4)$$

where z_x are the cation and anion valences, e is the charge of an electron, n is 12, ε^o is vacuum permittivity, and r_o is the equilibrium interionic distance. Interatomic distances were obtained from Robinson et al. (1971) and CrystalMaker® and force constants were calculated for each different interatomic distance in zircon. Since the Zr coordination polyhedron in zircon is a distorted octahedra, four bonds are 2.268 Å and four are 2.131 Å. The force constants for all bonds are averaged and used to calculate a fractionation factor. Since bond lengths are largely unknown in melts, we assume 2.10 Å for melt (Louvel et al., 2013). This results in K_f of 1914 N/m and 2186 N/m for zircon and melt, respectively. We then calculate the fractionation factor as:

$$ln\alpha_{A-B} = \frac{1}{24}\left(\frac{h}{k_b T}\right)^2 \left(\frac{1}{m_l} - \frac{1}{m_h}\right)\left[\frac{K_{f,A}}{4pi^2} - \frac{K_{f,B}}{4pi^2}\right] \quad (3.5)$$

where h is Planck's constant, k_b is the Boltzmann constant, T is temperature in Kelvin, m_l is the mass of the light isotope (^{90}Zr), m_h is the mass of the heavy isotope (^{94}Zr), K_f is the force constant, phase A is zircon, and phase B is the melt (Young et al., 2015) (Figs. 3.11, 3.12).

Third, we used the empirical temperature-dependent isotope fractionation relationship of Guo et al. (2020) (Table S6):

$$1000 \ln \alpha = -0.95x + 0.65 \quad (3.6)$$

where x is $10^6/T$(K) and T for that spot is determined from Ti-in-zircon thermometry (Watson and Harrison, 2005). We do this for illustration and comparison purposes despite questioning the validity of the Guo et al. (2020) calibration (which they acknowledge as provisional). Specifically, the slope of the regression appears too large (e.g., yields factor of 2 isotopic fractionation over <100°C intervals and ~11 ‰ at 30°C) to be physically feasible and the regression predicts non-zero fractionations at infinitely high temperature, which violates the principles of stable isotope fractionation. As shown in Figure 3.12, fractionation factors calculated by this method are approximately an order of magnitude higher than those proposed by ab initio calculations and several times higher than those calculated using ionic models. Méheut et al. (2021) posits that the isotopic variations observed by Guo et al. (2020) are controlled by kinetic rather than equilibrium effects making us question the use of Eq. (3.6) to understand equilibrium fractionation of zircon. Examples of Rayleigh fractionation curves due to continuous zircon removal from a melt, calculated using the above methods, are shown in Figures 12A and B, respectively. All zircon fractionation factors, $\alpha_{zircon\text{-}melt}$, are less than 1. Profiles calculated using $a_{Ti} = 1$ and $a_{Ti} = 0.7$ are very similar with the trajectory where $a_{Ti} = 1.0$ resulting in a slightly heavier initial $\delta^{94/90}Zr_{zircon}$ than the trajectory calculated using $a_{Ti} = 0.7$ (Fig. 3.16). Because of the similarity, all other profiles are calculated using $a_{Ti} = 0.7$.

3.6.2 Titanite-melt fractionation factors

Since we do not at present have a provisional temperature-dependent isotope fractionation calibration for titanite as we do for zircon (e.g., as determined theoretically by Chen et al. (2020) or Méheut et al. (2021) or hypothesized using inversions of natural zircon data by Guo et al. (2020)), we estimate the titanite-melt fractionation factors a variety of ways. First, using force

constants calculated using density functional theory in Chen et al. (2020) ($<F_{pyrope}>$ = 433.5 N/m and $<F_{melt}>$ = 369.2 N/m) and eq. 3.2 and 3.3, we calculate fractionation between melt and a titanite proxy. While ab initio calculations of Zr in titanite have not been calculated, force constants for Zr substitution into the octahedral site in pyrope were performed by Chen et al. (2020). Therefore, we use data from the $^{IV}Al^{3+} + {}^{1V}Si^{4+} \leftrightarrow Zr^{4+} + Al^{3+}$ substitution in pyrope as a proxy for Zr substitution in titanite. This substitution in pyrope was chosen as a proxy because both Ti in titanite and Zr in the octahedral site in pyrope have similar cation-oxygen lengths and both bonds are in the same coordination (Chen et al., 2020). Ca-Catapleiite, which we use to understand the structure of the melt when looking at zircon-melt fractionation, is again used as a proxy for melt (Fig. 3.12D). Second, we calculated the fractionation factors using an ionic model. Force constants are calculated using equations 4 and 5 where phase A is titanite and phase B is the melt. Zr in titanite is in an octahedrally coordinated site, and we used CrystalMaker® to determine the interatomic distances for each bond (Speer and Gibbs, 1976). Force constants for each bond were calculated using the ionic model, and then an average force constant was used to calculate a fractionation factor. As described previously, we use 2.1 Å for melt Zr-O distance (Louvel et al., 2013) (Fig. 3.12C and D). The titanite-melt fractionation factors, $\alpha_{titanite\text{-}melt}$, estimated are greater than 1.

An alternate method to assess temperature effects on Zr isotope fractionation into titanite would be to regress titanite-melt fractionation with temperature (as determined by the 1000 $\ln\alpha_{av.titanite\text{-}rock}$ where $\alpha_{av.titanite\text{-}rock}$ is the fractionation factor between the titanite and the whole rock). Temperatures for this calculation could be determined via average Zr-in-titanite crystallization temperatures for each rock (Hayden et al., 2008). This approach, similar to the method of Guo et al. (2020), is not appropriate where both zircon and titanite are significant reservoirs of Zr due the paucity of documented titanite-rock fractionation factors. This is further complicated by the

closeness of these two samples' average Ti-in-zircon and Zr-in-titanite temperatures. This results in a regression with very large error bars that trend positive rather than negative as expected from first principles.

3.6.3 Modeling melt evolution

We use the Raleigh distillation model to calculate isotopic composition at each point *f*,

$$\delta = ((\delta_o + 1000) \times f^{\alpha-1}) - 1000, \quad (3.7)$$

where δ is the calculated $^{94}Zr/^{90}Zr$ isotopic ratio, δ_o is the starting melt $^{94}Zr/^{90}Zr$ composition, α is the temperature-dependent fractionation factor, and *f* is the fraction of Zr remaining in the melt sphere. To account for changing temperature, a revised fractionation factor is then calculated for each new temperature (Figs. 3.11, 3.12, 3.15). In the case where zircon is the only Zr-bearing phase under consideration, we assume that all Zr initially in the melt will be incorporated into the growing zircon. Thus, we plot the Zr isotopic evolution both spatially (radius-to-volume effects are discussed below) and as the fraction of Zr remaining (Figs. 11A, B, E, and F; Figs. 3.15A, B, E, and F).

The above model assumes that Zr is rapidly equilibrated within the spherical melt reservoir such that its isotopic composition at the crystal growth surface is continuously refreshed to the average value of the remaining reservoir. This assumption is likely valid in hydrous magmas at temperatures typical of zircon formation in intermediate to felsic systems (Harrison and Watson, 1983; Mungall et al., 1999). We can get a first order estimate of the timescale for homogenization using the 1-D approximation $t = r^2/D$, where *t* is time and *D* is the Zr diffusivity.

As noted above, the length scale of the melt sphere is determined by the mass of Zr required to form a tabular zircon (i.e., $M_{zir} = 2 \times (4/3\ \pi\ r^3\ [Zr]_{melt})$, where M_{zir} is the mass of Zr in the zircon, 2 is the $ZrSiO_4$/Zr weight correction factor, *r* is the radius of the melt reservoir, and $[Zr]_{melt}$ is the

concentration of Zr in the melt. For a grain with an effective spherical radius *a* of 90 μm (i.e., the spherical mass equivalent of a tabular zircon), the radius of the required melt reservoir is ~1100 μm. Note that this calculation does not address the complication arising from the crystallization of large modal phases within the reservoir volume but the additional diffusional tortuosity this produces could be partially compensated for by the resulting advection of Zr toward the growing zircon due to the aforementioned 'pileup' effect (Méheut et al., 2021).

3.6.4 Difference between fractionation factors

As shown in Figures 11 and S1, the three approaches yield contrasting fractionation factors. For example, calculating fractionation factors using the force constants from the two different ab initio studies produce a ~0.3‰ difference in the composition of the final zircons (Chen et al., 2020; Méheut et al., 2021). These differences are caused by a combination of different model inputs including differences in the characteristics of the mineral each chose to model the melt. The ionic model results in fractionations several times larger than what is observed in ab initio studies.

As discussed in Méheut et al. (2021), the isotope profiles in zircon grains reported in the Guo et al. (2020) study may be dominated by kinetic fractionation making this a poor choice for determining equilibrium fractionation factors. Beyond this, the temperature dependence (Eq. 6) is statistically weak with large scatter. This, and the unreasonably large effects this relationship predicts at both low and infinite temperature, leads us to argue against its use in determining temperature-dependent fractionation factors.

To proceed, we used the Chen et al. (2020) ab initio values and the ionic model as the most promising approaches; the Chen et al. (2020) study provides force constants for zircon, melt, and a titanite proxy while the ionic model allows us to directly compare titanite and zircon fractionation. Calculations using the ionic model are normally within a factor of 2 or 3 of ab initio

calculations (Young et al. 2015). Another advantage is that we can directly calculate the titanite fractionation factor by performing these calculations using the ionic model rather than relying on assumptions based on similarity of bonding environments –and force constants– in compositionally different minerals.

However, we note that this method is hindered by the lack of known interatomic distances in melt. While we do not have exact values of this parameter, interatomic distances of zircon and titanite are determined to be larger and smaller, respectively, compared to melt in other studies (Robinson et al., 1971; Farges et al., 1991; Louvel et al., 2013; Chen et al., 2020). Therefore, while the force constants will be slightly different depending on what Zr-O bond lengths are used for melt, titanite has $\alpha_{titanite\text{-}melt} > 1$ and zircon has an $\alpha_{titanite\text{-}melt} < 1$ allowing for a basic understanding of fractionation (Fig. 4). Beyond the modeled relationships, titanite isotopic compositions from our two samples are both: (1) isotopically heavier than their respective bulk rock values by very similar magnitudes; and (2) isotopically heavier than most of the zircons in their respective rocks thus providing further evidence for direction of relative fractionation between the two phases.

3.6.5 Spatial effects

To model the spatial evolution of Zr isotopes within zircon, we need to relate *f* in some way to size. Given the generally square prismatic shape of igneous zircon, we use a model with parallel sides and variable length as a first order approximation of the mass-to-length relationship. We model two shapes: x = y = z (i.e., a cube; Fig. 3.11B and F; Fig. 3.15B, F) for reference and x = y = 0.2z to approximate a square prismatic zircon (Figs. 3.11C, F; Fig. 3.17b; Figs. 3.15C, F). For the cubic case, $d = (V_{zircon} \times (1\text{-}f))^{1/3}$ where d is diameter and V_{zircon} is the volume of the zircon. For the second case, $d_{y,z} = (V_{zircon}/2 \times (1\text{-}f))^{1/3}$ and $d_z = 5d_{y,z}$. Graphical representations of the grain profiles calculated using the Chen et al. (2020) ab initio values and ionic model are shown in

Figures 11B and C and 11F and G, respectively. Profiles calculated using the two other methods are shown in Figure S1.

Resolving growth-related isotopic variations in linear traverses within a 3D solid is problematic both because most of the mass is located close to the edges (~50% of the mass is between x, y = 0.8 and 1.0 in a cube) and closed system Raleigh equilibrium fractionation yields strongly fractionated effects only in the late stages of distillation (when looking at isotopic profiles formed because of equilibrium fractionation from our aforementioned melt packet). Of note from the model of our idealized grain is spot size vs. the change in isotopic composition. Zircon modeled as a square prismatic solid where x = y = z show that all three axes of a grain will plot with the same isotopic trajectory (Fig. 3.11B). Where $d_{relative,x,y}=0.2d_{relative,z}$, the x and y axis will have the same isotopic trajectory whereas the z axis will be five times as long (Fig. 3.11C; Fig. 3.17b). An idealized version of a grain where x = y = 40 µm and z = 200 µm, typical of La Posta zircons, with spot widths (SIMS (8 µm; green); LA-ICPMS (20 µm; Guo et al., 2020; blue)) is shown as Fig. 3.11D.

For systems where isotopic changes are a result of equilibrium fractionation, apparent isotopic composition stays approximately the same between $0 < r < 0.8$. It is not until the outer 20% of the grain diameter is reached that a large change in isotopic composition occurs. This emphasizes the importance of having the highest possible lateral resolution. For example, the model LA-ICPMS spot (20 µm) drawn on Fig. 3.11D and H show a change of ~0.13 ‰ (Chen et al. (2020) values) and ~0.34 ‰ (ionic model), respectively, from the innermost edge of the spot to the outermost edge of the spot when looking parallel to the z-axis. This value will increase with more oblique observations relative to the z-axis due to a smaller distance associated with the same change in

isotopic composition. This effect, while less problematic on SIMS due the smaller beam spot size, will still smear the isotopic profile.

While the recent analytical improvements on spot size for in situ methods have allowed far better spatial precision, analyses on the edges of grains are still going to mix multiple isotopic domains. This is especially problematic when looking at grain transects which exhibit Rayleigh fraction. For example, on a grain like the one modeled in Fig. 3.11D, one might be able to get one spot on each end of a grain when using a 20 μm beam and perhaps two spots on each end when using an 8 μm beam. However, this relative dearth of spatial information limits observations, including determination of the changing fractionation factor. This is both because of the multiple isotopic domains from which a beam is drawing at the edges of the grain and the lack of space available for analyses in the outermost portion of the grain. However, in diffusion-driven systems observed changes in isotopic composition may be larger. This allows better discrimination of different isotopic domains. Still, due to the spot size used to analyze these samples, the isotopic profiles will still be smeared and, due to most mass being in the outer portion of the grain, most fractionation, regardless of whether it is equilibrium or kinetic fractionation, will still be most pronounced in the outer portion of grain transects.

Among our natural samples from the La Posta samples, we see a variety of grain profile shapes. Considering that we expect to have relatively uniform isotopic composition until the outermost portion of grains if we assume equilibrium fractionation, the La Posta grains with nearly uniform isotopes or those with slight increases in isotopic composition towards to edge of the grain can be explained by equilibrium fractionation at either constant or variable T. However, some grains, such as LP6 grain 7, have unexpected isotopic profiles (Fig. 3.7). In this grain, the isotopically

heaviest point on this grain is not, as expected, close to the rim of the grain. This shows that something else is controlling Zr isotope fractionation in this system.

3.6.6 Potential impacts of kinetic mass dependent effects

To understand the causes of variable Zr isotopic fractionation in different systems (Tompkins et al., 2020, Inglis et al., 2019, Ibañez-Mejia and Tissot, 2019), we begin by examining whether these effects are caused by equilibrium fractionation. Méheut et al. (2021) argued that large fractionations can be caused by kinetic imbalances between crystal growth, chemical diffusion in the melt, and the mass dependency of diffusing isotopes. While the import of their proposed mechanism is blunted by the lack of knowledge of the calibration parameter, β, which describes the magnitude of mass dependent diffusive separation between two isotopes (e.g., ^{94}Zr and ^{90}Zr) and the assumption of anhydrous crystallization conditions, it appears viable in the case of rapidly crystalizing volcanic and hypabyssal magmas. However, its application to the plutonic rocks under study is problematic. Specifically, that all slow diffusing, incompatible, high field strength elements (e.g., Zr and P) 'pileup' in the zone adjacent a rapidly growing modal phase creating large concentration gradients along which significant isotopic fractionation could occur.

Méheut et al. (2021) argues that the profiles shown in Guo et al. (2020), which are from zircons formed in the hydrous Gangdese Batholith, indicate kinetic rather than equilibrium fraction due in part to the high zircon growth rate to Zr diffusion in melt ratio (R/D). While this is true for anhydrous melts (e.g., ~2 x 10^4 cm^{-1} for a growth rate of 10^{-13} cm sec^{-1} at 740°C; Harrison and Watson, 1983), wet melts have a R/D less than 1 (e.g., 5 x 10^{-2} for a growth rate 10^{-13} cm sec^{-1} at 740°C; Harrison and Watson, 1983) meaning that zircon growth is slower than Zr diffusion in the latter case. While we cannot rule out a kinetic effect in hydrous magmas, this does not appear a plausible mechanism to explain our results.

Méheut et al. (2021) discuss how diffusive boundary layers form and their impact on grain fractionation. The speed of crystal growth, diffusion in the melt, and the isotopic mass dependency of diffusion all contribute to whether kinetic fractionation occurs. For example, a compound which has a low partition coefficient between melt and solid in a grain with a fast growth rate will result in the area near the surface of a grain being enriched in that compound. However, the amount of this local enrichment is equal to the diffusivity of that same compound in the melt. If they diffusivity in the melt is faster than the growth rate of the crystal, an enriched diffusive boundary layer should not exist. Sketches of the formation of these diffusive boundary layers are shown in Figure 3.18c.

3.6.7 Zr isotopic fractionation between zircon and melt

As noted in the Introduction, rocks of the La Posta series fractionated under hydrous conditions yielding relatively uniform distributions of zircon. Thus, we chose to investigate the coupled effects of temperature and simultaneous growth of multiple Zr-bearing phases as a possible source of observed 1 to 1.9‰ $\delta^{94/90}$Zr variations in La Posta zircon. Predicting the isotopic composition of Zr in zircons forming from a silicate magma is complicated by our lack of knowledge of the crystallization and fractionation histories of those zircons, the presence of co-crystalizing Zr-bearing phases (e.g., titanite), and the thermal history of the magma. However, we have several tools that can aid in attempting such reconstructions. We can use Ti and Zr thermobarometry to gain insights into the possible co-crystallization of zircon (Watson and Harrison, 2005) and titanite (Hayden et al., 2008), and can utilize the known diffusion parameters for Zr in hydrous silicate melts (Watson and Harrison, 1983; Mungall et al., 1999) to assess the likelihood of isotopic equilibrium being maintained during some specified thermal evolution. Thus, rather than viewing the problem as simply an exchange between bulk melt and zircon (and its attendant mathematical

simplifications), we chose a model that places individual zircons in context with the melt volume required to fertilize the growing zircon described earlier.

Our calculation described in "*Modeling fractionation between zircon and melt"* suggests that the time it would take for the model grain to form is only about 500 years. However, this assumes that all Zr is removed from the reservoir sphere whereas in reality only that portion above the level of zircon saturation in the melt can be sequestered at any particular moment in time. This requires a more complex calculation that involves decreasing zircon solubility with cooling (Watson and Harrison, 1983; Boehnke et al., 2013). Watson (1996) undertook such an analysis, principally for the case of zircon dissolution but as both processes are controlled by the absolute melt solubility, level of over/undersaturation, and Zr diffusivity (rather than being interface controlled), these results provide complimentary insights into crystallization timescales as well. For plausible values for the La Posta case (i.e., Zr oversaturation of 20 ppm, cooling rate of 0.01°C/yr; see Fig. 8 of Watson, 1996), a 90 μm radius zircon is estimated to form in ~10,000 years. This timescale is both commensurate with known U-Th ages of young magmatic zircons (Reid et al., 1997; Schmitt, 2011) and sufficiently long (as illustrated by the heuristic calculation above) for Zr isotopic homogeneity in a hydrous magma to be continuously achieved by diffusion within the reservoir shell. While this model presupposes no ingress of Zr into the reservoir sphere during zircon crystallization, a seemingly unrealistic assumption at first glance, a stochastic distribution of zircon nuclei spaced roughly at the characteristic Zr diffusion distance ($x = \sqrt{\kappa \times t}$ where x is distance, κ is diffusivity, and *t* is time) and would have the effect of approximating a zero Zr flux boundary condition at the shell perimeter (Bindeman and Melnik, 2016). Sample petrography is broadly consistent with this assumption with clumps of zircon formed in melt pockets often appearing together in thin section (Fig. 3.2).

Deviations of our modelled isotopic trajectories from measured values, as observed in this study, would imply that at least one underlying assumption is incorrect. For example, increases in Ti-in-zircon temperatures likely mean that magma recharge had occurred, which are recorded in the higher crystallization temperatures of our more differentiated samples. While this newly introduced magma could potentially change the Zr isotopic composition of the reference melt sphere, the fact that thermal diffusion is ten orders of magnitude faster than Zr diffusion in a melt held at 700°C suggests otherwise. Another potential cause of misalignment of theory and measured values is if another phase is also incorporating Zr (and fractionating Zr isotopes) into its structure.

3.6.8 Impact of temperature

As expected from first principles, temperature should impact Zr isotopic fractionation with a greater magnitude at lower temperature (generally following $1/T^2$). While many of the grains in this study have only a few tens of degrees of recorded temperature change, some grains, such as LP6 grain 7, exhibit a much larger (87°C) change from core to mantle. For such grains, including temperature effects in calculations of fractionation factors is important as can be seen in our models showing changing vs. constant T, especially at low f (Fig. 3.16).

Guo et al., (2020) observed a relationship between calculated fractionation factor (inverted from Rayleigh fractionation modeling) and average Ti-in-zircon temperature for each rock in their study by performing a linear regression between 1000 $\ln(\alpha)$ and $10^6/T^2$. However, the large range of temperatures they found within each rock preclude a precise calibration, and as noted earlier, the model they derived is generally physically implausible. Furthermore, Ti concentration measurements were not performed on many of the grains in the Guo et al., (2020) study and uniform target selection criteria were used on those analyzed (e.g., their Fig. 3.2E shows a Ti

analysis spot in the grain core which, in the absence of recharge, would represent the highest temperature experienced rather than the average).

3.6.9 Impact of co-crystallizing phases

As noted earlier, the average Zr isotopic values for these rocks are all within uncertainty at the bulk rock scale (Fig. 4). However, the more differentiated the rock (as indicated by whole rock SiO_2), the greater the variability in zircon isotope composition with isotopically lighter zircons becoming more prevalent in more differentiated rocks (Fig. 3.5). However, the lightest values do not correlate with temperature, indicating that there may be a local effect from an isotopically heavier co-crystallizing phase.

We observe the impact of co-crystallizing phases geochemically through assessment of trace elements in zircon (Fig. 3.9). HREE/MREE in zircon will decrease with garnet fractionation (Hauri et al., 1994) and increase with temperature due to lattice strain (Blundy and Wood, 1994; Blundy and Wood, 2003). MREE can also be depleted by the presence of other phases like titanite, hornblende, or garnet which either crystallized before or concurrently with zircon (Simmons and Hedge, 1978; Whitehouse and Platt, 2003; Harper et al., 2004; Davidson et al., 2007; Colombini et al., 2011). As stated earlier, the outer three units of the pluton contain significant hornblende and titanite (Walawender and Clinkenbeard 1989) indicating that titanite or amphibole may impact Zr isotopic compositions in La Posta pluton zircons. Due to both the much higher concentration of Zr and higher Zr isotopic fractionation exhibited by titanite compared to amphibole, we focus mostly on titanite.

Petrography indicates that titanite formation occurred throughout the crystallization process (Figs. 3.2, 3.3). This early formation would have allowed for the composition of the melt to become lighter by the fractionation of titanite. However, we also observe late forming titanite (Fig. 3.3),

and most, if not all, zircons appear to be euhedral (Fig. 3.3). While the late forming titanite likely formed after zircon and would not impact the isotopic composition of the zircon, the early formed titanite may have influenced the melt which zircons eventually formed from.

This effect from titanite may also have influenced zircon isotopic profiles from the Gangdese Batholith (Guo et al., 2020). These profiles are all concave with heavier zircon compositions towards the rims of the grains. This is expected if zircon fractionation is the primary control on Zr isotopic fractionation in the system. However, starting melt composition, which were determined by best fit for each grain, are different within rocks. This difference in initial melt composition could be caused by, as Méheut et al. (2021) proposed, slow diffusion of Zr resulting in a non-uniform distribution of initial Zr isotopic composition throughout the magma. However, the Gangdese batholith, similar to the Peninsular Ranges batholith, is characterized by hydrous magmas (Xu et al., 2015; Ding et al., 2021; Wang et al., 2021; Xia et al., 2021). As discussed earlier, such magmas yield higher Zr diffusivities that counteract the pileup effect making slow diffusion an unlikely culprit. Another potential impact for these differences in initial melt compositions is that another phase, like fractionation of amphibole or titanite, are pulling the starting melt composition to isotopically lighter compositions. The zircon isotopic profiles may be further impacted by titanite or amphibole fractionation during zircon crystallization which could change the apparent zircon fractionation factor. This would explain why the range of fractionation factors within each rock is so large. If some zircons are located near a titanite while other zircons are not, the fractionation factors of these two zircons will be different and the relationship between temperature and zircon fractionation factor will become harder to constrain.

3.6.10 Modeling the impact of Zr in co-crystallizing phases and impact of crystallization order

In order to understand the effect of co-crystallizing phases on the Zr isotopic evolution of a magma, we model three compositions: P_{zircon}= 50% and $P_{titanite}$= 50%, : P_{zircon}= 75% and $P_{titanite}$= 25% and : P_{zircon}= 90% and $P_{titanite}$= 10%, where P_x is equal to the proportion of Zr that goes into each phase (Fig. 3.13). We calculate the effective fractionation factor for the melt as $\alpha_{solids\text{-}melt} = (P_{titanite} \times \alpha_{titanite\text{-}melt,\,T}) + (P_{zircon} \times \alpha_{zircon\text{-}melt,\,T})$ where $\alpha_{solids\text{-}melt}$ is the fractionation factor between solids and melt, P_{phase} is the proportion of Zr portioning into either zircon or titanite, and $\alpha_{phase\text{-}melt,\,T}$ is the temperature dependent fractionation factor between either zircon or titanite and melt. To determine the isotopic composition of instantaneous zircon and titanite at each f, we use the equations

$$\delta_{melt} = \left(\delta_{melt,0} + 1000\right) \times f^{\alpha_{solid-melt}-1} - 1000, \text{ and} \quad (3.8)$$

$$\delta_{phase} = \delta_{melt} + \left(P_{phase} \times \varepsilon\right), \quad (3.9)$$

where $\varepsilon = 1000 \ln\alpha_{phase\text{-}melt}$ to the melt composition at that f.

Since $\alpha_{zircon\text{-}melt} < 1$ and $\alpha_{titanite\text{-}melt} > 1$, the concavity of the $\delta^{94/90}$Zr vs. f or diameter/2 changes from concave to convex depending on the amount of each phase being formed at that specific f (Fig. 3.13). We can model the relative fractions of each phase required to realize equal Zr consumption. Taking the highest [Zr] value we observe in titanite (i.e., 656 ppm in LP2) and the typical concentration of Zr in zircon (~480000 ppm), this translates to a titanite:zircon ratio of ~730. Thus, for the case in which titanite constitute 5% of modal phases, we would expect a zircon abundance of ~70 ppm. This value can then be used to determine how much titanite would need to be removed to have a specified effect in the zircon.

To understand the impact of crystallization order on Zr isotopic evolution, we modeled a series of isotopic evolutions (Fig. 3.14). Both systems contain 50% of Zr held in zircon and 50% in titanite. However, the first system has titanite alone crystallizing for the first 25°C (f = 1 to f = 0.75)

followed by 1/3 and 2/3 of the remaining Zr incorporated into titanite and zircon, respectively. In the second scenario, only titanite crystallizes until f=0.50 followed by only zircon until f=0.

As shown in Fig. 3.14, co-crystallizing phases with near opposite fractionation factors dampen the fractionation experienced by the melt as well as crystallizing phases. This will result in isotopic profiles from systems with co-crystallization having shallower isotopic trajectories than systems where phases crystallize subsequently. When each phase is fractionating without the other, we begin to see large fractionation.

To compare fractionation in a system which crystallizes zircon exclusively with that which crystallizes only titanite ($P_{titanite}$ = 50%) followed by all zircon (P_{zircon}=50%), we look at isotopic composition at f=0.5 and f=0.001 for both systems (Figs. 3.11, 3.14). We chose these values to represent the first occurrence of zircon in our latter system and the latest crystallizing grains in both systems. Unsurprisingly, the difference between the isotopic values at f = 0.5 and f = 0.001 are the same between the two systems due to the fractionation factor and temperatures being the same. However, the latter system results in lighter values than the exclusively zircon system.

3.6.11 Combined temperature and co-crystallization impacts on zircon profiles

As discussed earlier, grains with a larger change in T should exhibit greater fractionation if the assumptions described in the '*Modeling melt evolution' section* are correct. However, while it is relatively easy to perform Ti concentration measurements on the same spots as Zr analyses and attempt to determine a fractionation profile, the impacts of co- or earlier crystallizing phases are much harder to untangle. For example, co-crystallization of both titanite and zircon will result in a much shallower profile than if zircon crystallized alone (Fig. 3.13). Problematically, the aforementioned shallowed profile could equally be interpreted as a result of high temperature

crystallization if crystallization temperature or earlier impacts from other Zr-containing phases (titanite vs. amphibole. vs. cpx vs. some other phases) are unknown for each analyzed spot.

While a temperature impact could be quantified through a correlation of Ti-in-zircon measurements with associated Zr isotopic measurements if magma chemistry is known, the complications of earlier or co-crystallizing phases will still cause issues when attempting to understand what controls Zr isotope chemistry in different systems. Assessment of trace elements, such as Gd/Gd* or La/Lu can help with determination of co-existing phases but since multiple phases can cause similar depletions in trace elements, this approach may not provide a unique solution.

3.6.12 Relationship between zircon and titanite

Since we have two titanite Zr isotope measurements from two rocks, we can calculate fractionation factors between individual zircon composition and titanite. However, to do so, we must know at approximately what temperature titanite crystallized. To determine the potential impact of titanite on Zr isotope fractionation in the La Posta system, we estimated Zr-in-titanite temperatures for these samples (Hayden et al., 2008). We assume the same parameters as for Ti-in-zircon thermometry: a Ti activity (α_{Ti}) of 0.7 and a Si activity (α_{Si}) of 1, in addition to pressure estimates of 0.2 GPa to 0.5 GPa.

To understand the approximate pressures under which titanite formed, we used previously published Al-in-hornblende measurements (Hammarstrom and Zen, 1986; Clinkenbeard and Walawender, 1989). To calculate pressures, knowledge of oxygen fugacity is required, which is constrained through the presence of a specific mineral assemblage. In the case of the La Posta pluton, magnetite is absent from the phase assemblage, making us unable to use this thermobarometer (E.A. Bell, pers. comm.; Clinkenbeard and Walawender, 1989). Beyond that, it

is recommended that the thermobarometer not be used below ~2 kbar (Hollister et al., 1987), a requirement that is not met for some of the measurements of Clinkenbeard and Walawender (1989). However, the original study, Hammarstrom and Zen (1986), included rocks with varying f_{O2} along with much larger error bars than the later study (±0.3 GPa). For this reason, we calculate Zr-in-titanite for pressures between 0.2 GPa and 0.5 GPa (Table S2). If crystallization pressures are higher, true titanite crystallization temperatures will be higher than our calculations indicate. LP2 titanite crystallization temperatures are 732 °C and 769 °C for P = 0.2 GPa and 0.5, respectively. For sample LP7, temperatures are 694 and 729 °C for P = 0.2 GPa and 0.5 GPa, respectively. We calculate the fractionation factor between titanite and the zircon which crystallized at approximately the same temperature as the titanite for both LP2 and LP7. The fractionation factors were all > 0.6 ‰. Fractionation factors for a system where 50% of Zr partitions into titanite and zircon calculated using equations from Chen et al. (2020) and the ionic model have fractionation factors ~0.1 ‰ and ~-0.3 ‰, respectively.

While titanite fractionation cannot account for the entirety of the fractionation seen in the La Posta pluton, it can, and likely has, accounted for at least some of the fractionation. Figure 3.12 shows Rayleigh fractionation isotopic profiles if all Zr were incorporated into zircon or titanite. Because $\alpha_{zircon\text{-}melt}$ and $\alpha_{titanite\text{-}melt}$ are < 1 and > 1, respectively, zircons will get progressively heavier and titanite will become progressively lighter with greater fractionation. In our current model where δ_o is the whole rock composition, the models do not predict either the measured zircon or titanite isotopic values. For example, in a system where 50% of Zr is incorporated into zircon followed by the remaining 50% incorporated into titanite, we never reach the isotopically heavy titanite or the very isotopically light zircons observed in the LP7 La Posta sample. While the ionic model calculates much larger fractionation than models based on ab initio calculations, it still is not able

to reproduce the spread of isotopic compositions observed in the LP7 sample, regardless of crystallization order.

If we argue that isotopically heavy titanite was removed from the system, which could be the case due to the much higher amount of titanite observed in sample LP13 (Fig. 3.6) leading to an isotopically heavier starting melt composition, our model will still not predict the observed extremely isotopically light La Posta zircons.

3.6.13 Applications to understanding magmatic evolution

Inglis et al. (2018) found a tenuous correlation between whole rock SiO_2 and $\delta^{94/90}Zr$ among magmatic rock standards, while Inglis et al. (2019) saw a similar but clearer relationship in samples from Hekla Volcano. In the case of the Hekla study, Ibañez-Mejia and Tissot (2019) argue that trace element measurements and U-Th crystallization ages, some of which are tens of thousands of years older than the eruption age (Carley et al., 2011), indicate that rocks analyzed by Inglis et al. (2019) may be contaminated with material not formed during the targeted eruption. This contamination may have led to isotopically heavier results than the real isotopic composition of the rock.

We observe that the isotopic composition between the Cuyamaca gabbro sample (CG1, whole rock SiO_2: 41.52 %, whole rock $\delta^{94/90}Zr_{NIST}$: -0.101 ‰) and the least felsic sample (LP7, whole rock SiO_2: 68.63 %, whole rock $\delta^{94/90}Zr_{NIST}$: -0.042 ‰) becomes heavier suggesting a possible trend towards heavier isotopic composition with increased differentiation. However, isotopic compositions among the La Posta samples do not consistently change with greater differentiation. In addition, we note that the range of Zr isotopic values is larger for more differentiated samples. For example, LP6, which is our most differentiated sample, and which has a geochemical signature of sediment addition (Shaw et al., 2003; Bell and Kirkpatrick, 2021), has the largest range of

$\delta^{94/90}Zr_{NIST}$. However, the least differentiated sample, LP7, has the 2nd smallest range of values (Fig. 3.5). Potentially the reason for the large ranges in $\delta^{94/90}Zr_{NIST}$ in the intermediate units is because of the magma mingling or mixing seen previously (Shaw et al., 2014; Bell and Kirkpatrick, 2021).

3.6.14 Applications to detrital studies and future directions

While Guo et al. (2020) proposed Zr isotopes in zircon as a potential new tool for understanding out-of-context (i.e., detrital) zircons, the caveats discussed here make that goal difficult to achieve at the moment. Without clear knowledge of co-existing phases, crystallization temperature, and magma water content (insights into which might be obtained through examination of primary inclusions), it does not appear possible to determine the exact causes of observed fractionation. Assessment of inclusion phases could potentially allow for determination of pre- and co-crystallizing phases and perhaps elucidate how other phases may be impacting Zr isotope evolution. If necessary, even without a concrete knowledge of co-crystallizing phases, we could make inferences about magma chemistry from trace elements in out-of-context zircons. However, as stated earlier, trace elements have multiple controls including temperature, co-crystallizing phases, and pressure, and will not lead to an unambiguous reconstruction of the exact formation conditions of zircon or the nature of co-crystallizing phases. To understand specifically the impact of co-crystallizing phases on the Zr isotopic composition of zircons, studies of natural sites (preferably volcanic due to many phases instantaneously crystallizing) or experimental studies could be performed, allowing for a more precise assessment. Since the two studies that have examined plutonic felsic systems in-depth, this study and that of Guo et al. (2020), are both from areas which formed under hydrous conditions, a potential further path to explore would be to examine in-situ samples from an anhydrous natural system or samples where R/D > 1 is known.

This would allow for an in-depth examination of arguments in Méheut et al. (2021) about Zr fractionation being partially controlled by the development of Zr diffusive boundary layers.

3.7. Summary

In order to gain a greater understanding of Zr isotope behavior in magmatic systems, we performed a suite of analyses including Zr isotope measurements of zircon, titanite, amphibole, biotite, and whole rocks from the La Posta pluton, a zoned batholith in the Peninsular Ranges of southern California and undertook simple calculations to assess the role of temperature and co-crystallization effects on producing significant Zr isotopic variations. We found that non-zircon phases, in particular titanite, can significantly impact the Zr isotopic evolution of a system. Yet, these effects, even when incorporating impacts from changing temperature in a system, do not account for the up to 6‰ variations in zircons seen in the Duluth gabbro or the up to 1.9 ‰ variations seen in our La Posta samples. More studies which examine potential controls on Zr isotope evolution will allow for a greater understanding of this system. Until the responsible processes are better understood, it appears premature to see Zr stable isotopic investigations of igneous rocks as unambiguous proxies for magmatic evolution.

3.8 Figures

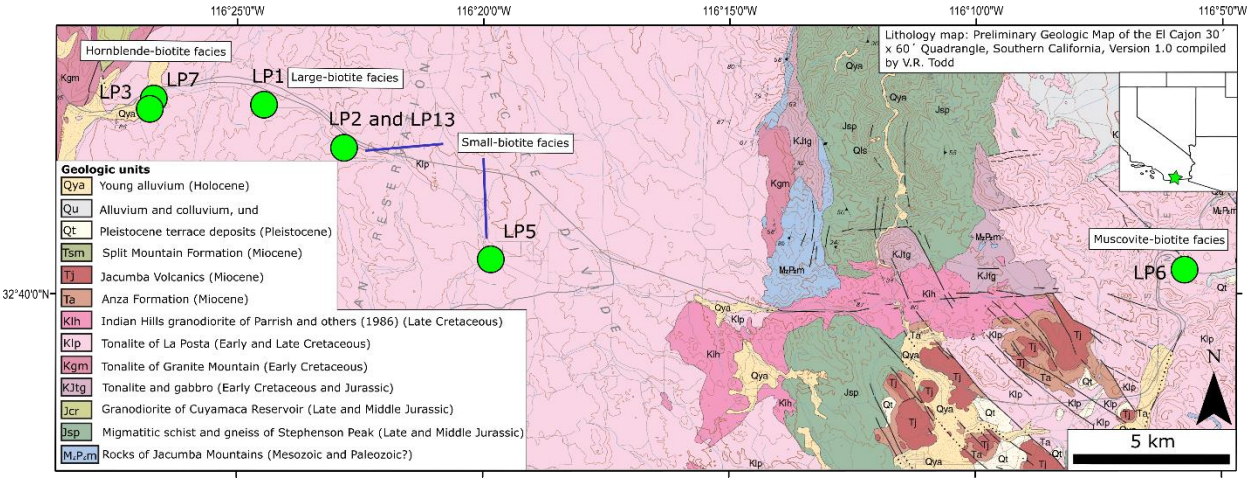

Figure 3.1: Geologic map of the La Posta region of the Peninsular Ranges batholith with an inset map showing the location in relation to state lines in the southwestern United States. Geologic map and units are from Todd (2004). The green dots show sample locations. From left to right, the units are hornblende-biotite facies (LP3 and LP7), large-biotite facies (LP1), small-biotite facies (LP2 and LP5), and muscovite-biotite facies (LP6). For reference, the light pink unit is the La Posta pluton.

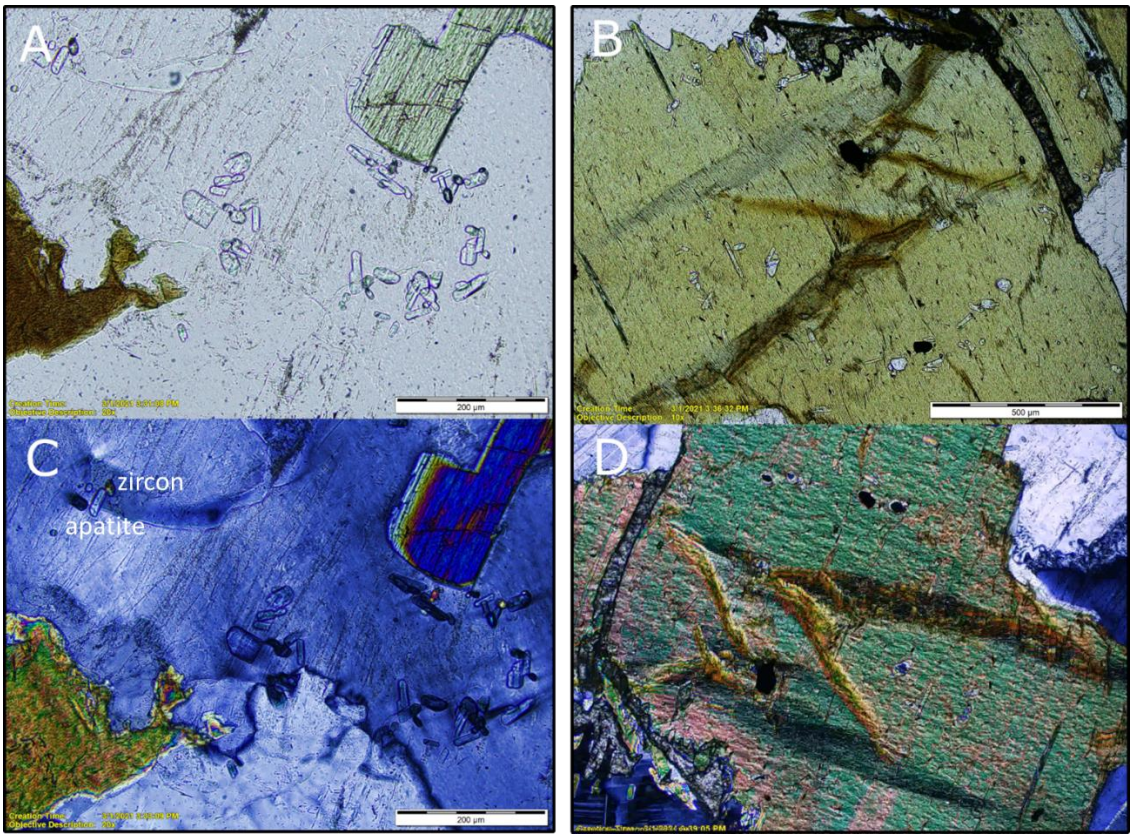

Figure 3.2: Petrographic images of thin sections from the small biotite facies of the La Posta pluton. Top images show plane polarized light images and bottom images show cross-polarized light images of samples. Within the black boxes, the images are showing the same area of a thin section (apatite has first order grey birefringence; zircon has 3rd order birefringence). The distribution of zircon is inconsistent with the ‘pileup’ model.

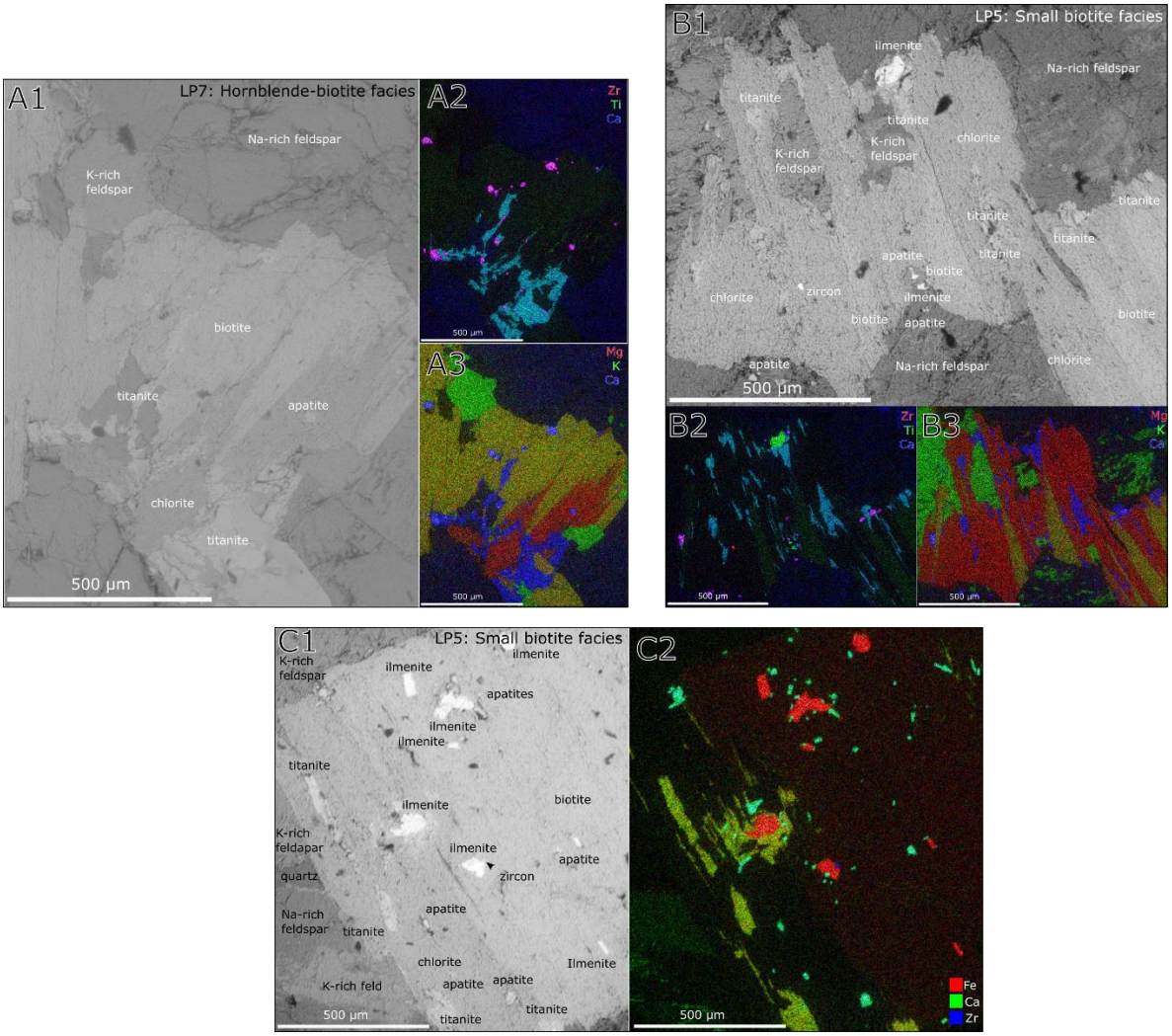

Figure 3.3: Images showing the mineralogy of sample LP7 (A) and LP5 (B and C) from the hornblende-biotite and small biotite facies of the La Posta pluton, respectively. A1, B1, C1) Backscatter electron images of the studied area with some mineralogy labeled. A2 and 3) show elemental compositions with Zr-Ti-Ca (A2) and Mg-K-Ca (A3) as red-green-blue. Of note, the light blue color and pink in (B) shows titanite and apatite, respectively. P and Zr emit similar x-rays, so these two elements often show up on the others' patterns. The mineral showing red and green in (A3) is biotite. Chlorite is shown in red. Green shows K-rich feldspar, and dark blue shows titanite and apatite. Na-rich feldspar is black-blue. A1, 2, and 3 show the same field of view. B2)

and 3) show Zr-Ti-Ca and Mg-K-Ca, respectively, as red-green-blue. In (B2), light blue shows titanite, green shows ilmenite, pink shows apatite, and red shows zircon. In (B3), blue shows titanite and apatite and red-green shows biotite. C2) shows elemental compositions with Fe-Ca-Zr as red-green-blue. Red shows ilmenite and green shows titanite. Bluish-green shows apatite.

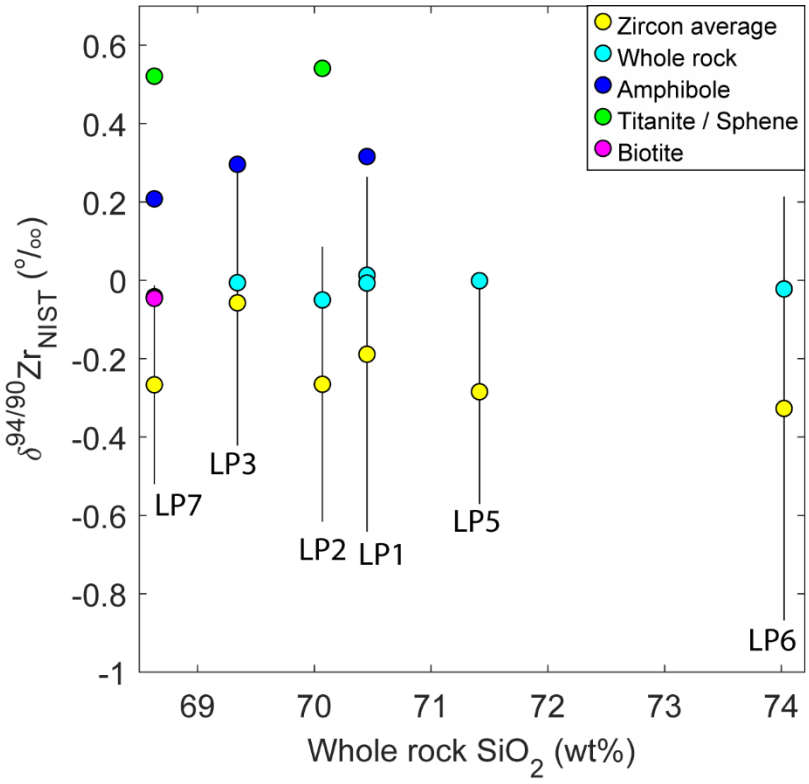

Figure 3.4: Figure shows all Zr isotope analyses in this study: zircons (averaged from all analyses for each rock, yellow), whole rock (cyan), amphibole (blue), titanite/sphene (green), and biotite (pink). Error bars on zircon analyses, which were conducted by SIMS, are 1 s.d. Error bars for

other measurements, which were conducted by DS-MC-ICPMS, are smaller than the plotted symbols.

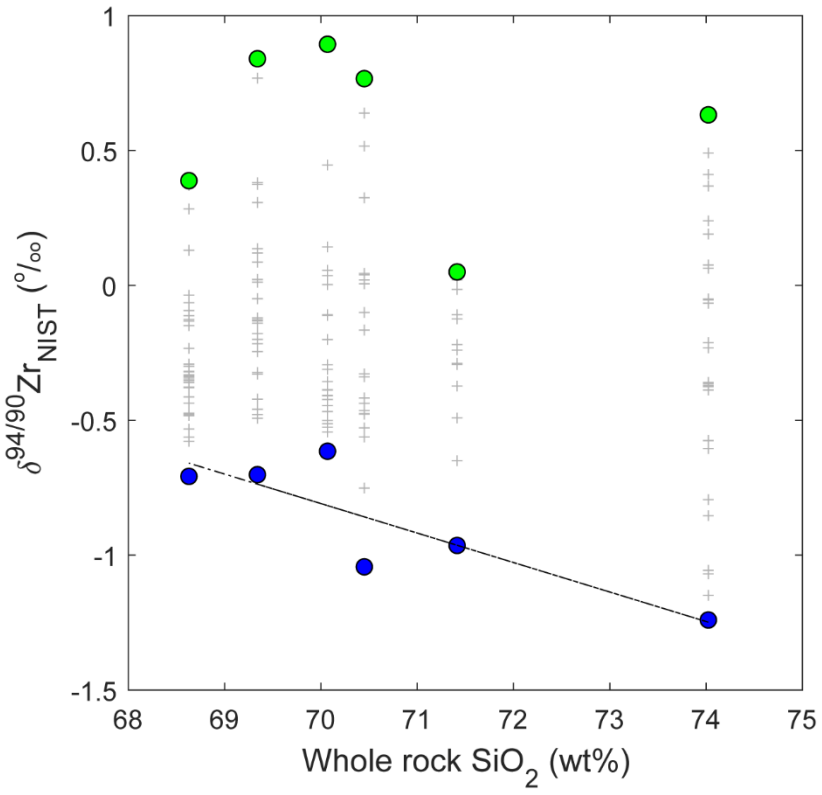

Figure 3.5: Figure shows all Zr isotope analyses of zircon in this study vs. whole rock SiO_2: the zircon with the heaviest Zr isotopic composition (green circle), zircon with the lightest Zr isotopic composition (blue circle), and all zircons measured for each rock (grey cross). Best fit line of each rocks' minimum isotopic composition vs. whole rock SiO_2 shown with a dot-dash line.

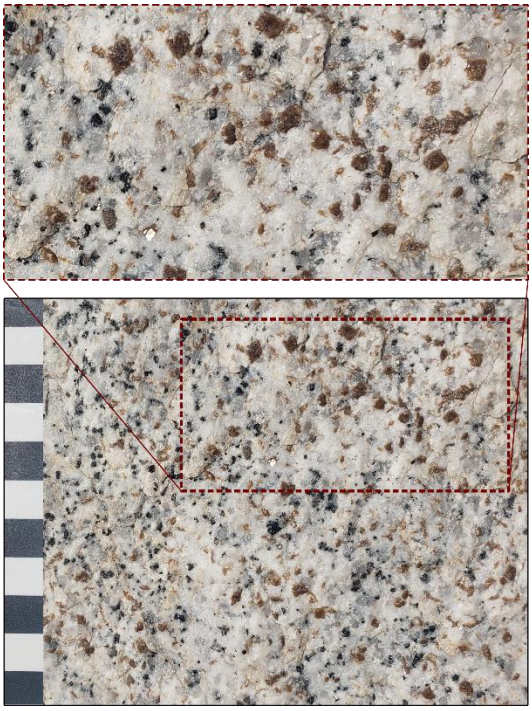

Figure 3.6: The bottom image shows a titanite-rich portion of the LP13 outcrop, close to the LP2 sampling location. The burgundy dashed box in the lower image shows the location of the upper image. The vertical measurement of each square on the left side corresponds to 1 cm.

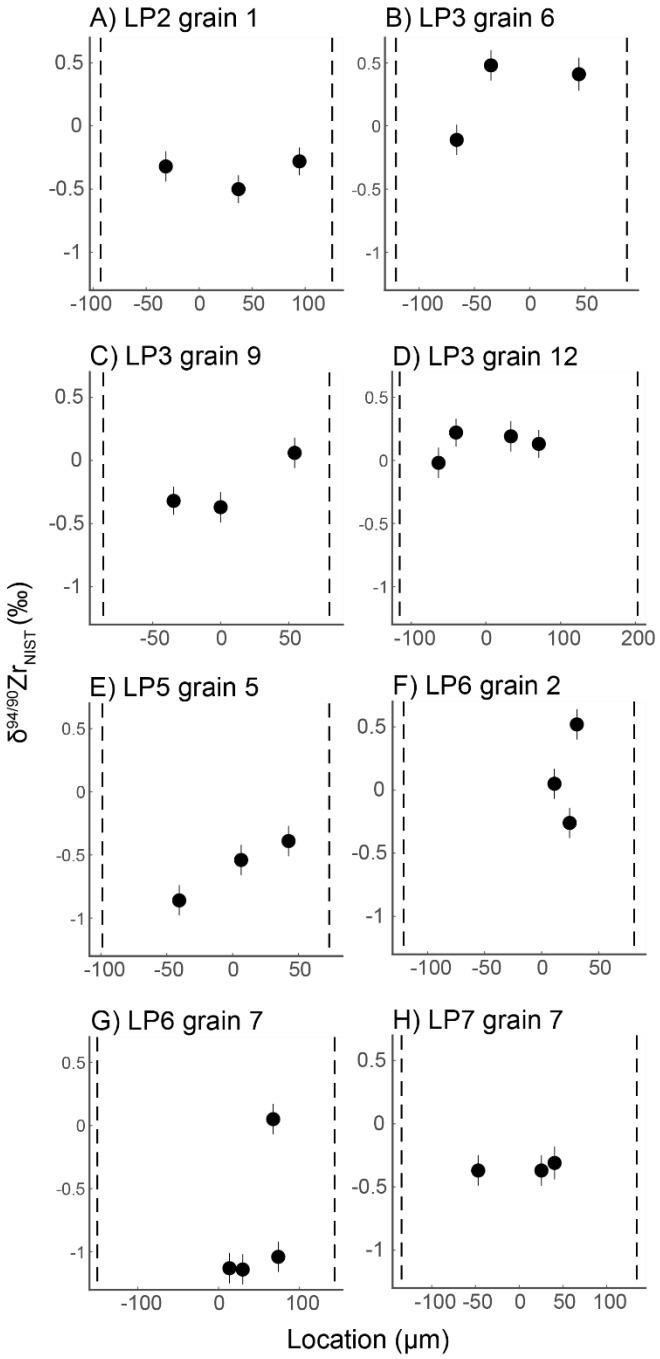

Figure 3.7: Isotopic profiles of grains from the La Posta pluton. 0 on the x-axis corresponds to the core of the grain, and the dotted black lines show the edges of grains. Cathodoluminescence images of these grains can be found in the Supplementary Material. Error bars are showing 1 s.d. The width of an analytical spot is less than the horizontal length of a spot.

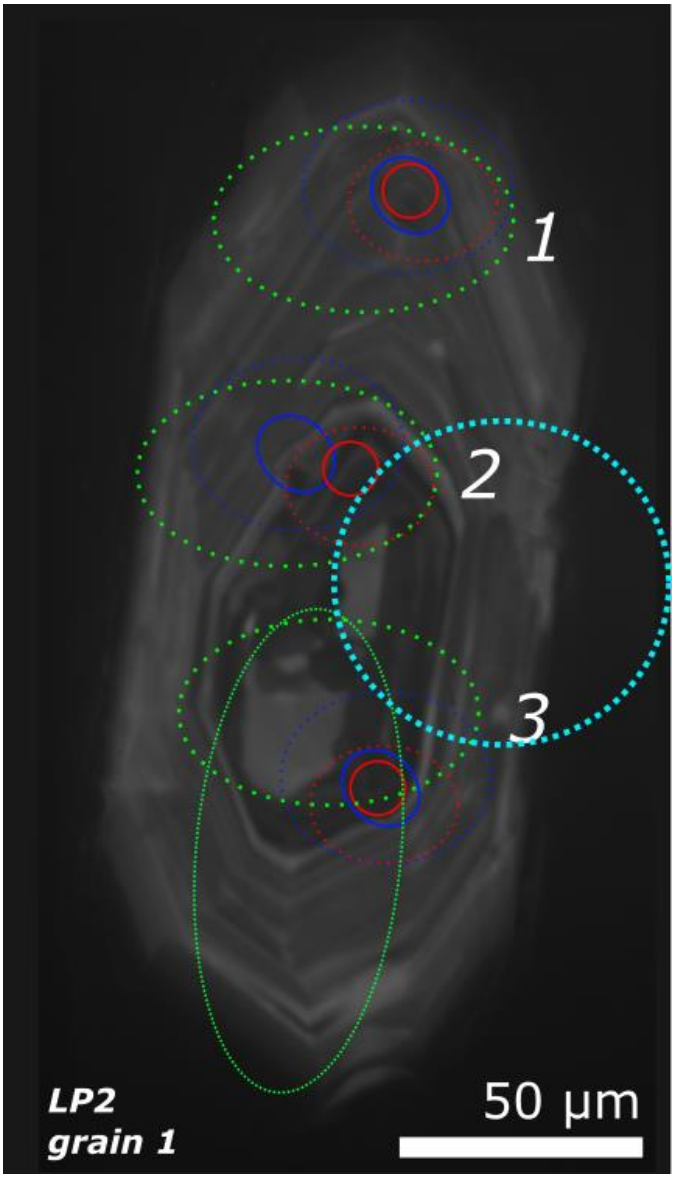

Figure 3.8: Cathodoluminescence image of LP2 grain 1 with Zr isotopic analyses, trace element (*ims*1290), trace element (*ims*1270), and U-Pb spots shown in red, blue, light blue, and green, respectively. U-Pb analyses from the November and December 2020 sessions are shown with thicker and thinner dotted lines, respectively. White numbers adjacent to spots show analysis

numbers in Table S5. This grain contains an inherited core which is Proterozoic in age surrounded by Cretaceous growth.

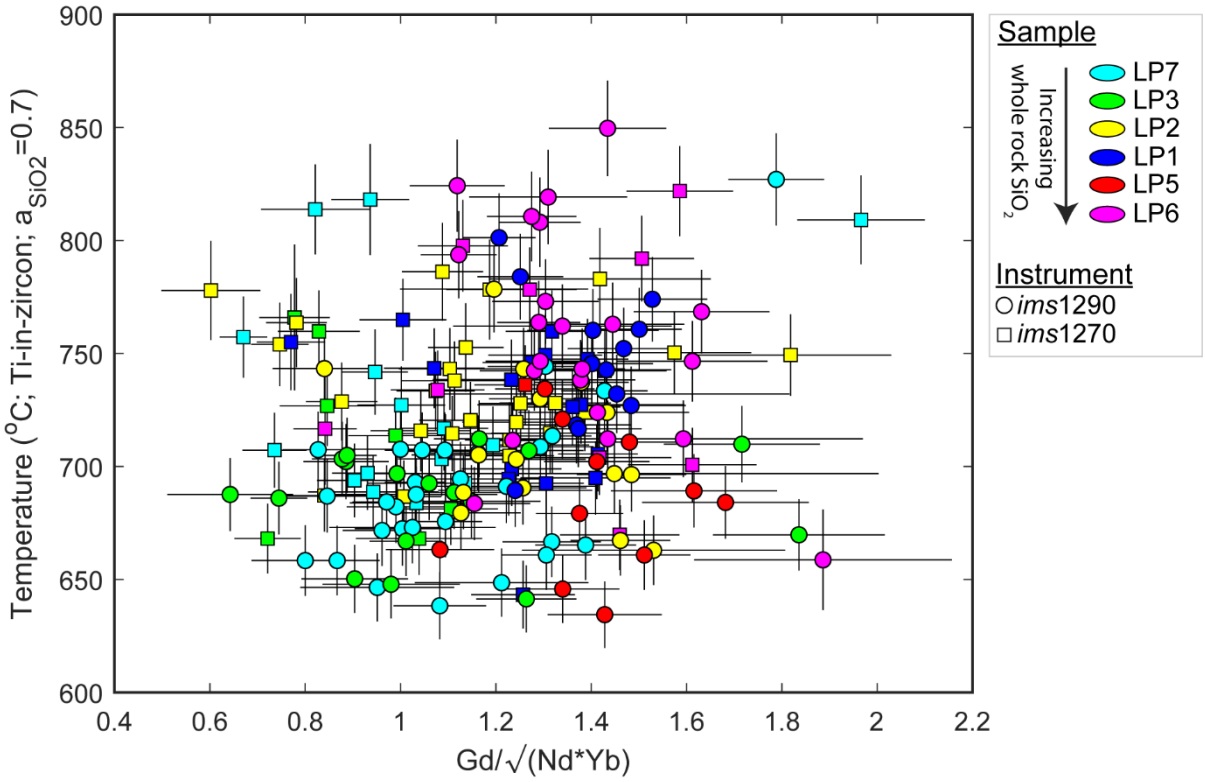

Figure 3.9: Gd/Gd* vs. Ti-in-zircon temperature for all zircons analyzed. Different units within the zoned La Posta pluton are shown in different colors. Generally, less silicic rocks have both lower Gd/Gd* and lower Ti-in-zircon temperatures showing indicating a higher degree of titanite fractionation prior to zircon crystallization. The heatmap shows an increase in Ti-in-zircon temperature with increasing Gd/Gd*. Titanite depletes MREE in glasses (Colombini et al., 2011), and Gd/Gd* is used to represent that depletion here. Square boxes represent analyses made using the *ims*1270 and circle boxes show analyses made using the *ims*1290.

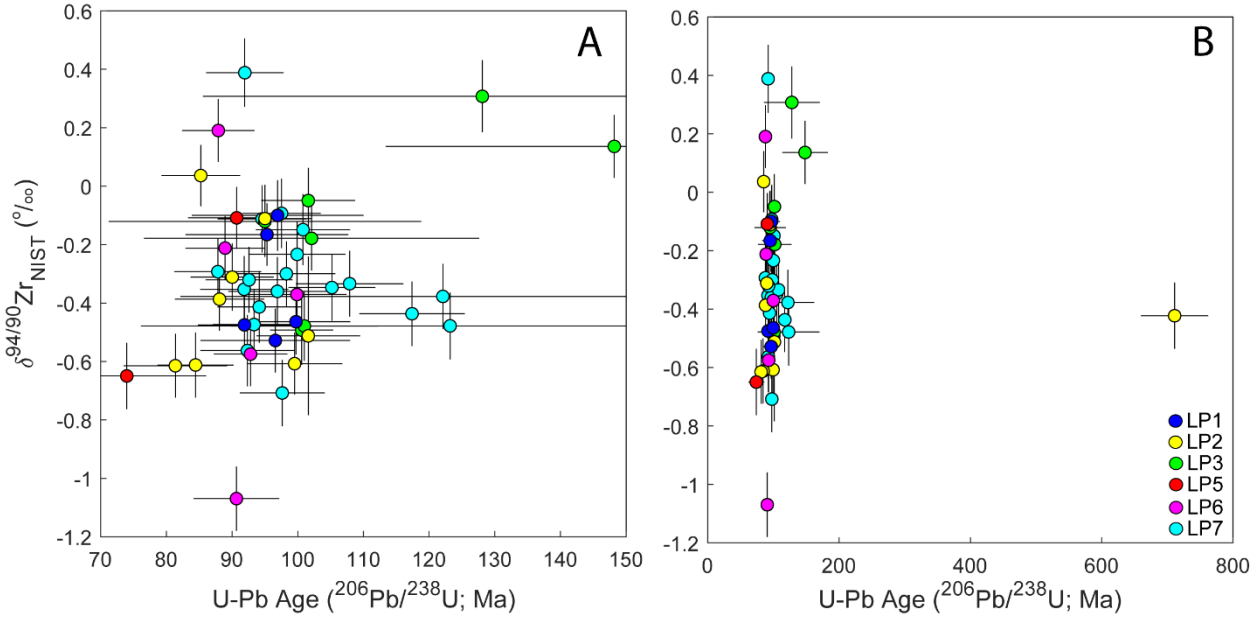

Figure 3.10: U-Pb ages vs. Zr stable isotope values of zircons from the La Posta pluton with different colors showing different samples. All analyses contain >95% $^{206}Pb^*$ and are within 30% of concordance.

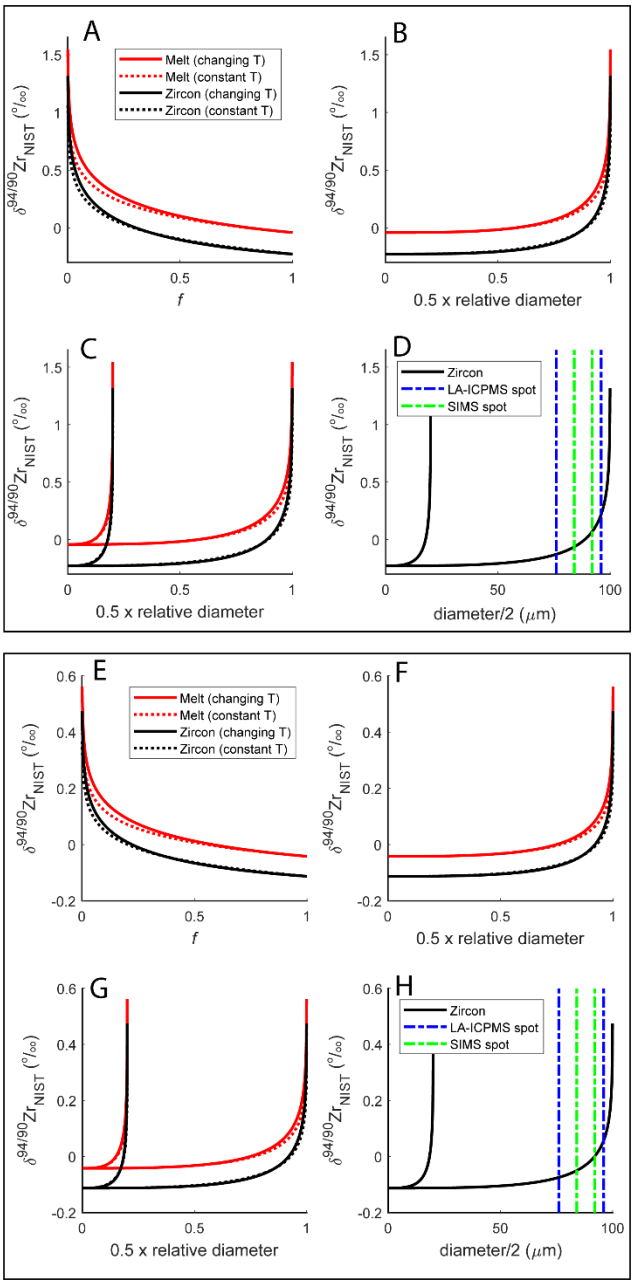

Figure 3.11: A-D show relationships as modeled using the ionic model (Young et al., 2015); E-H show relationships modeled using force constants calculated by Chen et al. (2020); A, B, C. E, F, G) Modeled zircon isotope profiles showing the impacts of constant vs. changing T on Zr isotope evolution for a tabular zircon that we model as a rectangle. B and F) shows a system where all three zircon axis are the same length (x = y = z) and C and G) shows a system where x = y and z=

5x. D and H) shows a grain where z = 200 μm and x = y = 40 μm along with the approximate size of LA-ICPMS and SIMS beams in blue and green, respectively. Red and black lines show the isotopic composition of melt and zircon, respectively and solid and dotted lines show the isotopic trajectory of a system with a constantly changing T and an isothermal system, respectively.

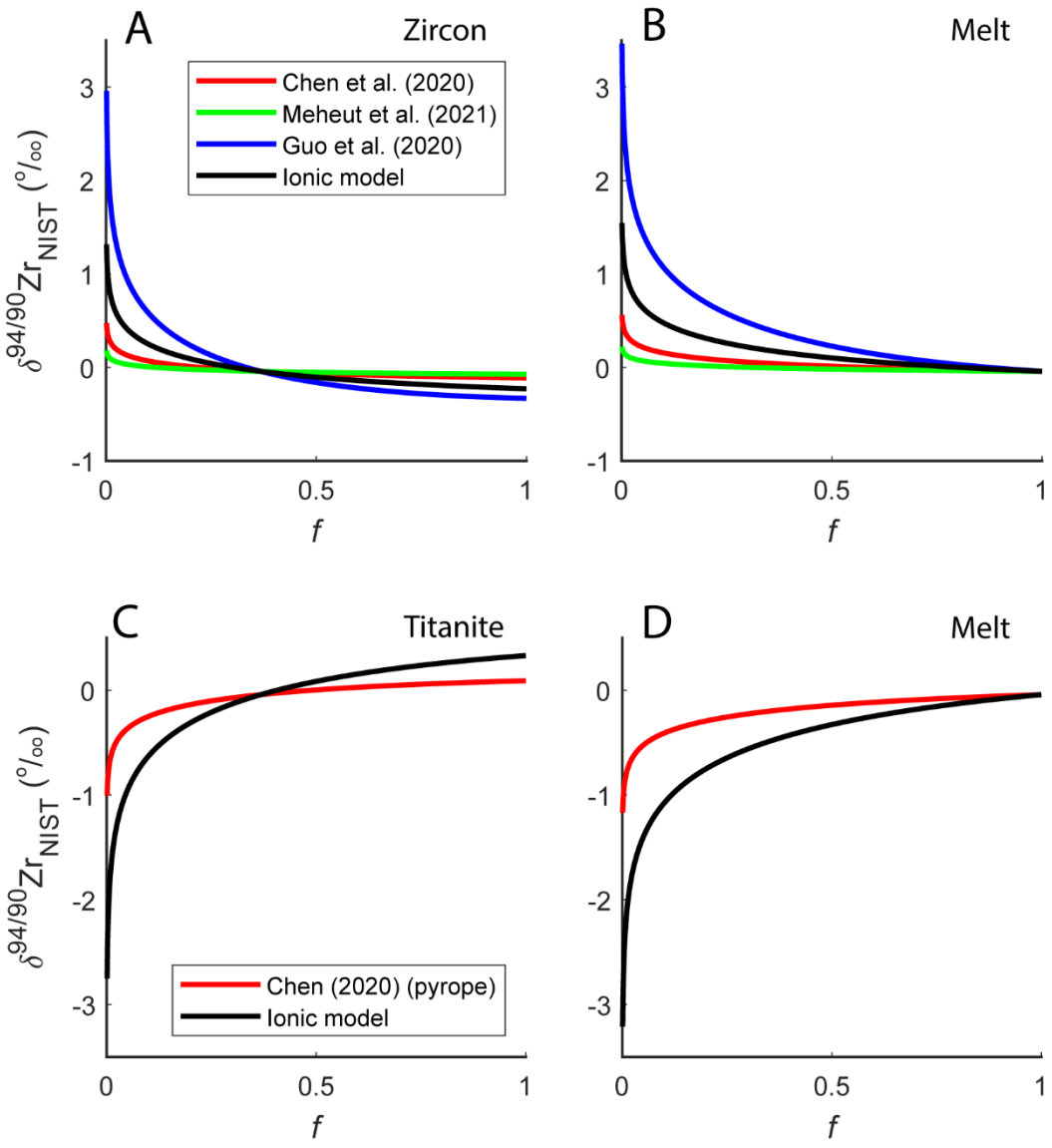

Figure 3.12: Modeled evolution curves if only a single phase is crystallizing. A) shows isotope evolution of zircon if zircon crystallizes as a result of Rayleigh fractionation and B) shows the resultant melt evolution. C) shows the Zr isotopic evolution of sphene if it crystallizes alone and D) shows the isotopic evolution of the melt as a result of titanite crystallization. All profiles show a 100 K change (1006 → 906 K). In the upper two subfigures, zircon is the only phase crystallizing. In the bottom two, titanite is the only phase crystallizing.

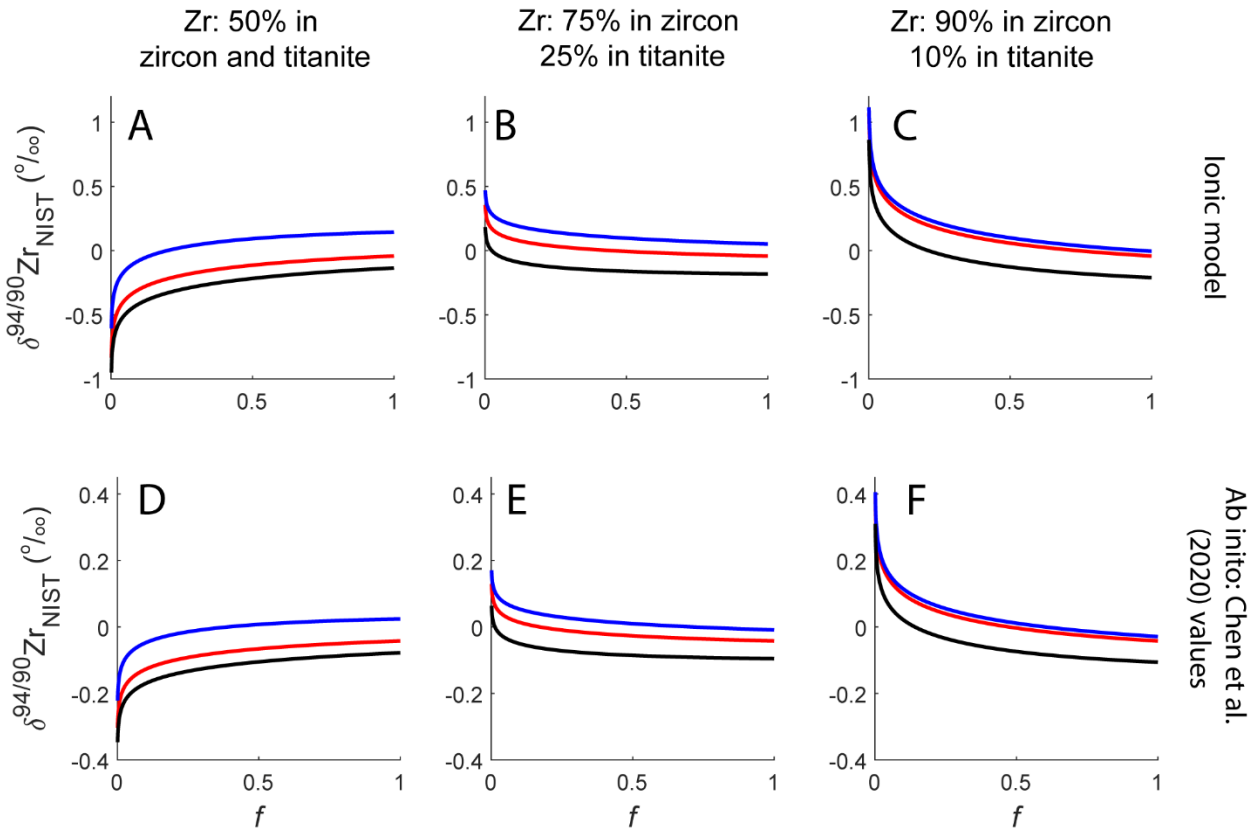

Figure 3.13: Influence of co-crystallizing phases on isotope profiles shown through fraction of Zr remaining (f) vs. $\delta^{94/90}$Zr (‰) for a modeled zircon for a system with a constant change in temperature. Red, blue, and black lines show the isotopic composition of melt, titanite, and zircon, respectively. Figures A-C show fractionation factors calculated using the ionic model. Figures D-F show profiles calculated using fractionation factors calculated using values from Chen et al. (2020).

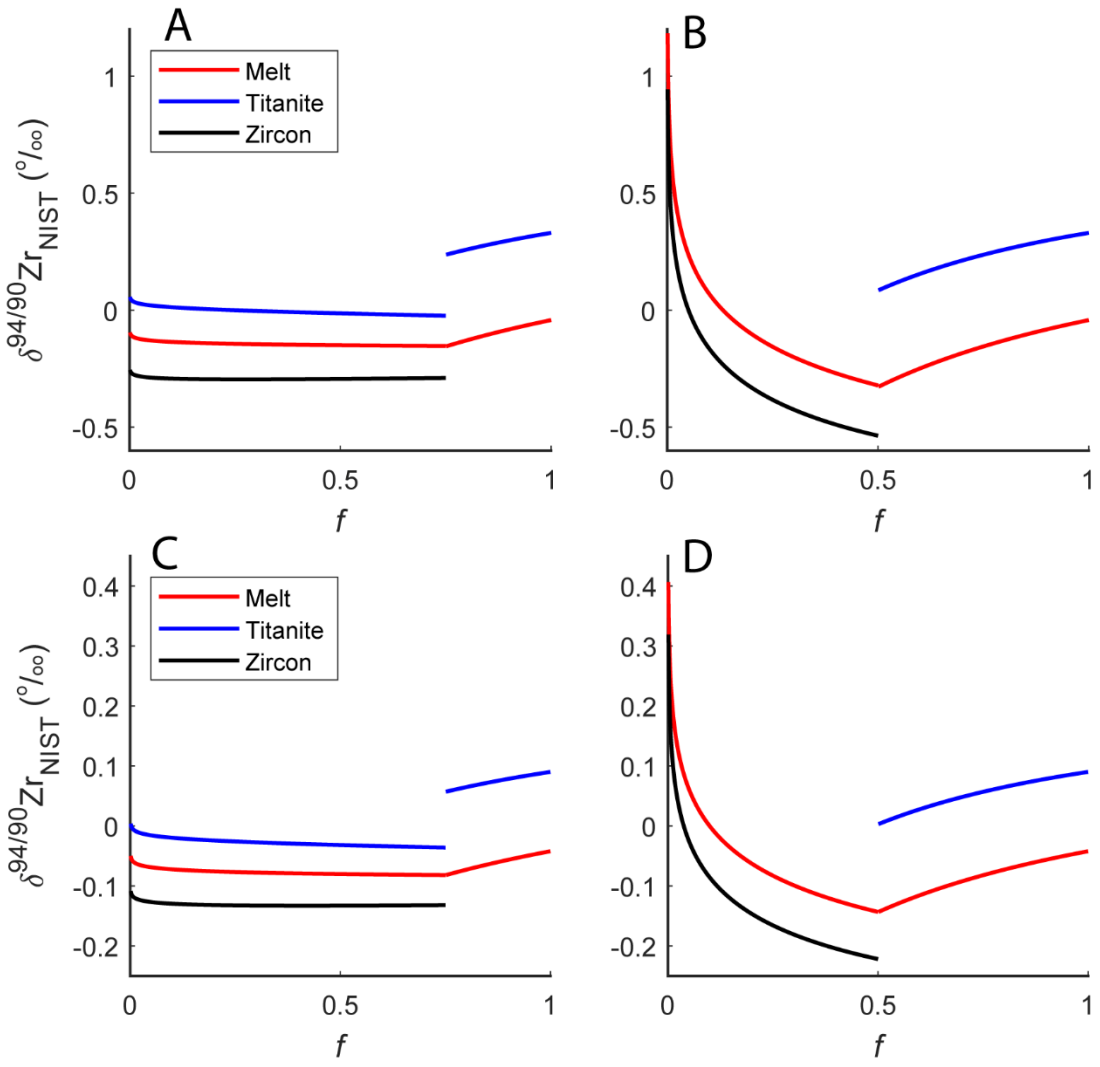

Figure 3.14: Fraction of Zr remaining (f) vs. $\delta^{94/90}$Zr (‰) for a modeled zircon for two systems with 50% of Zr in zircon and 50% of Zr in titanite, both with a constant change in T. Figures A and C show all Zr partitioning into titanite until f = 0.75 followed by co-crystallization of titanite and zircon where 1/ 3 of Zr partitions into titanite and 2/3 partitions into zircon. In Figures B and D, Zr partitions into titanite until f = 0.5 followed by Zr partitioning into zircon until f = 0. Red, blue, and black lines show the isotopic composition of melt, titanite, and zircon, respectively. Figures A-B show fractionation factors calculated using the ionic model. Figures C-D show profiles calculated using fractionation factors calculated using values from Chen et al. (2020).

3.9 References

Akram W., Schönbächler M., Sprung P. and Vogel N., 2013, Zirconium - Hafnium isotope evidence from meteorites for the decoupled synthesis of light and heavy neutron-rich nuclei. The Astrophysical Journal. **777**. 1-12.

Bea F., Montero P. and Ortega M., 2006, A LA-ICP-MS evaluation of Zr reservoirs in common crustal rocks: Implications for Zr and Hf geochemistry, and zircon-forming processes. The Canadian Mineralogy, **44**, 693–714.

Bell E. A., Boehnke P., Barboni M. and Harrison T. M., 2019, Tracking chemical alteration in magmatic zircon using rare earth element abundances. Chemical Geology, **510**, 56–71. Available at: https://doi.org/10.1016/j.chemgeo.2019.02.027.

Bell E. A., Boehnke P. and Harrison T. M., 2016, Recovering the primary geochemistry of Jack Hills zircons through quantitative estimates of chemical alteration. Geochimica Cosmochimca Acta, **191**, 187–202. Available at: http://dx.doi.org/10.1016/j.gca.2016.07.016.

Bell E. A. and Kirkpatrick H. M., 2021, Effects of crustal assimilation and magma mixing on zircon trace element relationships across the Peninsular Ranges Batholith. Chemical Geology, **586**, 120616. https://www.sciencedirect.com/science/article/pii/S0009254121005593.

Bell E. A., Kirkpatrick H. M. and Harrison T. M. Crystallization order effects on inclusion assemblages in magmatic accessory minerals and implications for the detrital record.

Bindeman I. N. and Melnik O. E., 2016, Zircon survival, rebirth and recycling during crustal

melting, magma crystallization, and mixing based on numerical modelling. Journal of Petrology, **57**, 437–460.

Blundy J. and Wood B., 2003, Partitioning of trace elements between crystals and melts. Earth and Planetary Science Letters **210**, 383–397.

Blundy J. and Wood B., 1994, Prediction of crystal-melt partition coefficients from elastic moduli. Nature, **372**, 452–454.

Boehnke P., Watson E. B., Trail D., Harrison T. M. and Schmitt A. K., 2013, Zircon saturation re-revisited. Chemical Geology, **351**, 324–334. Available at: http://dx.doi.org/10.1016/j.chemgeo.2013.05.028.,

Carley T. L., Miller C. F., Wooden J. L., Bindeman I. N. and Barth A. P., 2011, Zircon from historic eruptions in Iceland: Reconstructing storage and evolution of silicic magmas. Mineraology and Petrology, **102**, 135–161.

Chen X., Wang W., Zhang Z., Nie N. X. and Dauphas N., 2020, Evidence from Ab Initio and Transport Modeling for Diffusion-Driven Zirconium Isotopic Fractionation in Igneous Rocks. ACS Earth Space Chemistry, **4**, 1572–1595.

Clinkenbeard J. P. and Walawender M. J., 1989, Mineralogy of the La Posta pluton: implications for the origin of zoned plutons in the eastern Peninsular Ranges batholith, southern and Baja California. American Mineralogist, **74**, 1258–1269.

Colombini L. L., Miller C. F., Gualda G. A. R., Wooden J. L. and Miller J. S., 2011, Sphene and zircon in the Highland Range volcanic sequence (Miocene, southern Nevada, USA): Elemental partitioning, phase relations, and influence on evolution of silicic magma.

Mineraology and Petrology, **102**, 29–50.

Davidson J., Turner S., Handley H., Macpherson C. and Dosseto A., 2007, Amphibole “sponge” in arc crust? Geology **35**, 787–790.

Ding H., Zhang Z. and Kohn M. J., 2021, Late Cretaceous hydrous melting and reworking of juvenile lower crust of the eastern Gangdese magmatic arc, southern Tibet. Gondwana Research, Available at: https://doi.org/10.1016/j.gr.2021.07.017.

Farges F., Ponader C. W. and Brown G. E., 1991, Structural environments of incompatible elements in silicate glass/melt systems: I. Zirconium at trace levels. Geochimica Cosmochimica Acta, **55**, 1563–1574.

Feng L., Hu W., Jiao Y., Zhou L., Zhang W., Hu Z. and Liu Y., 2020, High-precision stable zirconium isotope ratio measurements by double spike thermal ionization mass spectrometry. Journal of Analytical Mass Spectrometry, **35**, 736–745.

Ferry J. M. and Watson E. B., 2007, New thermodynamic models and revised calibrations for the Ti-in-zircon and Zr-in-rutile thermometers. Contributions to Mineralogy and Petrology, **154**, 429–437.

Gastil G., Diamond J., Knaack C., Walawender M., Marshall M., Boyles C., Chadwick B. and Erskine B., 1990, The problem of the magnetite/ ilmenite boundary in southern and Baja California. Geological Society of America Memoirs, **174**, 19–32.

Gastil R. G., Phillips R. P. and Allison E. C., 1975, Reconnaissance Geology of the State of Baja California. In Reconnaissance Geology of the State of Baja California (eds. R. G. Gastil, R. P. Phillips, and E. C. Allison). Geological Society of America. Available at:

https://doi.org/10.1130/MEM140-p1.

Grove M., Lovera O. and Harrison T. M., 2003, Late Cretaceous cooling of the east-central Peninsular Ranges batholith (33°N): Relationship to la Posta pluton emplacement, Laramide shallow subduction, and forearc sedimentation. Special Papers of the Geological Society of America, **374**, 355–379.

Guo J.-L., Wang Z., Zhang W., Moynier F., Cui D., Hu Z. and Ducea M. N., 2020, Significant Zr isotope variations in single zircon grains recording magma evolution history. Proceedings of the National Academy of Sciences, **117**, 21125–21131. Available at: https://www.pnas.org/content/117/35/21125.

Hammarstrom J. M. and Zen E., 1986, Aluminum in hornblende: an empirical igneous geobarometer. American Mineralogist, **71**, 1297–1313.

Harper B. E., Miller C. F., Koteas G. C., Cates N. L., Wiebe R. A., Lazzareschi D. S. and Cribb J. W., 2004, Granites, dynamic magma chamber processes and pluton construction: The Aztec Wash pluton, Eldorado Mountains, Nevada, USA. Special Paper of the Geological Society of America, **389**, 277–295.

Harrison T. M. and Watson E. B., 1983, Kinetics of zircon dissolution and zirconium diffusion in granitic melts of variable water content. Contributions to Mineralogy and Petrology, **84**, 66–72.

Hauri E. H., Wagner T. P. and Grove T. L., 1994, Experimental and natural partitioning of Th, U, Pb and other trace elements between garnet, clinopyroxene and basaltic melts. Chemical Geology, **117**, 149–166.

Hayden L. A., Watson E. B. and Wark D. A., 2008, A thermobarometer for sphene (titanite). Contributions to Mineralogy and Petrology, **155**, 529–540.

Hirata T., 2001, Determinations of Zr isotopic composition and U-Pb ages for terrestrial and extraterrestrial Zr-bearing minerals using laser ablation-inductively coupled plasma mass spectrometry: Implications for Nb-Zr isotopic systematics. Chemical Geology, **176**, 323–342.

Hirata T. and Yamaguchi T., 1999, Isotopic analysis of zirconium using enhanced sensitivity-laser ablation-multiple collector-inductively coupled plasma mass spectrometry. Journal of Analytical Mass Spectrometry, **14**, 1455–1459. Available at: http://dx.doi.org/10.1039/A901389J.

Hollister L. S., Grissom G. C., Peters E. K., Stowell H. H. and Sisson V. B., 1987, Confirmation of the empirical correlation of Al in hornblende with pressure of solidification of calc-alkaline plutons. American Mineralogist, **72**, 231–239.

Huang C., Wang H., Yu H. M., Feng L. P., Xie L. W., Yang Y. H., Wu S. T., Xu L. and Yang J. H., 2021, Further characterization of SA01 and SA02 zircon reference materials for Si and Zr isotopic compositions: Via femtosecond laser ablation MC-ICP-MS. Journal of Analytical Mass Spectrometry, **36**, 2192–2201.

Ibañez-Mejia M. and Tissot F. L. H. H., 2019, Extreme Zr stable isotope fractionation during magmatic fractional crystallization. Science Advances, **5**, 1–14.

Iizuka T., Lai Y. J., Akram W., Amelin Y. and Schönbächler M., 2016, The initial abundance and distribution of 92Nb in the Solar System. Earth and Planetary Science Letters **439**, 172–

181. Available at: http://dx.doi.org/10.1016/j.epsl.2016.02.005.

Inglis E. C., Creech J. B., Deng Z. and Moynier F., 2018, High-precision zirconium stable isotope measurements of geological reference materials as measured by double-spike MC-ICPMS. Chemical Geology, **493**, 544–552. Available at: https://doi.org/10.1016/j.chemgeo.2018.07.007.

Inglis E. C., Moynier F., Creech J., Deng Z., Day J. M. D., Teng F. Z., Bizzarro M., Jackson M. and Savage P., 2019, Isotopic fractionation of zirconium during magmatic differentiation and the stable isotope composition of the silicate Earth. Geochimica Cosmochimica Acta, **250**, 311–323.

Kimbrough D. L., Smith D. P., Mahoney J. B., Moore T. E., Grove M., Gordon R., Ortega-rivera A., Fanning C. M., Kimbrough D. L., Sciences G., Diego S. and Diego S., 2001, Forearc-basin sedimentary response to rapid Late Cretaceous batholith emplacement in the Peninsular Ranges of southern and Baja California. Geology, **29**, 491–494.

Klaver M., MacLennan S. A., Ibañez-Mejia M., Tissot F. L. H., Vroon P. Z. and Millet M. A., 2021, Reliability of detrital marine sediments as proxy for continental crust composition: The effects of hydrodynamic sorting on Ti and Zr isotope systematics. Geochimica Cosmochimica Acta, **310**, 221–239.

Krummenacher D. and Doupont J., 1975, K-Ar Apparent Ages, Peninsular Ranges Batholith, Southern California and Baja California. Bulletin of the Geological Society of America, **86**, 760–768.

Liu M. C., McKeegan K. D., Harrison T. M., Jarzebinski G. and Vltava L., 2018, The Hyperion-

II radio-frequency oxygen ion source on the UCLA ims1290 ion microprobe: Beam characterization and applications in geochemistry and cosmochemistry. International Journal of Mass Spectrometry, **424**, 1–9. Available at: http://dx.doi.org/10.1016/j.ijms.2017.11.007.

Louvel M., Sanchez-Valle C., Malfait W. J., Testemale D. and Hazemann J. L., 2013, Zr complexation in high pressure fluids and silicate melts and implications for the mobilization of HFSE in subduction zones. Geochimica Cosmochimica Acta, **104**, 281–299.

Mahon K. I., 1996, The New "York" Regression: Application of an Improved Statistical Method to Geochemistry. International Geology Review, **38**, 293–303.

Méheut M., Ibañez-Mejia M. and Tissot F., 2021, Drivers of zirconium isotope fractionation in Zr-bearing phases and melts: The roles of vibrational, nuclear field shift and diffusive effects. Geochimica Cosmochimica Acta, **292**, 217–234.

Miggins D. P., Premo W. R., Snee L. W., Yeoman R., Naeser N. D., Naeser C. W. and Morton D. M., 2014, Thermochronology of Cretaceous batholithic rocks in the northern Peninsular Ranges batholith, southern California: Implications for the Late Cretaceous tectonic evolution of southern California. Memoirs of the Geological Society of America, **211**, 199–261.

Minster J. F. and Allègre C. J., 1982, The isotopic composition of zirconium in terrestrial and extraterrestrial samples: implications for extinct 92Nb. Geochimica Cosmochimica Acta, **46**, 565–573.

Minster J. F. and Ricard L. P., 1981, The isotopic contosition of zirconium. International Journal

of Mass Spectrometry and Ion Physics, **37**, 259–272. Available at: https://www.sciencedirect.com/science/article/pii/0020738181800484.

Mungall J. E., Dingwell D. B. and Chaussidon M., 1999, Chemical diffusivities of 18 trace elements in granitoid melts. Geochimica Cosmochimica Acta, **63**, 2599–2610.

Ortega-Rivera A., 2003, Geochronological constraints on the tectonic history of the Peninsular Ranges batholith of Alta and Baja California: Tectonic implications for western México. Special Paper of the Geological Society of America, **374**, 297–335.

Poletti J. E., Cottle J. M., Hagen-Peter G. A. and Lackey J. S., 2016, Petrochronological Constraints on the Origin of the Mountain Pass Ultrapotassic and Carbonatite Intrusive Suite, California. Journal of Petrology, **57**, 1555–1598. Available at: https://doi.org/10.1093/petrology/egw050.

Premo W. R., Morton D. M., Wooden J. L. and Fanning C. M., 2014, U-Pb zircon geochronology of plutonism in the northern Peninsular Ranges batholith, southern California: Implications for the Late Cretaceous tectonic evolution of southern California. Memoir of the Geological Society of America, **211**, 145–180.

Quidelleur X., Grove M., Lovera O. M., Harrison T. M., Yin A. and Ryerson F. J., 1997, Thermal evolution and slip history of the Renbu Zedong Thrust, southeastern Tibet. Journal of Geophysical Research Solid Earth **102**, 2659–2679. https://doi.org/10.1029/96JB02483.

Reid M. R., Coath C. D., Harrison T. M. and McKeegan K. D., 1997, Prolonged residence times for the youngest rhyolites associated with Long Valley Caldera:230Th—238U ion microprobe dating of young zircons. Earth and Planetary Science Letters **150**, 27–39.

Robinson K., Gibbs G. V. and Ribbe P. H., 1971, The Structure of Zircon: a Comparison With Garnet. American Mineralogist, **56**, 782–790.

Schmitt A. K., 2011, Uranium Series Accessory Crystal Dating of Magmatic Processes. Annual Reviews of Earth and Planetary Science, **39**, 321–349. https://doi.org/10.1146/annurev-earth-040610-133330.

Schmitz M. D., Bowring S. A. and Ireland T. R., 2003, Evaluation of Duluth Complex anorthositic series (AS3, zircon as a U-Pb geochronological standard: New high-precision isotope dilution thermal ionization mass spectrometry results. Geochimica Cosmochimica Acta, **67**, 3665–3672.

Schönbächler M., Lee D. C., Rehkämper M., Halliday A. N., Fehr M. A., Hattendorf B. and Günther D., 2003, Zirconium isotope evidence for incomplete admixing of r-process components in the solar nebula. Earth and Planetary Science Letters **216**, 467–481.

Schönbächler M., Rehkämper M., Fehr M. A., Halliday A. N., Hattendorf B. and Günther D., 2005, Nucleosynthetic zirconium isotope anomalies in acid leachates of carbonaceous chondrites. Geochimica Cosmochimica Acta, **69**, 5113–5122.

Shaw S. E., Todd V. R. and Grove M., 2003, Jurassic peraluminous gneissic granites in the axial zone of the Peninsular Ranges, southern California. Special Paper of the Geological Society of America, **374**, 157–183.

Shaw S. E., Todd V. R., Kimbrough D. L. and Pearson N. J., 2014, A west-to-east geologic transect across the Peninsular Ranges batholith, San Diego County, California: Zircon 176Hf/177Hf evidence for the mixing of crustal- and mantle-derived magmas, and

comparisons with the Sierra Nevada batholith. Memoir of the Geological Society of America, **211**, 499–536.

Silver L. T. and Chappell B. W., 1988, The Peninsular Ranges Batholith: An insight into the evolution of the Cordilleran batholiths of southwestern North America. Transactions of the Royal Society of Edinburgh Earth Science **79**, 105–121.

Silver L. T., Taylor Jr. H. P. and Chappell B. W., 1979, Some petrological, geochemical, and geochronological observations of the Peninsular Ranges batholith near the International border of the U.S.A. and Mexico. In Mesozoic Crystalline Rocks, Geological Society of America Annual Meeting Guidebook (eds. P. L. Abbot and V. R. Todd). pp. 83–110.

Simmons E. C. and Hedge C. E., 1978, Minor-element and Sr-isotope geochemistry of tertiary stocks, Colorado mineral belt. Contributions to Mineralogy and Petrology, **67**, 379–396.

Speer J. A. and Gibbs G. V., 1976, The crystal structure of synthetic titanite, CaTiOSiO4, and the domain textures of natural titanites. American Mineralogist, **61**, 238–247.

Tian S., Inglis E. C., Creech J. B., Zhang W., Wang Z., Hu Z., Liu Y. and Moynier F., 2020, The zirconium stable isotope compositions of 22 geological reference materials, 4 zircons and 3 standard solutions. Chemical Geology, **555**, 119791. Available at: https://doi.org/10.1016/j.chemgeo.2020.119791.

Todd V. R. and Shaw S. E., 1985, S-type granitoids and an I-S line in the Peninsular Ranges batholith, southern California. Geology, **13**, 231–233.

Tompkins H. G. D., Zieman L. J., Ibañez-Mejia M. and Tissot F. L. H., 2020, Zirconium stable isotope analysis of zircon by MC-ICP-MS: methods and application to evaluating intra-

crystalline zonation in a zircon megacryst. Journal of Analytical Mass Spectrometry, **35**, 1167–1186.

Trail D., Watson E. B. and Tailby N. D., 2011, The oxidation state of Hadean magmas and implications for early Earth's atmosphere. Nature **480**, 79–82. Available at: http://dx.doi.org/10.1038/nature10655.

Walawender M. J., Gastil G., Clinkenbeard J. P., Mccormick W. V, Eastman B. G., Wernicke R. S., Wardlaw M. S., Gunn S. H. and Smith B. M., 1990, Orgin and evolution of the zoned La Posta-type plutons, eastern Peninsular Ranges batholith, southern and Baja California. Memoir of the Geological Society of America, **174**, 1–18.

Wang R. Q., Qiu J. S., Wen D. J. and Xu H., 2021, The role of hydrous mantle-derived magmas in the generation of Late Cretaceous granitoids in the Gangdese batholith: insights from the Shanba and Zongga plutons in the southern Lhasa subterrane, Tibet. Mineraology and Petrology, **115**, 113–136.

Watson E. B., 1996, Dissolution, growth and survival of zircons during crustal fusion: kinetic principles, geological models and implications for isotopic inheritance. In The Third Hutton Symposium on the Origin of Granites and Related Rocks (eds. M. Brown, P. A. Candela, D. L. Peck, W. E. Stephens, R. J. Walker, and E. Zen). Geological Society of America. pp. 43–56. Available at: https://doi.org/10.1130/0-8137-2315-9.43.

Watson E. B. and Harrison T. M., 1983, Zircon saturation revisited: temperature and composition effects in a variety of crustal magma types. Earth and Planetary Science Letters **64**, 295–304.

Watson E. B. and Harrison T. M., 2005, Zircon Thermometer Reveals Minimum Melting Conditions on Earliest Earth. Science, **308**, 841–844. Available at: https://doi.org/10.,126/science.1110873.

Whitehouse M. J. and Platt J. P., 2003, Dating high-grade metamorphism - Constraints from rare-earth elements in zircon and garnet. Contributions to Mineralogy and Petrology, **145**, 61–74.

Wu T., Zhang W. and Wilde S. A., 2020, The origin of mafic microgranular enclaves in granitoids: Insights from in situ Sr isotope of plagioclases and Zr-Hf isotopes of zircons. Chemical Geology, **551**, 119776. Available at: https://doi.org/10.1016/j.chemgeo.2020.119776.

Xia X. P., Meng J., Ma L., Spencer C. J., Cui Z., Zhang W. F., Yang Q. and Zhang L., 2021, Tracing magma water evolution by H2O-in-zircon: A case study in the Gangdese batholith in Tibet. Lithos, **404**–**405**, 106445. Available at: https://doi.org/10.1016/j.lithos.2021.106445.

Xu W. C., Zhang H. F., Luo B. ji, Guo L. and Yang H., 2015, Adakite-like geochemical signature produced by amphibole-dominated fractionation of arc magmas: An example from the Late Cretaceous magmatism in Gangdese belt, south Tibet. Lithos, **232**, 197–210. Available at: http://dx.doi.org/10.1016/j.lithos.2015.07.001.

Young E. D., Manning C. E., Schauble E. A., Shahar A., Macris C. A., Lazar C. and Jordan M., 2015, High-temperature equilibrium isotope fractionation of non-traditional stable isotopes: Experiments, theory, and applications. Chemical Geology, **395**, 176–195.

Zen E. A., 1986, Aluminum enrichment in silicate melts by fractional crystallization: Some mineralogic and petrographic constraints. Journal of Petrology, **27**, 1095–1117.

Zhang W., Wang Z., Moynier F., Inglis E., Tian S., Li M., Liu Y. and Hu Z., 2019, Determination of Zr isotopic ratios in zircons using laser-ablation multiple-collector inductively coupled-plasma mass-spectrometry. Journal of Analytical Mass Spectrometry, **34**, 1800–1809.

Chapter 4: Reevaluating the Ti-in-quartz thermobarometer

4.1 Introduction and background

The advent of plate tectonic theory (e.g.,Wilson, 1963) presented geologists with a dynamic model that predicts complex pressure-temperature-time (P-T-t) evolution of mountain belts. Essentially simultaneously, petrologists were exploiting phase equilibria to create mineral assemblage thermobarometers (e.g., Davis and Boyd, 1966) with which to investigate natural P-T variations in rocks, although it wasn't until the early 1980s (e.g., Spear and Selverstone, 1983) that dynamic P-T-t histories began to reveal the evolutionary paths predicted by plate tectonic theory. A generation later, advances in *in situ* trace element analysis led to the development of trace element thermobarometers (e.g., Watson and Harrison, 2005). This approach uses quantifiable trace element substitutions into mineral lattices at specific pressures and temperatures. Using experimental run products together with natural samples with well-constrained histories have allowed for the calibration of several accurate and precise trace element thermometers and barometers (Zack et al., 2004; Watson and Harrison, 2005; Wark and Watson, 2006; Watson et al., 2006; Ostapenko et al., 2007; Tomkins et al., 2007; Ferry and Watson, 2007; Hayden et al., 2008; Thomas et al., 2010; Huang and Audétat, 2012; Thomas et al., 2015).

The use of Ti-in-quartz to estimate temperature and pressure is one of the most widely used trace-element-based thermobarometers in the geosciences. Quartz typically presents as large crystals relative to, say, accessory minerals, and is widely present in crustal rocks. Numerous studies from several groups have attempted to quantify the solubility of Ti in quartz resulting in a wide range of estimates; there is yet no universally accepted thermobarometric calibration (e.g., Wark and Watson, 2006; Thomas et al., 2010; Huang and Audétat, 2012; Osborne et al., 2022). Below, I

discuss the challenges associated with Ti-in-quartz, offer potential solutions, and present new experimental results which support the Osborne et al. (2022) calibration.

4.1.1 Previous studies

Wark and Watson (2006) and Thomas et al. (2010) reported Ti concentrations in quartz synthesized in 13 (10 kbar, 600-1000^{o}C) and 19 experiments (5-20 kbar; 725-940^{o}C), respectively. They found a temperature effect on Ti^{4+} substitution into the quartz lattice. Thomas et al. (2010) confirmed that Ti^{4+} substitutes for Si^{4+} on four-fold tetrahedral sites in quartz using XANES. However, Huang and Audétat (2012) performed experiments between 1 and 10 kbar at 600 and 800^{o}C with a small thermal and chemical gradient and found Ti values three times lower than previous calibrations. Due to this chemical gradient, a_{TiO_2} was not constant throughout the experiment meaning that these experiments should not be used as a basis to formulate a thermobarometer (Thomas et al., 2015). Later, Thomas et al. (2015) performed four more experiments confirming the Thomas et al. (2010) calibration.

Acosta et al. (2020) performed several Ti solubility in quartz experiments at 800 ºC and 1 kbar and found a wide range of Ti concentrations in quartz. To understand the reason for these large variations, they developed a kinetic model that suggested that supersaturation had produced very high apparent Ti concentrations in many of their experiments and those of Wark and Watson (2006) and Thomas et al. (2010, 2015). Zhang et al. (2020) undertook similar experiments on aluminosilicate melts from 0.5-4 kbar and 700-900 ºC and found lower Ti concentrations than the prior two studies. Osborne et al. (2022) argued that the Zhang et al. (2020) crystals were grown under rutile undersaturated conditions. Zhang et al. (2020) found concentrations in their ~4 kbars runs that were equivalent to the 8-10 kbar experiments of Thomas et al. (2010, 2015). Subsequently, Osborne et al. (2022) performed experiments using similar methods to Thomas et

al. (2010) and argued that their experiments and those of earlier studies (i.e., Wark and Watson, 2006; Thomas et al., 2010, 2015) were undertaken at chemical equilibrium. They argued that the exponent in Zhang et al.'s (2020) solubility model was incorrectly determined and that the concentration isopleths could have a range of forms.

4.2 Thermodynamics of Ti substitution in the quartz lattice

Previous studies examined the solubility of trace elements in the lattices of quartz, rutile, and zircon (Zack et al., 2004; Wark and Watson, 2006; Watson et al., 2006; Tomkins et al., 2007; Ferry and Watson, 2007; Thomas et al., 2010; Huang and Audétat, 2012; Thomas et al., 2015).

The exchange of Ti^{4+} between rutile and quartz

$$TiO_2{}^{rutile} \Leftrightarrow TiO_2^{quartz} \tag{4.1}$$

leads to an equilibrium constant of:

$$K_1 = \frac{a_{TiO_2}^{quartz}}{a_{TiO_2}^{rutile}} \tag{4.2}$$

At equilibrium,

$$\Delta\bar{H}_1^0 - T\Delta\bar{S}_1^0 + P\Delta\bar{V}_1^0 - RTln\, a_{TiO_2}^{rutile} + RTln\, a_{TiO_2}^{quartz} = 0, \tag{4.3}$$

where $\bar{H}_1^0$ is standard state enthalpy, T is temperature, $\bar{S}_1^0$ is standard state entropy, $\Delta\bar{V}_1^0$ is the change in volume, R is the gas constant, $a_{TiO_2}^{rutile}$ is the activity of TiO_2 in rutile, and $a_{TiO_2}^{quartz}$ is the activity of TiO_2 in quartz. If, as in the case of this study, co-crystallization of rutile and quartz occurs (i.e. both rutile and quartz are present in experiments and show textures of equilibrium formation), then we assume $a_{TiO_2}^{rutile} = 1$ and $K_1 = a_{TiO_2}^{quartz}$. We also assume that studied rutile is pure TiO_2. For Henry's law behavior, $a_{TiO_2}^{quartz} \approx k_1 X_{TiO_2}^{quartz}$; k_1 is the product of Henry's law constant and a conversion factor between X_{TiO_2} and the Ti concentration in quartz. Therefore,

$$\bar{H}_1^0 - T\Delta\bar{S}_1^0 + P\Delta\bar{V}_1^0 + RTln\ k_1 X_{TiO_2}^{quartz} = 0 \quad (4.4)$$

In order to determine the composition Ti in quartz, we use the following equation:

$$lnX_{TiO_2}^{quartz} = \frac{-\Delta\bar{H}_1^0 + T\Delta\bar{S}_1^0 - P\Delta\bar{V}_1^0 - RTln\ k_1}{RT} \quad (4.5)$$

4.3 Methods

4.3.1 Experiments: To reassess the potential impacts of various controls on Ti solubility in quartz, six experiments were undertaken in which coexisting quartz, rutile, and zircon are crystallized from a silicate melt using a using a piston-cylinder apparatus. The SiO_2 starting materials were mostly silica glass with some tridymite found via XRD (same material as discussed in Trail et al., 2019), and the TiO_2 was rutile powder. All starting materials were purchased from Alfa Aesar. Details of the experimental capsule design can be found in Trail et al. (2019). All run products have quartz, rutile, and zircon. Care was taken to ensure equilibrium growth of the run products. Specifically, experiments were run for >100 hours. Experiments were undertaken in the ZrO_2-SiO_2-TiO_2-H_2O-F-Cl system at the University of Rochester. 10 kbar experiments at 900 and 1000 ºC in Pt and Ag capsules, respectively, were performed using an end-loaded piston cylinder apparatus. Following the procedure of Trail et al. (2009), capsules were pressure sealed. Samples were heated to their target temperature in ~5 minutes at a ramp rate of 200 K per minute. They were then left at that temperature for the duration of the experiment and the temperature was monitored using a calibrated thermocouple. Experiments were quenched by cutting power to the transformer.

Polished sections of the run products were examined petrographically and analyzed using the CAMECA ims1290 ion microprobe at UCLA by comparison with calibrated standards including 4 matrix-matched glass standards and 9 experimentally grown quartz samples, details of which

were originally published in Thomas et al. (2010, 2015). We then compared our results with the data of Wark and Watson (2006), Thomas et al. (2010), Thomas et al. (2015), and Osborne et al. (2022). Table S1 shows a list of mounts measured in each analysis session.

4.3.2 Characterization and measurements: Experimental run products are mounted in epoxy and polished using 1 μmAl_2O_3, colloidal silica, and diamond polish. They were then characterized by backscatter electron imaging (BSE) on the Tescan Vega-3 XMU variable-pressure (VP) Scanning Electron Microscope (SEM) with the EDAX energy-dispersive X-ray analysis (EDS) system at UCLA. Each epoxy disk normally contains a few rutile and quartz which are greater than several tens of μm's in size and many smaller zircons. Figure 1 shows a BSE image of six of the experimental run products. Using the *ims*1290 with the Hyperion II source at UCLA, we precisely and accurately measure Ti concentrations in quartz. The Hyperion II source allows for high spatial resolution and allows for several analyses on each quartz grain (Liu et al., 2018).

Standards for each of the three analytical sessions are measured at least 3 times with most measured at least 5 times. Each analysis has 15-20 cycles. We measured $^{30}Si^{16}O$ for all sessions, ^{49}Ti for the 2018 and 2022 sessions, and ^{47}Ti for the 2017 session ($^{30}Si^{16}O$ was the reference mass). In the 2017 session, we also measured 45.8 (as a dummy mass, $^{30}Si^{16}O$ reference mass), 70 (dummy mass, $^{30}Si_3$ reference mass), ^{90}Zr ($^{30}Si_3$ as reference mass), and $^{30}Si_3$. All masses for the 2017 sessions were measured on an electron multiplier (EM). We measured 20 blocks using a mass resolving power (MRP) of ~6000, a field aperture of ~5000 μm, a 30 second presputter, and an O^- beam. In the 2018 session, we measured 45.8 (as a dummy mass) in addition to $^{30}Si^{16}O$ and ^{49}Ti and we used a reference mass of $^{30}Si^{16}O$. We measured 20 blocks with an MRP of ~7000, a field aperture of ~5000 μm width, an O^- primary beam, and a 45 second presputter. In the 2022 session, we used a 2 μm raster, measured 15 cycles, used an EM for all analyses (Detector: $^{30}Si^{16}O$ - EM;

^{49}Ti - H2), an MRP of ~6500, a field aperture of ~2000 μm, an O^{2-} primary beam, and a 45 second presputter.

Calibration between measured $^{4x}Ti/^{28}Si^{16}O$ ratios standards of known concentrations were computed via a weighted regression (New York regression; Mahon, 1996). Standards include glasses with concentrations of 0 ppm Ti, 100 ppm Ti, 500 ppm Ti, and 1000 ppm Ti (Gallagher and Bromiley, 2013) and several QTiP mounts (see Thomas et al., 2010, 2015). As most of our new run products were measured in the February 2022 session, we compare all to that session with a few exceptions. For the handful of samples which we did not measure during the 2022 session, we performed regressions with standards in the relevant session and compared them to values from the 2022 session. Over the course of three sessions, we obtained results from 15 different experimental run products and four matrix-matched glasses. Of the 15, concentrations of quartz from 6 new experimental mounts are reported here and re-analyzed data from several QTiP mounts (i.e., Thomas et al., 2010, 2015) are also given (QTiP 7, 10, 11, 14, 17, 29, 38, 39, 43) (Table 2).

Four Ti-in-quartz standards are measured in all three of our sessions: QTiP7, QTiP14, QTiP38, and QTiP39. These samples range, according to Thomas et al. (2010) and Osborne et al. (2022), from 18 ppm to 813 ppm, making them an appropriate standard for comparison across multiple sessions. However, since we are assessing whether disequilibrium occurred during the growth of the QTiP experiments, these materials cannot be used as geochemical standards. For this reason, we use matrix-matched glasses as a reference. We did not, however, measure the matrix-matched glasses during one of our sessions (2017). For this analysis session, we use measurements of experiments QTiP7, QTiP38, and QTiP39 as standards. To calculate values from the September 2017 session we performed a linear regression between concentrations of three experimental products from the February 2022 session and measurements of the same experimental products

from the 2017 session. Concentrations and temperatures for each experiment were then plotted and a regression for each pressure between the log of concentration and 10^4/T(K) was performed. We then compared these new regressions for each pressure (using only run products we measured ourselves) to that of Osborne et al. (2022). Errors were added in quadrature.

Ti concentrations for all studies were calculated using a modified version of eq. 4 in Osborne et al. (2022) as

$$lnX_{TiO2}^{quartz} = \frac{a+(P\times c+(d*P)+RTlna_{TiO2}^{rutile}}{RT} \quad (4.6)$$

where P is pressure (kbar), T is temperature (K), R is the gas constant (8.3145 J/K-mol), a_{TiO2}^{rutile} is activity of TiO_2 in the fluid or melt, and X_{TiO2}^{quartz} is the mole fraction of TiO_2 in quartz with respect to rutile. Using the suggested values of Osborne et al. (2022), which consider a decreasing volume of the quartz lattice with increasing pressure, the variables a, c, and d are 55.287±0.693, 0, -2.625±0.940, and 0.0403±0.0028, respectively.

4.3.3 Calculation of Ti concentration variability in a slowly cooled system

In order to understand the distribution of Ti-in-quartz in a slowly cooled system, we calculated Ti-in-quartz crystallization temperatures using the equations from Thomas et al. (2010) for a system which cooled from 800 ºC to 25 ºC over two hours and decompressed from 1 kbar to 1 bar over 15 minutes. We assume that full crystallization has occurred in the first 100 ºC.

4.3.4. Choice of glass standard concentrations

We used matrix-matched glasses provided by The University of Edinburgh NERC Ion-Microprobe (SIMS) Facility. These glasses are labeled 0ppm, 100ppm, 500ppm, and 1000ppm. These were later analyzed by several labs: ASU (SIMS: all but 1000 ppm), University of Edinburgh (SIMS,

ICE OES, and EPMA), University of Michigan (EPMA), and University of Bristol (EPMA). Results were generally consistent. In the ICE OES data, the 0ppm sample yielded a negative value due to the concentration being below the detection limit. The SIMS data from Edinburgh is ~1/3 lower than the target concentration for all compositions and the EPMA data from Edinburgh results also report a negative average for the 0 ppm glass. While the ASU data is consistent with most other labs, it does not include data for the 1000 ppm glass. For consistency, we have elected to use concentrations from the same lab for all glasses. Both the University of Michigan and the University of Bristol performed measurements using EPMA. For consistency and simplicity, the University of Michigan EPMA data were used to calculate standard concentrations, but we note that other datasets could lead to small systematic offsets.

4.4 Results

All experimental details including P-T-t conditions are given in Table 1 and measured concentrations are in Table 2. Figure 2 shows results of our new experiments and re-analyzed experiments along with those of previous studies. To correct for the lack of analysis of matrix-matched glass standards in the 2017 session, unweighted linear regressions between QTiP 7, 38, and 39 concentrations from different sessions were determined. Figure 2 shows log(ppm Ti-in-quartz) and 10^4/T(K) plotted for each pressure. Figure 3 shows a comparison of samples which were measured in at least two sessions, and Figure 4 shows a comparison of our recalculated values with the compilation in Osborne et al. (2022). Figure 5 shows the range of Ti concentrations in quartz for a slowly cooled and depressurized system, and Figure 6 shows a comparison of the Thomas et al. (2010) and Osborne et al. (2022) calibrations and linear regressions between log (Ti concentrations) and 10^4/T (K), for three pressure regimes.

4.5 Discussion

4.5.1 Disequilibrium

Recently, the accuracy of the Ti-in-quartz thermobarometer has been called into question in several studies (Acosta et al., 2020; Huang and Audétat, 2012; Zhang et al., 2020). These studies argued that quartz in Wark and Watson (2006) and Thomas et al. (2010) was grown in disequilibrium. If true, published Ti concentrations of quartz in these studies may be spuriously higher than the thermodynamically correct value, potentially resulting in faulty inferences drawn in several hundred studies that have used this thermobarometer. Thomas et al. (2015) argued that their results were not obtained under disequilibrium conditions because of the relative compositional homogeneity of their samples. Acosta et al. (2020) used models showing the combination of high rutile oversaturation, rutile solubility dependence on SiO_2, and quartz supersaturation to argue that the Wark and Watson (2006) and Thomas et al. (2010, 2015) profiles indicate disequilibrium. Acosta et al. (2020) illustrated several potential causes of variation in Ti concentrations in quartz, including rutile and quartz over- and undersaturation, rate constants, and different partition coefficients between quartz and melt.

4.5.1.1 Ti solubility in melt

Acosta et al. (2020) based their argument on the solubility measurements performed by Mysen (2019). These experiments were performed using a hydrothermal anvil device at a range of pressures and temperatures for four compositions: H_2O-TiO_2, TiO_2-SiO_2-H_2O, TiO_2-($CaO{\cdot}5SiO_2$)-H_2O, and TiO_2-($Na_2O{\cdot}5SiO_2$)-H_2O. Mysen (2019) performed each measurement at a different temperature and pressure resulting in the impacts of pressure and temperature not being individually constrained. Antignano and Manning (2008) performed piston cylinder experiments for several fluid compositions, including those systems both with and without SiO_2. While only two of their experiments were performed in a system with SiO_2, TiO_2, and H_2O, the Ti

concentrations of those two experiments are within error of the concentrations measured in the systems with H_2O and TiO_2. From this, they argued that the addition of SiO_2 did not result in measurable change in Ti solubility (Antignano and Manning, 2008). For this reason, we use the thermodynamic relationship that Antignano and Manning (2008) between TiO_2+H_2O and Ti solubility in melt to understand our system of interest.

Seven out of ten of the Antignano and Manning (2008) Ti solubility experiments in the H_2O-TiO_2 system and both in the TiO_2-H_2O-SiO_2 system were performed at 10 kbar. The other three runs were at 2 kbar, 15 kbar, and 7 kbar. The Mysen (2019) data range in pressure from ~5 kbar to ~18 kbar, generally with increasing pressures with increasing temperatures. Considering that we are reassessing Ti-in-quartz as a both an indicator of pressure and temperature, ideally the solubility models we use should also consider pressure, temperature, and composition in their calculations. Antignano and Manning (2008) found a slight pressure dependence on Ti solubility with higher Ti solubility at higher pressures. While the Antignano and Manning (2008) and Mysen (2019) solubility results for TiO_2-H_2O are similar, the Mysen (2019) data shows a sudden increase in Ti solubility in the TiO_2-SiO_2-H_2O system at ~750°C. Since Antignano and Manning (2008) accounted for pressure in their solubility calculations, we will proceed with their calibration.

4.5.1.3 Quartz and rutile supersaturation

Acosta et al. (2020) also argued that differences in the starting materials result in differences in the measured Ti solubility. The activities of SiO_2 and TiO_2 are referenced to quartz and rutile, respectively, in most previous studies (Thomas et al., 2010, Thomas et al., 2015, Acosta et al., 2020, Zhang et al., 2020). Both α-quartz and rutile are the most stable forms of their respective chemical constituents at room pressure and temperature. However, the starting compositions often include metastable phases such as tridymite (Acosta et al., 2020) and silica glass (Thomas et al.,

2010, Huang and Audétat 2012, Thomas et al., 2015, Acosta et al., 2020, Osborne et al., 2022, this study) for the SiO_2 starting phase, or anatase (Thomas et al., 2010, Huang and Audétat 2012, Thomas et al., 2015, Acosta et al., 2020, Osborne et al., 2022) for the TiO_2 starting phase. Because of these phases being metastable, they are more soluble than quartz or rutile in the fluid. Acosta et al. (2020) argues that including metastable phases results in the experimental melt becoming supersaturated with respect to both rutile and quartz at the beginning of the experiment.

Since the supersaturation calculation performed by Acosta et al. (2020) is based on the Mysen (2019) data in which pressure was not considered, we re-evaluate this relationship using the solubility estimates of Antignano and Manning (2008). As stated earlier, Antignano and Manning (2008) found that adding SiO_2 to their TiO_2+H_2O system did not impact Ti solubility in the fluid. Therefore, eq. 10 in Acosta et al. (2020), which relates the supersaturation of quartz and the solubility of rutile in melt, would yield no increase in the solubility of rutile in the fluid with quartz supersaturation. While quartz supersaturation may have occurred, it cannot be determined using this relationship. Independent of this, we know the starting composition of at least some of experiments was silica glass which has a higher solubility than quartz. Therefore, while the relationship described in Acosta et al. (2020) is problematic, we acknowledge the higher initial SiO_2 activities in silica glass compared to α-quartz and the resulting supersaturation of silica with respect to quartz in the melt. Regardless, a smaller supersaturation of silica in melt would result in a smaller range of Ti-in-quartz values (Acosta et al., 2020).

In addition, the proposed supersaturation starting values in Acosta et al. (2020) for rutile appear far too high. Anatase, when referenced to rutile, has a higher Ti activity in a water solution (Kalyani et al., 2015). Acosta et al. (2020) extrapolated data from Kalyani et al. (2015) to determine the solubility difference of Ti between rutile and anatase. However, the Kalyani et al. (2015) data

only extend to ~350 °C, ~250 °C less than our lowest temperature of interest and the experiment was performed at 1 bar. At 350 ºC, the anatase solubility of Ti in water is ~4 times greater than rutile solubility of Ti resulting in Acosta et al. (2020) using this difference in Ti solubilities as the maximum amount of rutile supersaturation in their melt. However, the ratio of solubility between rutile and anatase seems to decrease with increasing temperature. While no data exists showing the difference in Ti solubility between rutile and anatase at high temperatures and pressures, we doubt it would result in supersaturation by a factor of 4.

Interestingly, there does not seem to be a difference in the Ti-in-quartz concentrations whether the starting material is anatase or rutile in the Acosta et al. (2020) study, and the lack of control of the initial Ti host on the final Ti solubility in quartz was confirmed by Osborne et al. (2022) who performed various experiments with different starting materials and found no difference in resultant Ti concentrations in quartz. Further confirmation was provided by Rugaber (2020) who performed experiments with three starting compositions, brookite, rutile, and anatase at 800 °C and 10 kbar and found that the starting composition has no impact on Ti concentrations in quartz.

According to the Acosta et al. (2020) models, a lower supersaturation of both quartz and rutile should result in large differences in the Ti-in-quartz profiles for each grain. However, as discussed by Thomas et al. (2015) and Osborne et al. (2022), the profiles are remarkably similar for most grains suggesting a confounding variable in the Acosta et al. (2020) model. While there is some compositional heterogeneity seen in the Thomas et al. (2010, 2015) and Wark and Watson (2006) results, it is not as much as would be present under both extreme rutile and quartz supersaturation according to the Acosta et al. (2020) models. For this reason, we argue that, with a little modification, the Osborne et al. (2022) calibration yields valid thermobarometric results for quartz.

4.5.2 The impact of cooling on Ti solubility in quartz

In the absence of direct imaging and analysis at pressure and temperature, an infinitely fast quench should allow a "snapshot" of the equilibrium phase assemblage under study. Conversely, slow quenching can result in growth of new phases. If these new phases are then analyzed together with the material produced at peak conditions, incorrect estimates of equilibrium concentrations may occur. As a result, experimental petrologists strive for fast quenches, often on the order or tens of seconds (Thomas et al. 2010). While Acosta et al. (2020) state that their experiments were isobaric and isothermal, this may not be the case due to their slow cooling and decompression. Experiments reported in Acosta et al. (2020) took 15 minutes to reach 1 bar from their experimental pressure of 1 kbar and 2 hours to cool from their target temperature of 800°C to room temperature. This is far slower than the other Ti-in-quartz experiments discussed here (e.g., 20 seconds in Thomas et al. 2010) and may be a reason why Acosta et al. (2020) saw such large variations in their Ti-in-quartz concentrations. Previously, Manning (1994) performed a series of experiments with increasing quench times for the same P-T-x and found a decrease in solubility with greater quench times, thus showing the necessity of fast quench times to get the desired "snapshot" of elemental partitioning.

As shown, slow cooling results in a wide range of Ti concentrations in quartz and will complicate interpretation of the Acosta et al. (2020) experiments. For example, Acosta et al. (2020) noted that small rutile crystals in the outer capsule of their experiment were grown when the activity of TiO_2 was buffered by rutile at ~1 because of the small spaces between the crystals. However, these small crystals, already having access to nucleation sites via the only partially dissolved starting materials, could have grown during the quenching process. From previous experiments, we know that higher temperatures and lower pressures are associated with higher Ti concentrations (Wark and Watson, 2006; Thomas et al., 2010; Huang and Audétat, 2012; Thomas et al., 2015; Zhang et al., 2020; Osborne et al., 2022). These previous calibrations indicate that as quenching progresses,

the immediate growth would result in high Ti concentrations due to lower Ti solubility in melt at lower pressures and elevated temperatures. As the temperature slowly decreases, progressively less Ti partitions into later formed quartz. This could explain in part the wide range of Ti-in-quartz values in the Acosta et al. (2020) run products compared to those of Wark and Watson (2006) and Thomas et al. (2010, 2015).

To determine the impact of slow quenching on Ti-in-quartz values, we calculated the Ti concentrations in quartz that would occur if a samples was monotonically cooled and depressurized from 800 to 25 ºC over 2 hours and from 1 kbar to 1 bar in 15 minutes, respectively (Figure 5). We assume that new material is constantly being introduced adjacent the surface of still growing quartz crystal through advection as cooling occurs, at least at temperatures close to peak values (assuming activities of Ti in rutile and Si in quartz remain close to 1). Although a simplification, we also assume that the entire capsule is at approximately the same temperature and pressure. However, in reality the center of the experimental capsule will be hotter than the outer portion. Previous studies examining Ti solubility in quartz measured growth rates of tens to hundreds of microns per day (Thomas et al., 2010, Huang and Audétat, 2012). But if much of the quartz grown during the Acosta et al. (2020) experiments occurred during quenching, then ~20 μm would need to have grown over the 2 hour quench period (Fig. 6b) resulting in a growth rate of ~10 μm/ hour. While this is much faster than growth rates reported for other Ti-in-quartz run products, hydrothermal quartz has been reported to grow several mm to m per day in pegmatites (Phelps et al., 2020).

4.5.3 Secondary fluorescence

Secondary X-rays (or fluorescence) occur in an aureole surrounding a region being excited into emission of high-energy X-rays, such as under electron bombardment during electron microprobe

analysis (EMPA). This can have deleterious consequences to analysis of geologic materials. Consider the case of an EMPA electron beam being used to analyze a quartz inclusion in a rutile to examine the intrinsic Ti concentration. Despite that physical restriction, X-rays produced in that volume radiate into the enclosing zircon stimulating secondary Ti X-rays there leading to high apparent quartz [Ti]. Ion microprobe analysis, however, is unaffected by this mechanism making it a preferred method of microanalysis in small inclusions. Ti-in-quartz measurements using the Hyperion II source (Liu et al., 2018) used a spot size of ~8 μm. Bell and Kirkpatrick (2022) found that Ti measurements of zircon inclusions within a Ti-rich host can be influenced by the host phase, typically due to surface contamination. However, our analyses of quartz in this study were far from Ti-rich phases and therefore should not be influenced by this effect. Because we were not measuring inclusions in this study, the field aperture was open for these measurements.

Wark and Watson (2006) and Borisova et al. (2018) estimated the length scales over which secondary fluorescence could impact Ti-in-quartz measurements. Borisova et al. (2018) found that the distance between Ti-rich material and an analysis spot needed in order for the concentration to drop to background levels is at least 100 μm. Osborne et al. (2022) performed their measurements at least 50 μm away from rutile which significantly lessens the impact of secondary fluorescence. However, using the Osborne et al. (2022) calibration for ~900°C and 10 kbar, a spot analysis of quartz containing ~300 ppm Ti ~50 μm from a Ti-rich mineral would be overestimated by several hundred ppm Ti. This would result in corresponding over- and underestimate of temperatures and pressure, respectively. To avoid any potential contamination because of secondary fluorescence, analyses need to be a few hundred μm's away from a Ti-rich host. For measurements to be within $1/10^{th}$ of a log unit for a sample that is 300 ppm, analyses should be performed ~110 μm away from a Ti-rich phase (Fig. 2 in Borisova et al., 2018).

The most popular Ti-in-quartz calibrations (Wark and Watson, 2006; Thomas et al., 2010; and Thomas et al., 2015) are all mostly based on EMPA measurements of quartz, with lower concentration samples measured by ion microprobe. Due in part to the popularity of the Ti-in-quartz thermobarometer, the experimental run products grown in these three studies are now often used as geochemical standards for Ti measurements of quartz (e.g., Alexander, 2020). While the ion microprobe analyses are not impacted by secondary fluorescence, we rely on concentrations determined by electron probe from previous studies for our standardization. Thus, if previous studies were affected by secondary fluorescence, then the concentrations we use to standardize our measurements may be artificially high resulting in our own measurements being higher than the true Ti concentration in quartz. Below I investigate whether secondary fluorescence has impacted the integrity of our previous measurements.

To test whether secondary fluorescence is an issue, we consider 1) if secondary fluorescence is a large issue, we would see much larger variations in measurements in the original studies; and 2) a calibration line based only off measurements of matrix matched glasses would result in a shallower calibration curve.

Questioning whether secondary fluorescence impacted the Ti concentration measurements in previous calibrations also allows us to continue investigating potential reasons for the wide distribution in Ti-in-quartz calibrations between published studies. Acosta et al. (2020) performed PFIB (plasma focused ion beam) to remove rutile from the quartz they analyzed whereas Wark and Watson (2006), Thomas et al. (2010, 2015), and Osborne et al. (2019, 2022) did not physically separate the quartz and rutile. If Ti concentration analyses were performed within a few hundred μm of a Ti-rich phase, these analyses may be impacted by secondary fluorescence. If coexisting rutile caused enough secondary fluorescence in the Thomas et al. (2010, 2015) and Osborne et al.

(2022) studies, this could explain the difference in Ti-in-quartz concentrations between the various investigations.

In order to test whether the previously measured concentrations of Ti were potentially impacted by secondary fluorescence, I calculate Ti concentrations in quartz standardizing to only 1) the matrix-matched glasses from Edinburgh, 2) the Ti-in-quartz values from Thomas et al. (2010, 2015), and 3) both (Table 3). In general, I find that while QTiP quartz seem in general to have higher Ti concentration than the matrix matched standards, this difference is not large. For example, QTiP7, 14, 38, and 39 which have 18, 100, 380, and 813 ppm Ti, respectively, according to Thomas et al. (2010), contain 28, 150, 360, and 700 ppm Ti, respectively, when only including matrix-matched glasses in the calibration. We also note that the portion of QTiP14 we have access to appears to have some compositional heterogeneity leading us to believe that the measured QTiP14 value reported here may be higher than the true average composition. Figure 6 shows both the calibration from Osborne et al. (2022) as well as the best fit lines for each pressure regime where we measured at least three experiments. Assuming that the matrix-matched standards have the correct Ti concentrations, and we measured a representative sample of the glass, the reported Ti concentrations in Osborne et al. (2022) are approximately the same as our own measurements. This indicates that secondary fluorescence is not a substantial issue.

4.5.4. Ti-in-quartz calibration

Fig. 6 shows calibrations from Thomas et al. (2010), Osborne et al. (2022), and measured and recalculated values from this study for three pressures: 10 kbar, 15 kbar, and 20 kbar. These three correlations are broadly consistent with the exception of the 20 kbar experiments. This is the pressure where we measured the fewest experimental run products and the pressure with the lowest concentrations. This difference between calibrations may be caused by 1) contamination in our

experiments or an error when we related previous concentrations to our glass-only regression; 2) other studies reported erroneously low Ti concentrations.

Least squares regressions for three pressures, 10 kbar, 15 kbar, and 20 kbar, are included here:

$$\text{10 kbar: } lnX_{TiO_2}^{quartz} = \frac{-7581\ (\pm 2191)}{T(K)} - 1.17\ (\pm 1.87) \quad (4.7)$$

$$\text{15 kbar: } lnX_{TiO_2}^{quartz} = \frac{-10497\ (\pm 1320)}{T(K)} + 0.36\ (\pm 1.17) \quad (4.8)$$

$$\text{20 kbar: } lnX_{TiO_2}^{quartz} = \frac{-9256\ (\pm 4300)}{T(K)} - 1.47\ (\pm 3.77) \quad (4.9).$$

Because of the greater number of samples analyzed by Osborne et al. (2022), we suggest using their calibration for future studies.

4.6. Conclusions

Multiple Ti-in-quartz calibrations have been published with considerable variance seen. In this report, we discuss several potential issues in obtaining an accurate Ti-in-quartz thermobarometric calibration: 1) secondary fluorescence, 2) supersaturation, and 3) quenching rates. Most experiments performed by Wark and Watson (2006), Thomas et al. (2010, 2015), and Osborne et al. (2022) were measured by EMPA. An issue associated with such measurements of Ti phases is the possibility of secondary fluorescence when measuring trace amounts of Ti in a grain that is close to a Ti-dominated phase, such as rutile or titanite. To test if this was a potential issue in previous studies, we remeasured 9 previously published experimental run products and treated them as unknown mounts. We used matrix matched Ti standards from Edinburgh to determine their "new" Ti concentration and present Ti-in-quartz concentrations for 6 new experiments. In general, we find that the QTiP mounts tend to have higher concentrations at similar count rates compared to the matrix-matched glasses. However, on average, samples standardized using

matrix-matched glass are 90% of those calculated using a QTiP-based standardization. We find that the quenching rate in the Acosta et al. (2020) study may be a reason for the wide distribution of Ti concentrations in their run products and discuss different model assumptions. Continued modeling of the many controls on Ti concentrations in quartz are needed both for knowledge of quartz crystallization and understanding of Ti-in-zircon thermobarometry. We conclude that the calibration performed by Osborne et al. (2021) is likely the best thermobarometric model yet available.

4.7 Figures

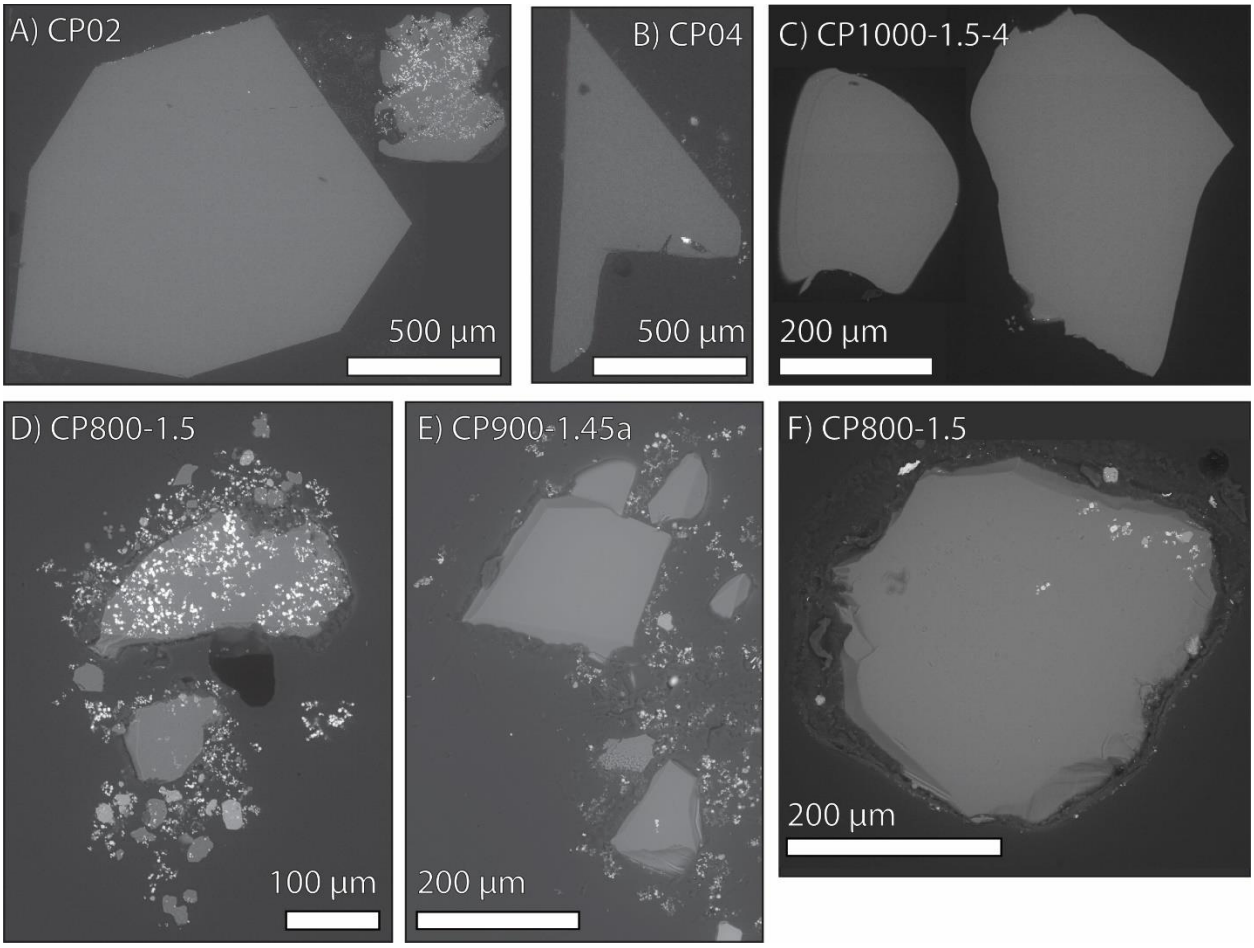

Figure 4.1: Backscatter electron images of 6 of the run products with row 1 showing experiments performed at 10 kbar and row 2 showing those performed at ~15 kbar. Experimental temperature increases from the left to the right. The major phase in all of these images is quartz with some also showing zircon and rutile. The dark background is epoxy.

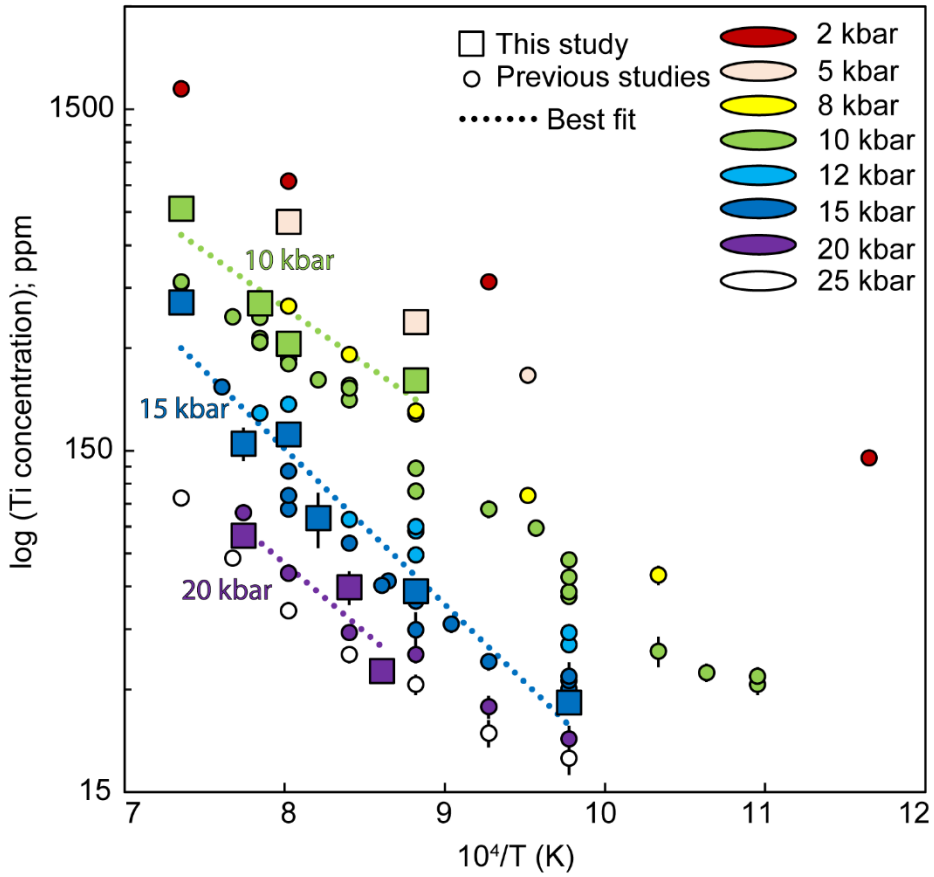

Figure 4.2: Comparison of measured and recalculated Ti concentrations in quartz. The three regression lines show relationships between temperature and concentration for each pressure regime with at least three measurements. Measurements made in this study are in large circles and recalculated concentrations are shown in small circles. The upper right side shows what pressure each color corresponds to. Vertical bars represent 1 s.e.

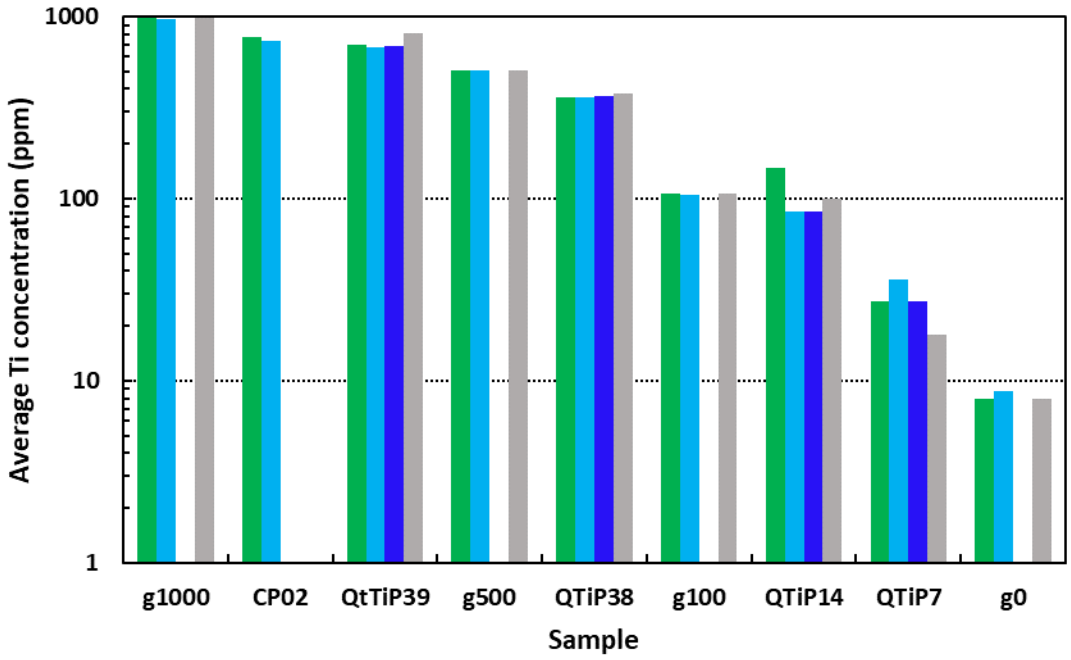

Figure 4.3: Comparison of Ti-in-quartz measurements between multiple sessions based on sample and session. Green, aqua, blue, and grey represent the 2022, 2018, 2017, and previously published concentrations, respectively.

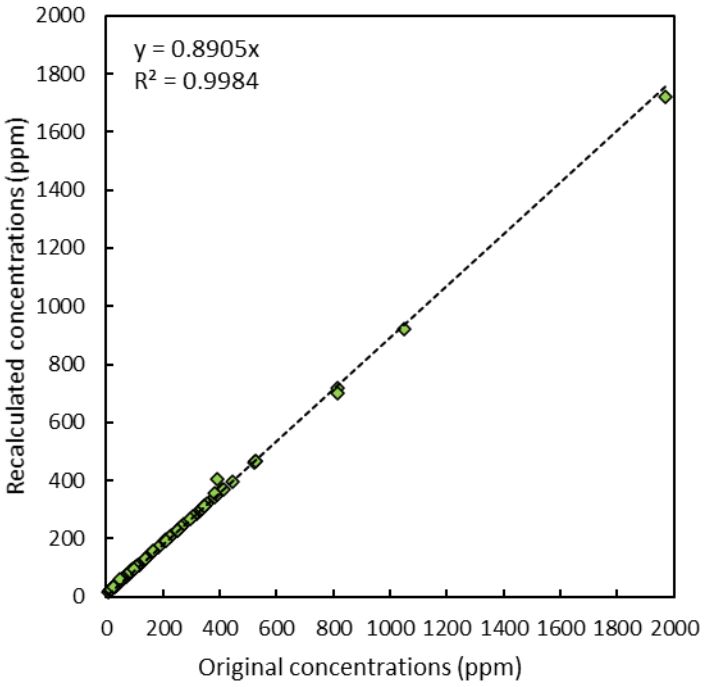

Figure 4.4: Relationship between original concentrations and recalculated concentrations.

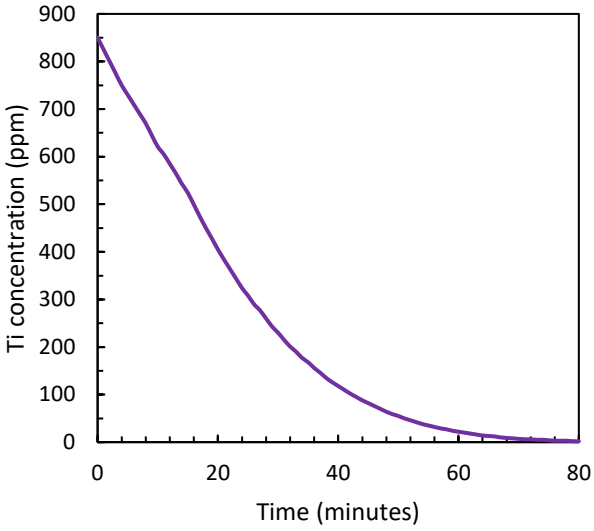

Figure 4.5: Calculated change in concentration with monotonic cooling from 800 °C to 25 °C over 2 hours (first 80 minutes shown) and 1 kbar to 1 bar over 15 minutes. Calculation used the calibration of Thomas et al. (2010). Note the rapid decrease in composition over the course of the first 30 minutes.

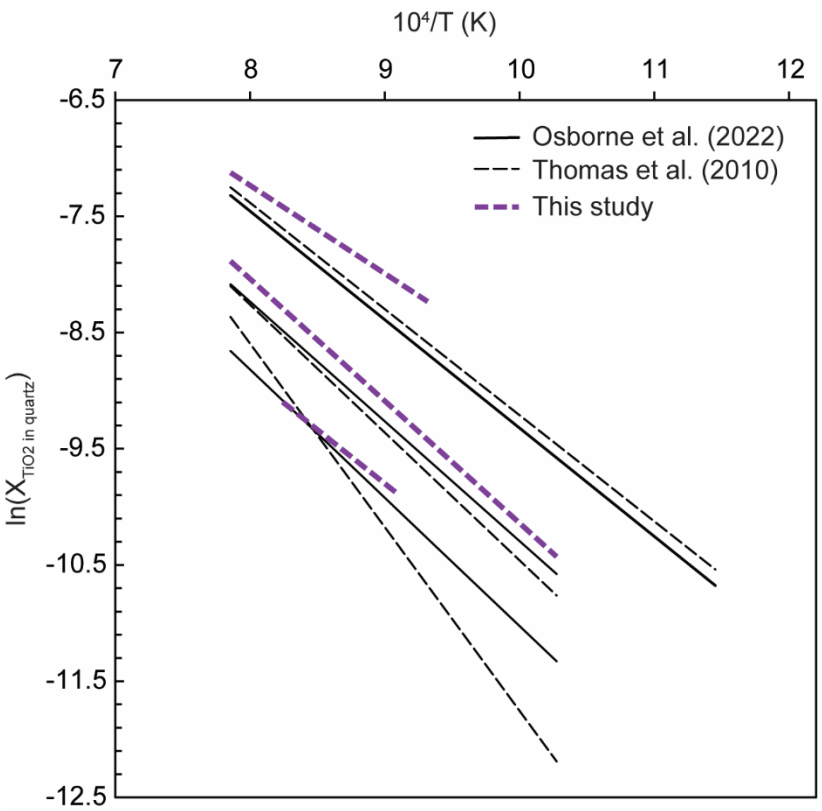

Figure 4.6: Thin lines represent the calibration proposed by Osborne et al. (2022). Thin lines show linear regressions from this study.

4.8 Tables

Pressure (kbar)	Temperature (ºC)	Sample	Duration (hours)
10	800	CP800-1a	432
10	900	CP04	168
10	1000	CP02	70
15	800	CP800-1.5a	400
14.5	900	CP900-1.45a	190
15	1000	CP1000-1.5a-4	72

Table 4.1: List of newly grown experiments with temperature, pressure, name, and run duration.

Session	Sample	Temperature (ºC)	Pressure (kbar)	Ti concentration (ppm)	1 s.e.
2022	*QTiP38*	800	5	358	18
2022	*QTiP39*	900	5	702	25
2022	CP800-1	800	10	241	9
2022	CP02	1000	10	768	36
2022	CP04	900	10	309	11
2018	*QTiP43*	925	10	405	7
2022	CP900-1.45	900	15	167	6
2022	CP1000-1.5-4	1000	15	408	17
2022	CP800-1.5	800	15	58	3
2017	*QTiP10*	940	15	157	18
2017	*QTiP11*	875	15	95	18
2022	*QTiP7*	700	15	27	1
2017	*QTiP14*	940	20	85	3
2017	*QTiP17*	850	20	60	7
2018	*QTiP29*	825	20	34	2
Notes: *Remeasured experiment from Thomas et al. (2010) or Thomas et al. (2015)*					

Table 4.2: Experimental run products used in this calibration with pressure, temperature, Ti concentration, and 1 s.e. of Ti concentrations. Samples in italics are reanalyzed run products from Thomas et al. (2010) or Thomas et al. (2015).

				Published (ppm)		Concentrations (standardized to)			Difference from published (%)			1 s.e. (ppm)		
Session	Sample	Temperature	Pressure (Gpa)	concentration	s.d.	all	glass	QTiP	all	glass	QTiP	all	glass	QTiP
2017	*QTiP38*	800	0.5	380	8			367			-3			**12**
2017	*QTiP39*	900	0.5	813	5			688			-15			**24**
2017	*QTiP7*	700	1.5	18	1			27			52			**2**
2017	*QTiP11*	875	1.5	96	5			**95**			-1			**5**
2017	*QTiP10*	940	1.5	167	5			**157**			-6			**6**
2017	*QTiP17*	850	2	49	2			**60**			22			**3**
2017	*QTiP14*	940	2	100	2			85			-15			**3**
2018	*QTiP38*	800	0.5	380	8	371	357	373	-2	-6	-2	8	**8**	9
2018	*QTiP39*	900	0.5	813	5	711	683	716	-12	-16	-12	12	**13**	13
2018	*QTiP43*	925	1	392	1	422	**405**	424	8	3	8	7	**7**	8
2018	CP02	1000	1			769	738	774				24	**23**	25
2018	*QTiP7*	700	1.5	18	1	36	36	36	100	100	99	4	**4**	5
2018	*QTiP29*	825	2	24	1	34	**34**	34	41	42	40	5	**4**	6
2018	*QTiP14*	940	2	100	2	87	85	87	-13	-15	-13	4	**3**	4
2018	*g1000*			987	10	1011	970	1017	2	-2	3	39	**38**	40
2018	*g500*			504	4	529	508	532	5	1	6	11	**11**	12
2018	*g100*			107	2	108	105	109	1	-1	2	5	**4**	5
2018	*g0*			8	1	8	9	7	-5	11	-10	4	**4**	5
2022	*QTiP38*	800	0.5	380	8	408	**358**	407	7	-6	7	15	**18**	16
2022	*QTiP39*	900	0.5	813	5	802	**702**	812	-1	-14	0	11	**25**	13
2022	CP800-1	800	1			274	**241**	269				4	**9**	6
2022	CP04	900	1			352	**309**	349				6	**11**	8
2022	CP02	1000	1			877	**768**	889				29	**36**	30
2022	*QTiP7*	700	1.5	18	1	29	**27**	18	61	53	-2	2	**1**	4
2022	CP800-1.5	800	1.5			64	**58**	54				3	**3**	5
2022	CP900-1.45	900	1.45			189	**167**	182				4	**6**	5
2022	CP1000-1.5-4	1000	1.5			465	**408**	466				12	**17**	13
2022	*QTiP14*	940	2	100	2	168	**148**	160	68	48	60	49	**43**	50
2022	*g1000*			987	10	1125	**984**	1143	14	0	16	39	**46**	40
2022	*g500*			504	4	578	**507**	582	15	1	16	27	**29**	28
2022	*g100*			107	2	120	**107**	111	12	0	4	5	**6**	6
2022	*g0*			8	1	7	**8**	-5	-17	0	-167	1	**1**	4

italics: reanalyzed sample

purple: served as standard for that session

*Textures indicating disequilibrium growth present

Bold: indicates measurements used in Figure 1

Table 4.3: Calculations of Ti concentrations in experimental run products using a glass-only calibration, QTiP-only calibration, and a calibration with both glass and QTiP standards.

4.9 References

Acosta, M. D., Watkins, J. M., Reed, M. H., Donovan, J. J., and DePaolo, D. J., 2020, Ti-in-quartz: Evaluating the role of kinetics in high temperature crystal growth experiments. Geochimica et Cosmochimica Acta, 281, 149–167. https://doi.org/10.1016/j.gca.2020.04.030

Alexander, E., 2020, Geochemical tracers of crustal thickness and their applicability to the Tibetan-Himalayan Orogen. Ph.D thesis, University of California, Los Angeles, pp. 144.

Antignano, A., and Manning, C. E., 2008, Rutile solubility in H2O, H2O-SiO2, and H2O-NaAlSi3O8 fluids at 0.7-2.0 GPa and 700-1000 °C: Implications for mobility of nominally insoluble elements. Chemical Geology, 255, 1–2, 283–293. https://doi.org/10.1016/j.chemgeo.2008.07.001

Bell, E.A., and Kirkpatrick, H.M., 2022, Micro-zircon inclusions in accessory minerals reveal more complete magma compositional evolution records. Submitted to Contributions to Mineralogy and Petrology.

Borisova, A. Y., Zagrtdenov, N. R., Toplis, M. J., Donovan, J. J., Llovet, X., Asimow, P. D., de Parseval, P., and Gouy, S., 2018, Secondary fluorescence effects in microbeam analysis and their impacts on geospeedometry and geothermometry. Chemical Geology, 490, 22–29. https://doi.org/10.1016/j.chemgeo.2018.05.010

Davis, B.T.C. and Boyd, F.R., 1966, The join Mg2Si2O6-CaMgSi2O6 at 30 kilobars pressure and its application to pyroxenes from kimberlites. Journal of Geophysical Research, 71, 3567-3576.

Ferry, J. M., and Watson, E. B., 2007, New thermodynamic models and revised calibrations for the Ti-in-zircon and Zr-in-rutile thermometers. Contributions to Mineralogy and Petrology, 154, 4, 429–437. https://doi.org/10.1007/s00410-007-0201-0

Gallagher, C., and Bromiley, G., 2013, Ti in quartz standards.

Huang, R., and Audétat, A., 2012, The titanium-in-quartz , TitaniQ thermobarometer: A critical examination and re-calibration. Geochimica et Cosmochimica Acta, 84, 75–89. https://doi.org/10.1016/j.gca.2012.01.009

Kalyani, V., Vasile, B. S., Ianculescu, A., Testino, A., Carino, A., Buscaglia, M. T., Buscaglia, V., and Nanni, P., 2015, Hydrothermal Synthesis of SrTiO3: Role of Interfaces. Crystal Growth and Design, 15, 12, 5712–5725. https://doi.org/10.1021/acs.cgd.5b00770

Liu, M. C., McKeegan, K. D., Harrison, T. M., Jarzebinski, G., and Vltava, L., 2018, The Hyperion-II radio-frequency oxygen ion source on the UCLA ims1290 ion microprobe: Beam characterization and applications in geochemistry and cosmochemistry. International Journal of Mass Spectrometry, 424, 1–9. https://doi.org/10.1016/j.ijms.2017.11.007

Mahon, K. I., 1996, The New “York” Regression: Application of an Improved Statistical Method to Geochemistry. International Geology Review, 38, 293–303. https://doi.org/10.1080/00206819709465336

Manning, C. E., 1994, The solubility of quartz in HZ0 in the lower crust and upper mantle. In Geochimica et Cosmochimica Acta , Vol. 58, Issue 22,

Mysen, B., 2019, Aqueous fluids as transport medium at high pressure and temperature: Ti4+ solubility, solution mechanisms, and fluid composition. Chemical Geology, 505, 57–65. https://doi.org/10.1016/j.chemgeo.2018.12.007

Osborne, Z. R., Thomas, J. B., Nachlas, W. O., Angel, R. J., Hoff, C. M., and Watson, E. B., 2022, TitaniQ revisited: expanded and improved Ti-in-quartz solubility model for thermobarometry. Contributions to Mineralogy and Petrology, 177, 3, https://doi.org/10.1007/s00410-022-01896-8

Ostapenko, G. T., Tarashchan, A. N., and Mitsyuk, B. M., 2007, Rutile-quartz geothermobarometer. Geochemistry International, 45, 5, 506–508.

Phelps, P.R., Lee, CT.A. and Morton, D.M., 2020, Episodes of fast crystal growth in pegmatites. Nature Communications, 11, 4986. https://doi.org/10.1038/s41467-020-18806-w

Rugaber, C., 2020, Experimental Investigation of Ti Incorporation into Quartz: Implications for thermobarometry in the crust. Undergraduate thesis. University of Rochester, 18 pp.

Spear, F.S. and Selverstone, J., 1983, Quantitative PT paths from zoned minerals: theory and tectonic applications. Contributions to Mineralogy and Petrology, 83, 348-357.

Thomas, J. B., Watson, E. B., Spear, F. S., Shemella, P. T., Nayak, S. K., and Lanzirotti, A., 2010, TitaniQ under pressure: The effect of pressure and temperature on the solubility of Ti in quartz. Contributions to Mineralogy and Petrology, 160, 5, 743–759. https://doi.org/10.1007/s00410-010-0505-3

Thomas, J. B., Watson, E. B., Spear, F. S., and Wark, D. A., 2015, TitaniQ recrystallized: experimental confirmation of the original Ti-in-quartz calibrations. Contributions to Mineralogy and Petrology, 169, 3, https://doi.org/10.1007/s00410-015-1120-0

Tomkins, H. S., Powell, R., and Ellis, D. J., 2007, The pressure dependence of the zirconium-in-rutile thermometer. Journal of Metamorphic Geology, 25, 6, 703–713. https://doi.org/10.1111/j.1525-1314.2007.00724.x

Trail, D., Bindeman, I.N., Watson, E.B., Schmidt, A.K., 2009, Experimental calibration of oxygen fractionation between quartz and zircon. Geochimica et Cosmochimica Acta, 73, 23, 7110-7126.

Trail, D., Savage, P.S., Moynier, F., 2019, Experimentally determined Si isotope fractionation between zircon and quartz. Geochimica et Cosmochimica Acta, 260, 257-274

Wark, D. A., and Watson, E. B., 2006, TitaniQ: A titanium-in-quartz geothermometer. Contributions to Mineralogy and Petrology, 152, 6, 743–754. https://doi.org/10.1007/s00410-006-0132-1

Watson, E. B., and Harrison, T. M., 2005, Zircon Thermometer Reveals Minimum Melting Conditions on Earliest Earth. Science, 308, 841–844. https://doi.org/10.1126/science.1110873

Watson, E. B., Wark, D. A., and Thomas, J. B., 2006, Crystallization thermometers for zircon and rutile. Contributions to Mineralogy and Petrology, 151, 413–433. https://doi.org/10.1007/s00410-006-0068-5

Wilson, J.T., 1963, A possible origin of the Hawaiian Islands. Canadian Journal of Physics, 41, 863-870.

Zack, T., Moraes, R., and Kronz, A., 2004, Temperature dependence of Zr in rutile: Empirical calibration of a rutile thermometer. Contributions to Mineralogy and Petrology, 148, 4, 471–488. https://doi.org/10.1007/s00410-004-0617-8

Zhang, C., Li, X., Almeev, R. R., Horn, I., Behrens, H., and Holtz, F., 2020, Ti-in-quartz thermobarometry and TiO2 solubility in rhyolitic melts: New experiments and parametrization. Earth and Planetary Science Letters, 538. https://doi.org/10.1016/j.epsl.2020.116213

Chapter 5: Summary

5.1. Using models to understand crustal processes

As remarked in Chapter 1, humans have understood their world through history by weaving explanatory narratives. As Earth scientists, we continue this tradition by conceptualizing our observations through largely quantifiable models. The foundational concept of this dissertation is plate tectonics. Tectonic 'damage' in eastern Tibet occurs because of the continuing growth of the Tibetan plateau, itself a manifestation of the Indo-Asian collision (Yin and Harrison, 2000). Zr isotope fractionation in the Peninsular Ranges Batholith is a distant manifestation of subduction of the Farallon plate beneath western North America leading to the great Cordilleran batholiths. Thermobarometry allows geologists to understand the 2D, and in some cases 3D, evolution of tectonic and magmatic processes. Each of these lines of investigation potentially provides a new way to refine the overarching model of plate tectonics and understand how it shapes crustal processes. Described below are a few key points related to crustal processes and our use of models to understand Earth's evolution.

Models should be constantly refined in light of new observations to better understand plate tectonics. Chapter 2 investigated controls on landscape evolution in eastern Tibet in which we found that fault damage within ~15 km of major faults significantly impacted erosion in Eastern Tibet. While erosion coefficients appear not primarily controlled by vegetation, rainfall, and lithology, knowledge of their role is important to develop and improve models. In the context of Chapter 2, we can ask follow-up questions to further build models to understand tectonic damage. Is the 15 km length scale for fault damage a universal observation? If not, is there a relationship between quantifiable metrics and the location of fault damage which would allow us

to understand the role of tectonics and rock strength better? If so, this information could help us not only understand topography better but could also help make policy decisions related to building in mountainous landscapes.

Models are also useful for understanding new petrologic or geochemical systems. Recent studies of non-traditional stable isotopes, such as Zr and Si, have used well-understood geologic localities to gain greater understanding of newly studied stable isotopes. For example, Savage et al. (2011) used Hekla volcano as a case study of Si isotope variability. Later, Inglis et al. (2019) used the same samples to understand whether Zr stable isotopes had similar controls to those of Si isotopes. Chapter 3 followed a similar approach; we chose to study the Peninsular Ranges batholith because the extensive work on Cordillera magmatism previously performed provided us a well-defined natural laboratory in which to examine surprisingly large variations in Zr isotopes.

Because humans are imperfect, so are our models. Chapters 4 and 5 discuss the assumptions and mistakes we make when using models to understand geologic processes. Chapter 4 examines controls on Zr stable isotopes, earlier thought to be a proxy for magmatic evolution. We systematically studied controls on Zr isotopic variations through measurements of various phases coupled with trace element chemistry, modeling, and petrography. We conclude that, counter to what previous studies suggested, Zr stable isotopes cannot, at the present time, be used as unambiguous metrics of magmatic evolution.

Even popular models can and should be reconsidered. Chapter 5 investigated recent skepticism of the widely cited Ti-in-quartz thermobarometric calibration. With new data, old assumptions are questioned, and new insights may be obtained. Experiments undertaken in Chapter 5 are

consistent with the earlier calibrations and arguments developed therein suggest that recent criticisms are unwarranted, seemingly due to experimental and analytical artifacts. With improvements in the Ti-in-quartz thermobarometer and a greater understanding of controls on Ti portioning between melt and quartz, we will be able to determine petrological responses to plate forces more accurately.

5.2 References

Inglis, E.C., Moynier, F., Creech, J., Deng, D., Day, J.M.D., Teng, F.-Z., Bizzarro, M., Jackson, M., and Savage, P., 2019, Isotopic fractionation of zirconium during magmatic differentiation and the stable isotope composition of the silicate Earth. Geochimica Cosmochimica Acta, 250, 311-323. https://doi.org/10.1016/j.gca.2019.02.010

Savage, P.S., Georg, R.S., Williams, H.M., Burton, K.W., Halliday, A.N. (2011). Silicon isotope fractionation during magmatic differentiation Geochimica Cosmochimica Acta, 75, 20, 6124-6139. https://doi.org/10.1016/j.gca.2011.07.043

Appendix A for Chapter 2: Impact of fault damage on eastern Tibet Topography

2.7. Quantification of Erosion Coefficients and Rate Constants

For the analyses in the main text, we quantified erosion coefficient, *K*, from the linear relationship between erosion rate, *E*, and normalized channel steepness calculated from the integral method, k_{sn}. We calculated the root-mean-square-errors (RMSE) to examine the goodness of the fits of linear and nonlinear (exponential or power-law) models between *E* and k_{sn}. RMSE is calculated by taking the square root of the sum of squared errors (SSE) divided by degrees of freedom (*df* = number of data points - number of parameters). RMSE values from linear and nonlinear models are similar between erosion rate and various topographic metrics including channel steepness, slope, and local relief, when looking both at all basins and only small basins with $A < 200$ km^2 (Table S4). Since the linear and nonlinear models produce comparable results, we calculated the erosion coefficient, *K*, assuming a linear model ($n = 1$) without an intercept (eq. 2.3). The use of $n = 1$ is consistent with the approaches of previous studies in this study area (Ouimet et al., 2009; Kirby and Ouimet, 2011, Scherler et al., 2017). To examine the differences, we also calculated erosion coefficient, K_{nl}, assuming the best-fit, nonlinear relationship between erosion rate and channel steepness (power-law model, $E = K_{nl} \cdot k_{sn}^{n}$; $n = 0.49$).

We also examined erosion coefficients calculated based on different assumptions of river incision models or rate constants calculated for different topographic metrics (Table S3). First, we calculated the erosion coefficients, K_{sp} and K_{ss}, using discharge instead of drainage area and determined the expected exponents based on stream power or shear stress incision models, respectively (e.g., Whipple et al., 1999, Finlayson et al., 2002). The erosion rates are related to controls as,

$$\boldsymbol{E = K_i\,(Q^{a_i} S^{b_i})^{n_i}} \qquad (2.5)$$

where E is erosion rate [L t^{-1}], Q is stream discharge [L^3 t^{-1}], S is slope [dimensionless], and a and b are constants that differ depending on stream power ($i = sp$) or shear stress ($i = ss$) based erosion models, and n_i is an empirical constant. For the stream power-based erosion model, a = 1/2 and b = 1. For the shear stress-based erosion model, a = 1/3 and b = 2/3. We calculated the spatial distribution of Q by integrating mean annual precipitation of upstream grid cells assuming infiltration or evapotranspiration are negligible or proportional to precipitation. We acknowledge that this assumption may not be applicable to certain areas. However, due to the lack of a high-resolution discharge dataset, this assumption is necessary to quantify the spatial distribution of Q. Based on relationships between basin-averaged erosion rates and basin-averaged values of discharge as well as slope, we determine n_{sp} and n_{ss}. There are comparable RMSE from nonlinear power-law and linear models (Table S4). Assuming best-fit, power-law exponents of n_{sp} =0.50 and n_{ss} =0.63, we calculated K_{sp} and K_{ss}. Unlike K, erosion coefficients of K_{sp} and K_{ss} are less affected by the spatial variations of precipitation or discharge.

Then, we calculated the rate constants from relationships between basin-averaged erosion rates and topographic metrics of hillslope gradient and local relief. Previous studies have also shown empirical relationships between erosion rate and hillslope gradient or local relief (Montgomery and Brandon, 2002, Portenga and Bierman, 2011). Topographic metrics of both hillslope gradient and local relief have comparable RMSE from nonlinear power-law and linear models (Table S4). Following the previous studies which showed non-linear relationships between erosion rate and hillslope gradient or local relief (Ouimet et al., 2009; Kirby and Ouimet, 2011), we determined the best-fit, nonlinear power-law relationship between erosion rates E and hillslope gradient ($\boldsymbol{E = 0.46 \times S^{1.44}}$; RMSE = 0.108 mm yr^{-1}) and local relief ($E = 6.8\times10^{-5}\times LR^{1.2}$, RMSE = 0.107 mm

yr^{-1}). Using the power-law exponents of n = 1.44 and n = 1.20, we quantified rate constants for hillslope gradient (K_{slp}) and local relief (K_{lr}) for each basin, respectively.

2.7.1. Calculating channel steepness

We calculated basin-averaged k_{sn} by (1) the integral method based on □ (Perron and Royden, 2013; Scherler et al., 2017; Data Repository) and (2) averages of channel steepness extracted from channel points (ie. averages of channel steepness that are calculated as normalized channel slope by drainage area) (Wobus et al., 2006; Ouimet et al., 2009; Kirby and Ouimet, 2011; Scherler et al., 2017). Following Scherler et al. (2017), we used k_{sn} from the integral method to calculate K.

In the integral method, channel steepness k_s [$L^{2\Theta}$] is calculated from the fit between elevation z and χ (Perron and Royden, 2013) as:

$$z(x) = z(x_b) + \left(\frac{k_s}{A_0{}^{\theta}}\right)\chi \qquad (2.6)$$

where $\boldsymbol{\chi} = \int_{x_b}^{x}\left(\frac{A_0}{A(x)}\right)^{\theta}\boldsymbol{dx}$, x is horizontal distance [L], b is the base level, and A_0 is a reference drainage area [L^2; A_0 = 1 km^2]. We calculated normalized channel steepness (k_{sn}) assuming a reference concavity θ of 0.45, which is consistent with previous studies of this area (Ouimet et al., 2009; Kirby and Ouimet, 2011; Scherler et al., 2017). Both the integral method and values obtained from averaging channel points show comparable results to each other (R^2 = 0.97), and are similar to calculations in Scherler et al. (2017). Following Scherler et al. (2017), we used k_{sn} from the integral method based on $\boldsymbol{\chi}$ for calculating erosion coefficients.

2.8 Statistical Analysis

First, we examined how K, K_{nl}, K_{ss}, K_{sp}, K_{slp}, and K_{lr}, vary with potential controls including distance to major faults (D_{mf}), distance to major active faults, mean annual precipitation rates, *NDVI*, and *PGA* (Table S7). We examined five groups including all basins (n = 111), small basins with A < 200 km^2 (n = 95), and small basins dominated by siliciclastic sedimentary rocks (n = 56), mixed composition sedimentary rocks (n = 18), and plutonic rocks (n = 11).

All rate constants (K, K_{nl}, K_{ss}, K_{sp}, K_{slp}, and K_{lr}) show statistically significant (p-value < 0.05), inverse relationships with (1) distance to major faults and (2) distance to major active faults for all basins, small basins, and small basins dominated by siliciclastic sedimentary rocks. This is also true for small basins composed of 100% siliciclastic sedimentary rocks (n = 33). For small basins dominated by mixed composition sedimentary rocks, K shows statistically significant inverse relationships with distance to major faults and distance to major active faults. The K from small basins dominated by plutonic rocks has a stronger positive correlation with precipitation (R = 0.69, p-value = 0.02) than distance to major faults (R = -0.48, p-value = 0.14) and distance to major active faults (R = -0.54, p-value = 0.08). This co-correlation is due to basins in the Daxue Shan (e.g., wbo445, wbo647) that have high K, high precipitation rates, and are close to active faults. It is possible that these basins are affected by both high precipitation rates and pervasive fault damage.

The correlations between erosion coefficients and mean annual precipitation in different basin groups were mostly non-significant (Table S7). All statistically significant correlations with mean precipitation rates were negative and lower than those with the distance to major faults, except for the one positive correlation with K from plutonic rocks explained earlier. The weak, negative correlation between K and mean annual precipitation in all basins or basins dominated by

siliciclastic sedimentary rocks is likely due to the presence of basins in the hinterland that have high *K* and are close to major faults but experience low precipitation rates. None of the rate constants show statistically significant correlations with *NDVI*. There are positive correlations between both K_{nl} and K_{ss} and *PGA*, but these correlations are weaker than those with distance to major faults.

We also perform multiple stepwise regressions to explain *K* using five variables (i.e., distance to major faults, distance to major active faults, *MAP*, *NDVI*, and *PGA*). The linear model based on negative relationships with distance to major active faults and mean annual precipitation rates is the best-fit linear model (F = 8.02, p-value = 0.0055). If we exclude distance to major active faults due to the similarity between D_{mf} and distance to major active faults, the linear model based on negative relationships with the distance to major faults and mean annual precipitation rates is the best-fit linear model (F = 7.96, p-value = 0.0057). These results are consistent with previous analyses which identified individual correlations, which support strong correlations between erosion coefficients and distance to major faults or distance to major active faults among potential controls.

In summary, our analysis shows that distance to faults is an important control on various erosion coefficients. The similar statistical results from active faults and all faults implies that all faults, regardless of whether they are inactive or active, may have an influence on erosion due to accumulated rock damage over time. The weak or statistically insignificant correlations between erosion coefficients and mean annual precipitation rates indicate that the influence of mean annual precipitation rates in these areas is likely secondary, although we cannot completely rule out the potential influence of precipitation rate or variability in this area (Scherler et al., 2017).

Second, we performed *t*-tests to examine whether the mean values of erosion coefficient, *K*, are different for several basin groups divided by distance to major faults or lithologic type. We examined the five basin groups of all basins, small basins, and small basins dominated by siliciclastic sedimentary, mixed composition sedimentary, and plutonic rocks. Our null hypothesis is that erosion coefficients from two groups come from independent random samples with normal distributions, equal means, and unequal and unknown variances. We first examined what ranges of distance to major faults produce statistically different *K* values by comparing mean *K* from basins at certain intervals of distance to major faults. We examine the intervals of distance from 10 km to 40 km with a 5 km increment. Due to the limited number of samples, all basins (n =111), small basins with $A < 200$ km^2 (n = 95), and small basins composed of 50% (n = 56) siliciclastic sedimentary have more than 10 samples in 10-km-distance groups (e.g., 0 – 10 km, 10 – 20 km) whereas the other basin groups (those grouped by other lithologies) do not. With a 10 km interval, statistically different mean *K* values are observed between 0 – 10 km and 10 – 20 km for small basins composed of 50% siliciclastic sedimentary rock. With an interval of 15 km, all basins, small basins with $A < 200$ km^2, and the small basins composed of 50% siliciclastic sedimentary show statistically different mean *K* values between 0 – 15 km and 15 – 30 km and similar *K* values between 15 – 30 km and 30 – 45 km. These three basin groups show statistically different mean *K* values consistently when examining the intervals of distance from 15 km (e.g., 0 – 15 km vs 15 – 30 km) to 40 km (e.g., 0 – 40 km vs 40 – 80 km). This is likely due to the fact that 74% of *K* values higher than 1.5×10^{-6} m$^{0.1}$ yr^{-1} are within ~15 km of major faults. Thus, we use 15 km as the cut-off to examine the impact of distance to major faults on *K*.

Based on this 15 km distance, we perform a second 2-sample *t*-test for *K* values from basins within 15 km ($D_{mf} \leq 15$ km) and greater than 15 km ($D_{mf} > 15$ km) from major faults. We found that mean

K from basins with $D_{mf} \leq 15$ km are ~2 times higher than those with $D_{mf} > 15$ km (Tables S8 and S9). Increased mean K is also observed in five basin groups between basins $D_{mf} > 15$ km and $D_{mf} \leq 15$ km, including all basins (1.9 ± 0.3 (2 s.d.) times), small basins (1.7 ± 0.4 times), and small basins dominated by siliciclastic sedimentary (2.3 ± 0.6 times), mixed composition sedimentary (1.6 ± 0.8 times), and plutonic rocks (1.9 ± 1.0 times) (Fig. 2.3). In addition, both the all basins and small basins with $A < 200$ km^2 groupings have statistically significant higher (1.5 to 1.8 times) K values for $D_{mf} \leq 15$ km compared to those with $D_{mf} > 15$ km when considering (1) basins sampled before 2008 and (2) basins sampled before 2008 or sampled after the 2008 Wenchuan earthquake outside of the 2008 Wenchuan earthquake severe shaking area ($PGA < 0.34$ g) (Table S9). This is consistent with observations that do not consider the 2008 Wenchuan earthquake, which implies the observed impact of D_{mf} on K was not due to the bias from samples affected by coseismic landslides from the 2008 Wenchuan earthquake.

Interestingly, we find that mean K from basins with $D_{mf} \leq 15$ km are higher for basins dominated by siliciclastic sedimentary rock (*ss*) than those dominated by plutonic rocks (*p*). However, there are no differences in mean K between basins with $A < 200$ km^2 and $D_{mf} > 15$ km dominated by different lithologic groups including siliciclastic sedimentary (*ss*), mixed composition (*mx*), and plutonic (*p*) rock. This indicates that fault damage in eastern Tibet may potentially induce differences in K depending on lithology with sedimentary rocks experiencing greater fault damage than plutonic rocks.

Lastly, we used an F-test to test whether the model prediction between erosion rates (E) and channel steepness (k_{sn}) is improved when considering (1) different groups of lithology, (2) distance to major faults, and (3) both. Based on equation 3 and n =1, we considered the reduced model of $E = K \cdot k_{sn}$ assuming a single erosion coefficient K. We examined whether the model with more

variables (e.g., distance to major faults, lithologies) had a statistically significant improvement compared to the reduced model (Snedecor and Cochran, 1989; Young and Hilley, 2018). The *F*-statistic for comparing the models is calculated with the following equation:

$$F = \frac{\frac{SSE_1 - SSE_2}{df_1 - df_2}}{\frac{SSE_2}{df_2}} \tag{2.7}$$

where SSE is the sum of squared errors and *df* is the degrees of freedom. The subscript 1 and 2 represent the reduced and full model, respectively. The p-values were determined using the numerator degrees of freedom ($df_1 - df_2$) and the denominator degrees of freedom (df_2). If the *p*-value of the *F*-statistic ($F_{df_1 - df_2, df_2}$) is less than 0.05, we can assume that the full model is a statistically significant improvement compared to reduced model.

First, we compared the reduced model with the full model with different *K* values from basins dominated by different lithologic groups. We used basins with A < 200 km^2 dominated by siliciclastic sedimentary (*ss*), mixed composition sedimentary (*mx*), and plutonic (*p*) rock. In this case, the full model with different lithologic groups does not show a significant improvement compared to the reduced model of a single *K* for those basins ($F_{2,82}$ = 0.61 with *p*-value=0.55). Second, we compared the reduced model of a single *K* with the full model with *K* that linearly varies with distance to the major faults, *D*, (e.g., $E = (K_1 \cdot D + K_2) \cdot k_{sn}$). In this case, the full model considering *D* shows a statistically significant improvement compared to the reduced model ($F_{1,83}$ = 9.14 with *p*-value = 3×10^{-3}). Third, we evaluated the reduced model in which *K* linearly varies with *D* compared to the full model in which the variations of *K* with *D* are different for each lithologic group (e.g., $E = (K_{i1} \cdot D + K_{i2}) \cdot k_{sn}$ where *i* = *ss, mx,* and *p*). We find no statistically significant improvements for these groups ($F_{4,79}$ = 1.87 with *p*-value = 0.12). In summary, the model prediction between erosion rates (E) and channel steepness (k_{sn}) is significantly improved

when we consider K varying with distance to major faults. However, the model prediction is not improved when we consider K varying with different lithologic groups (plutonic, siliciclastic sedimentary, and mixed composition sedimentary rocks) or with fault distance separately for different lithologic groups. The lack of model improvement for different lithologic groups may imply that the impact of fault damage is more pronounced than lithologic variations in eastern Tibet. In fact, according to *t*-tests in the previous section, K from different lithologic groups are similar to each other at D_{mf} >15 km. Within D_{mf} of 15 km, K from basins dominated by plutonic and siliciclastic sedimentary rocks differ. However, the small number of plutonic rocks may preclude a significant impact on the *F*-test.

In summary, the results of statistical analyses including observed significant, inverse correlations between distance to major faults and various erosion coefficients, statistically different mean K between basins less than and greater than 15 km from major faults, and a statistically improved model of erosion rates considering channel steepness (k_{sn}) and distance to major faults (D_{mf}), indicate the robust impact of fault damage on erosion and topography in eastern Tibet.

2.9 Figures

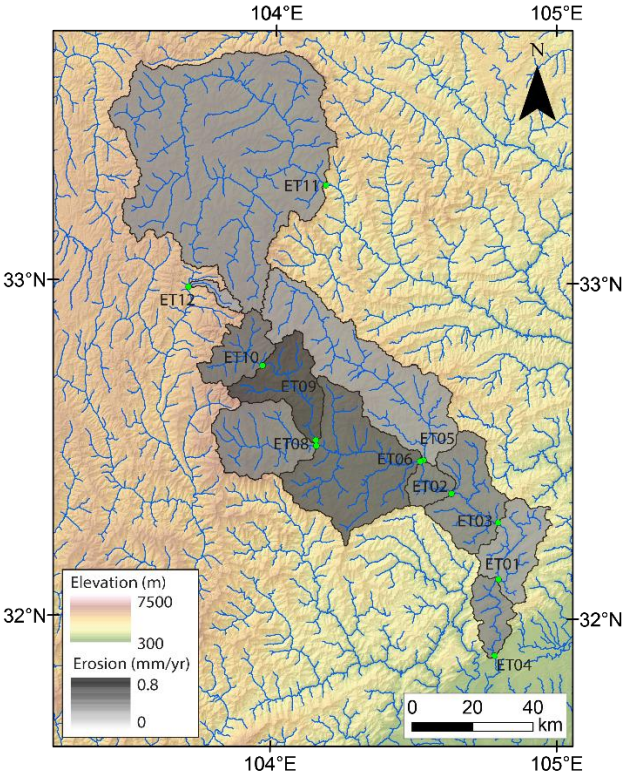

Figure 2.4. Elevation map of the Min Shan area with the 11 new sample collection sites and basin outlines from this study. Sample names are shown in black, channel networks are shown in blue, and sample collection sites are shown with green dots. Note that all samples except for ET05, 08, 10-12 have nested basins. Erosion rates from basins which are not from nested basins are shown on top of those which are from nested basins.

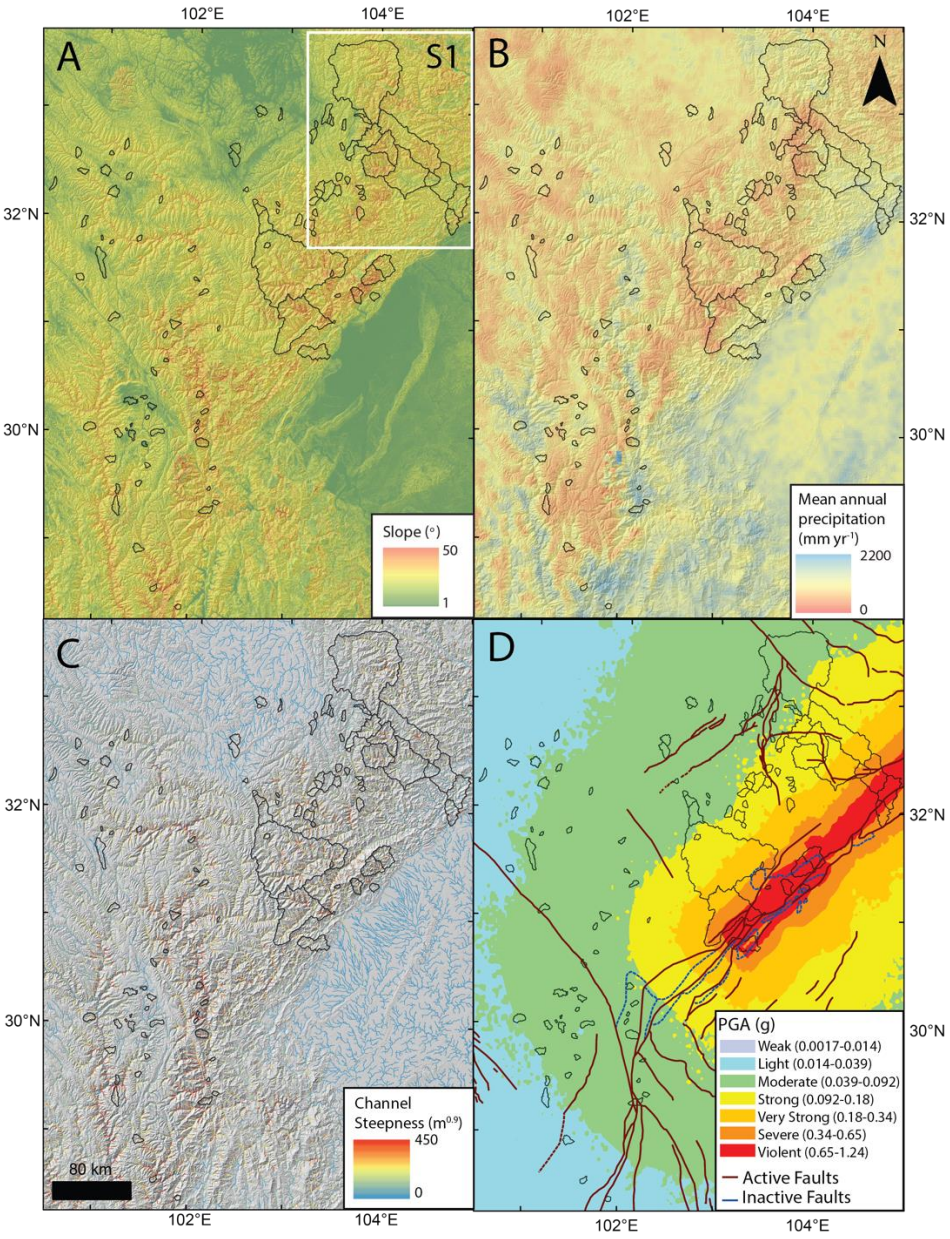

Figure 2.5. Maps showing (A) slope, (B) mean annual precipitation from Bookhagen and Burbank (2010), and (C) channel steepness shown for channel sections with drainage areas larger than 10 km^2 in eastern Tibet, and (D) peak ground acceleration (*PGA*) from the 2008 Wenchuan earthquake (from USGS ShakeMap v4). Black outlines represent all basins compiled from previous studies and measured in this study. A white box in (A) represents the area shown in Fig. 2.4.

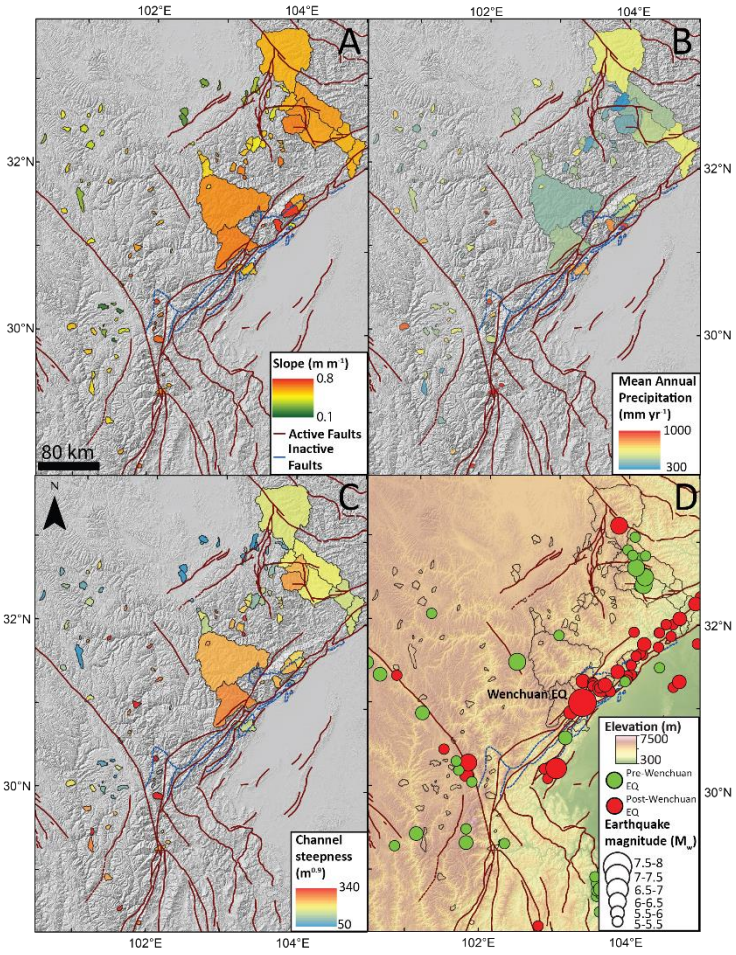

Figure 2.6. Maps showing basin-averaged (A) slope, (B) mean annual precipitation from Bookhagen and Burbank (2010), and (C) channel steepness from the integral method in eastern Tibet. (D) Elevation map with earthquakes from M_w 5 to 8 with larger circles showing higher magnitude earthquakes. Earthquakes before the 2008 Wenchuan earthquake are shown with green circles and those after the 2008 Wenchuan earthquake are shown with red circles. Earthquakes shown in the compilation occurred from 1970 through July 2018. Earthquakes were retrieved from www.iris.edu.

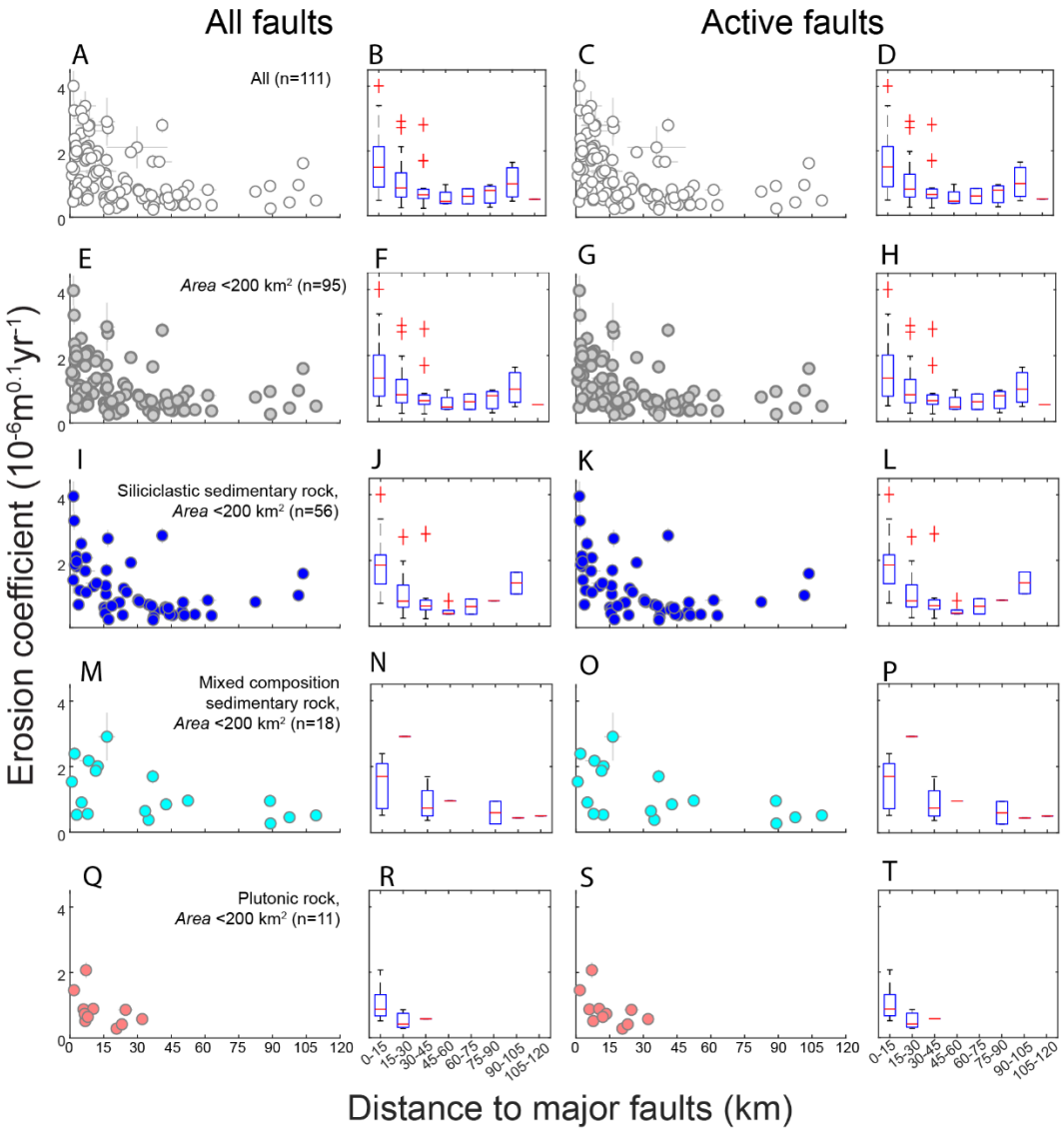

Figure 2.7. Scatter plots (A, C, E, G, I, K, M, O, Q, S) and box plots (B, D, F, H, J, L, N, P, R, T) showing how erosion coefficients vary with (A, B, E, F, I, J, M, N, Q, R) the distance to major faults and (C, D, G, H, K, L, O, P, S, T) distance to major active faults for A-D) all basins, E-H) small basins with area < 200 km^2, and small basins dominated by I-L) siliciclastic sedimentary rock, M-P) mixed composition sedimentary rock, and Q-T) plutonic rock. All basins, small basins, and small basins dominated by siliciclastic sedimentary, mixed composition sedimentary, and plutonic rocks are shown in circles with white, gray, blue, cyan, and salmon colors, respectively

in the scatter plots. The top and bottom of the blue sides of the box plots show the 25^{th} and 75^{th} percentiles, respectively. The central red mark in the box shows the median. The whiskers show the extent of data within 99.3%, and red crosses show outliers.

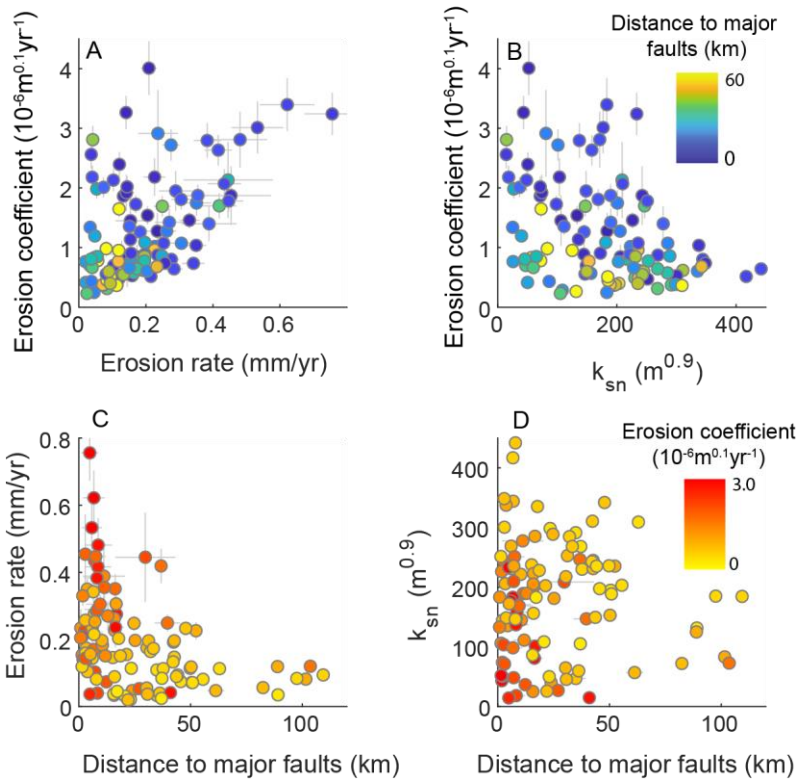

Figure 2.8. Scatter plots showing erosion coefficient vs. (A) erosion rate and (B) channel steepness (k_{sn}), color-coded for distance to major faults, and distance to major faults vs (C) erosion rate and (D) channel steepness (k_{sn}), color-coded for erosion coefficient. The control of distance to major faults on erosion coefficients is observed in a wide range of erosion rates and k_{sn} values.

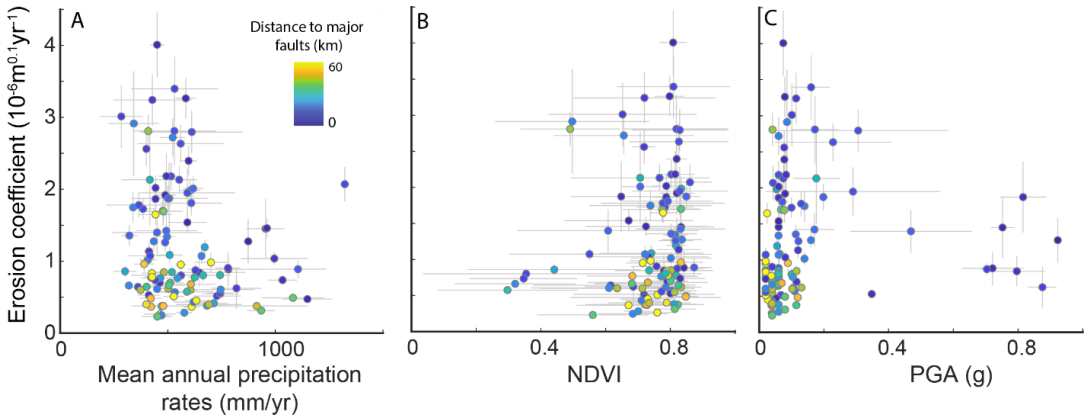

Figure 2.9. Relationships between basin-averaged erosion coefficient and (A) basin-averaged mean annual precipitation rates, (B) basin-averaged *NDVI*, and (C) peak ground acceleration (*PGA*) from the 2008 Wenchuan earthquake from all basins in this study. The colors represent distance to major faults.

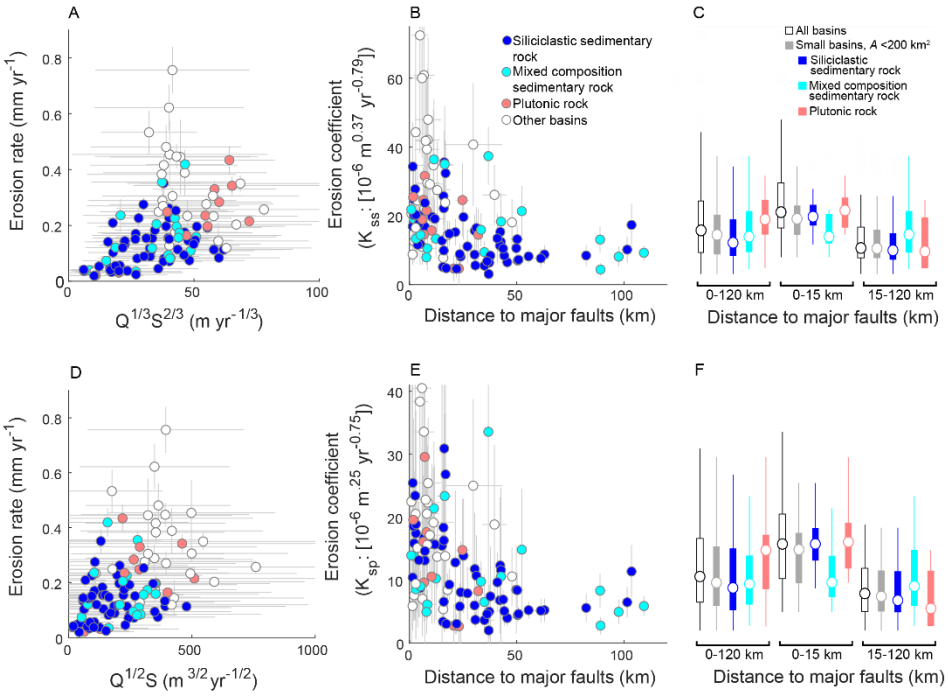

Figure 2.10. Plots of (A, D) erosion rates vs. the product of discharge and slope and (B,C,E,F) erosion coefficients vs. distance to major faults, color-coded for small basins dominated by different lithologic groups. Erosion coefficients K_{ss} and K_{sp} are based on river incision models assuming A-C) shear stress and D-F) stream power, respectively. Symbols are the same as in Fig. 2.3.

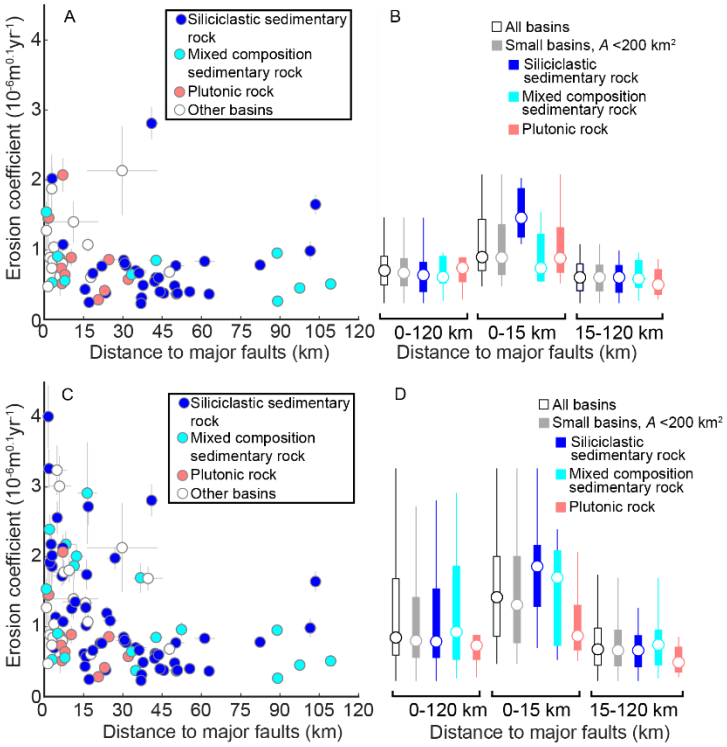

Figure 2.11. A,C) Erosion coefficient versus distance to major faults, color-coded for small basins dominated by different lithologic groups. B,D) Boxplots showing erosion coefficient ranges from different lithologies separated by distances to major faults. The plots show results from A,B) samples collected before the 2008 Wenchuan earthquake and C,D) samples collected before and after the 2008 Wenchuan earthquake but outside of the severe shaking range (*PGA* < 0.34 g). Symbols are the same as in Fig. 2.3. In both cases, we see that both the all basins grouping and the small basins grouping for $D_{mf} \leq 15$ km have ~1.5 to 1.8 times higher erosion coefficients than those basins with $D_{mf} > 15$ km.

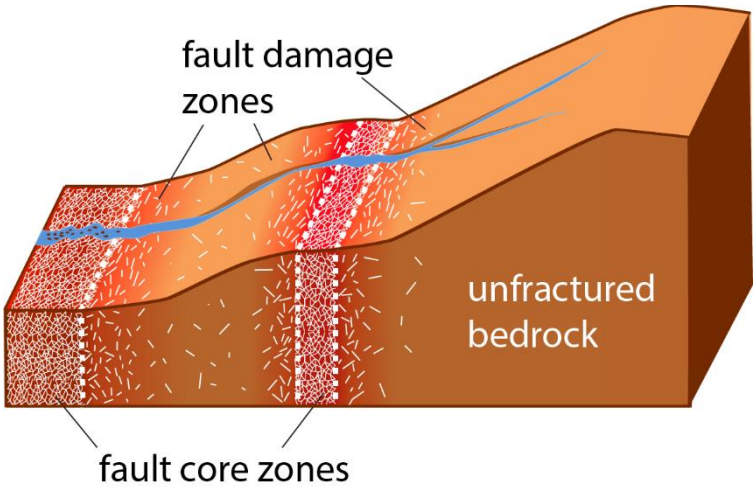

Figure 2.12. Conceptual diagram of fault core and damage zones and idealized topographic expression. Rock strength increase from fault core zones (e.g., gauge, cataclasite) to fault damage zones (e.g., jointed or fractured rocks) to unfractured intact bedrock. The topographic slope near the fault zone is gentler due to greater rock damage. Map not to scale.

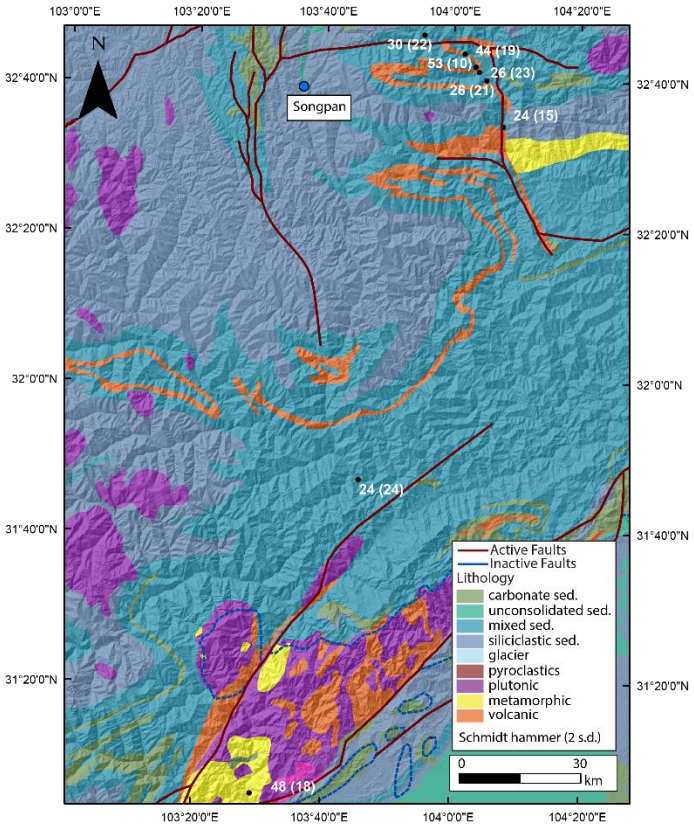

Figure 2.13. Lithology of the northeastern Longmen Shan and Min Shan area (Hartmann and Moosdorf, 2012) with the locations of Schmidt hammer measurements shown in black dots. The numbers in white are the average Schmidt hammer rebound values, and those in parenthesis show two standard deviation values. Brown lines show the active faults and blue lines shown inactive faults compiled in this study. The blue dot shows the location of the city of Songpan.

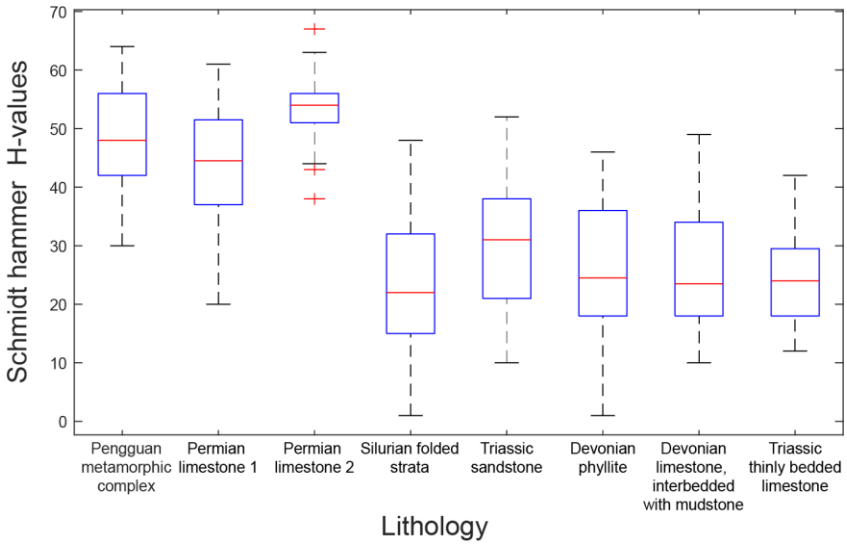

Figure 2.14. Boxplots showing the ranges of Schmidt hammer rebound values (*H*-values) for 8 sites. The top and bottom of the blue sides of the box show the 25th and 75th percentiles, respectively. The central red mark shows the median. The whiskers show the extent of data within 99.3%, and red crosses show outliers.

2.10 References:

Bookhagen, B, and Burbank, D.W., 2010, Toward a complete Himalyan hydrologic budget: Spatiotemporal distribution of snowmelt and rainfall and their impact on river discharge: Journal of Geophysical Research, 115, F03019, p. 1-25, doi:10.1029/2009JF001426.

Hartmann, J. and Moosdorf, N., 2012, The new global lithological map database GLiM: A representation of rock properties at the Earth surface: Geochemistry, Geophysics, Geosystems, 13, no. 12, p. 1–37.

Kirby, E. and Ouimet, W.B., 2011, Tectonic geomorphology along the eastern margin of Tibet: insights into the pattern and processes of active deformation adjacent to the Sichuan Basin: Geological Society, London, Special Publications, 353, no. 1, p.165–188, doi:10.1144/SP353.9.

Ouimet, W.B., Whipple, K.X., and Granger, D.E., 2009. Beyond threshold hillslopes: Channel adjustment to base-level fall in tectonically active mountain ranges: Geology, 37, no. 7, p. 579–582, doi: 10.1130/G30013A.1.

Portenga, E.W., and Bierman, P.R., 2011, Understanding Earth's eroding surface with 10Be: GSA Today, 21, no. 8, p. 4-10.

Scherler, D., Dibiase, R.A., Fisher, G.B., and Avouac, J.-P., 2017, Testing monsoonal controls on bedrock river incision in the Himalaya and Eastern Tibet with a stochastic-threshold stream power model: Journal of Geophysical Research: Earth Surface, 122, p. 1389–1429, doi:10.1002/2016JF004011.

U.S. Geological Survey, 2017, ShakeMap – Earthquake Ground Motion and Shaking Intensity Maps: U.S. Geological Survey, doi: 10.5066/F7W957B2.

Whipple, K.X. and Tucker, G.E., 1999, Dynamics of the stream-power river incision model: Implications for height limits of mountain ranges, landscape response timescales, and research needs: Journal of Geophysical Research, 104, no. B8, p. 17661-17674.

Finlayson, D.P., Montgomery, D.R., Hallet, B., 2002. Spatial coincidence of rapid inferred erosion with young metamorphic massifs in the Himalayas: Geology, 30, no. 3, p. 219-222.

Montgomergy, D.R., and Brandon, M.T., 2002. Topographic controls on erosion rates in tectonically active mountain ranges: Earth and Planetary Science Letters, 201, p. 481-489.

Perron, J.T. and Royden, L., 2013, An integral approach to bedrock river profile analysis: Earth Surface Processes and Landforms, 38, p.570–576, doi: 10.1002/esp.3302.

Snedecor, G.W. and Cochran, W.G., 1989, Statistical Methods: Ames, Iowa, Iowa State University Press.

Wobus, C., Whipple, K.X., Kirby, E., Snyder, N., Johnson, J., Spyropolou, K., Crosby, B., and Sheehan, D., 2006, Tectonics from topography: Procedures, promise,and pitfalls, in Willett, S.D., Hovius, N., Brandon, M.T., and Fisher, D.M., eds., Tectonics, Climate, and Landscape Evolution: Geological Society of America Special Paper 398, Penrose Conference Series, p. 55–74, doi: 10.1130/2006.2398(04).

Young, H.H., and Hilley, G.E., 2018, -scale denudation rates of the Santa Lucia Mountains, California: Implications for landscape evolution in steep, high-relief, coastal mountain

ranges: Geological Society of America Bulleti130, no. 11-12, p. 1809-1824. doi:10.1130/B31907.1.

Appendix B for Chapter 3: Temperature and co-crystallization effects on Zr isotopes: A case study of the La Posta igneous complex

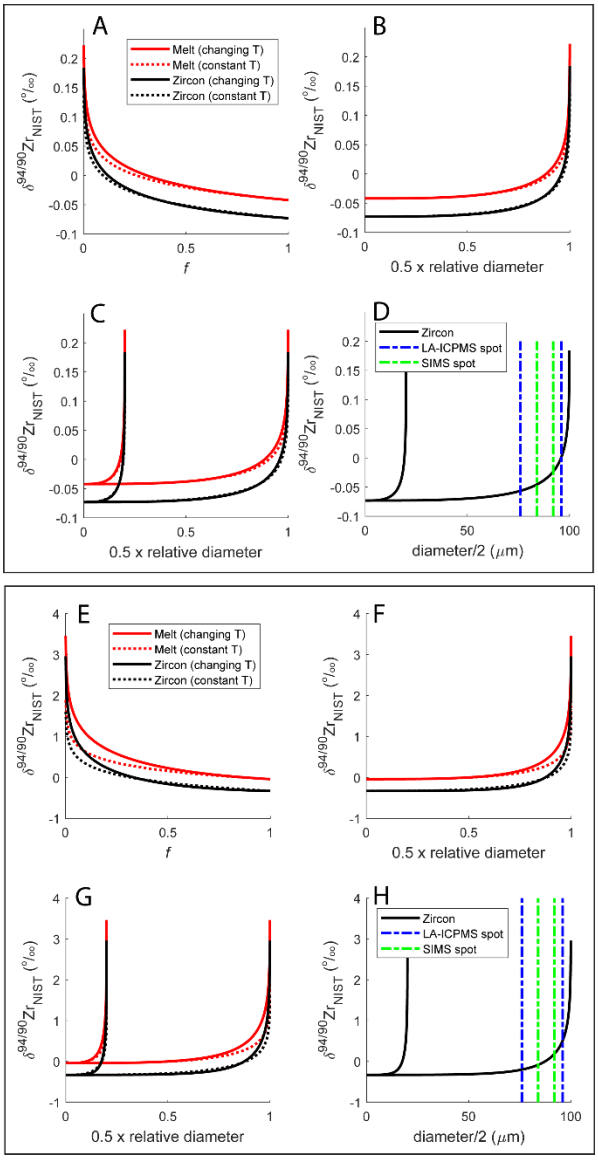

Figure 3.15: A-D show relationships as modeled using force constants calculated in Méheut et al. (2021); E-H show relationships modeled using the temperature regression shown in Guo et al. (2020); A, B, C. E, F, G) Modeled zircon isotope profiles showing the impacts of constant vs. changing T on Zr isotope evolution for a tabular zircon that we model as a rectangle. B and F) shows a system where all three zircon axis are the same length (x = y = z) and C and G) shows a

system where x = y and z= 5x. D and H) shows a grain where z = 200 μm and x = y = 40 μm along with the approximate size of LA-ICPMS and SIMS beams in blue and green, respectively. Red and black lines show the isotopic composition of melt and zircon, respectively and solid and dotted lines show the isotopic trajectory of a system with a constantly changing T and an isothermal system, respectively.

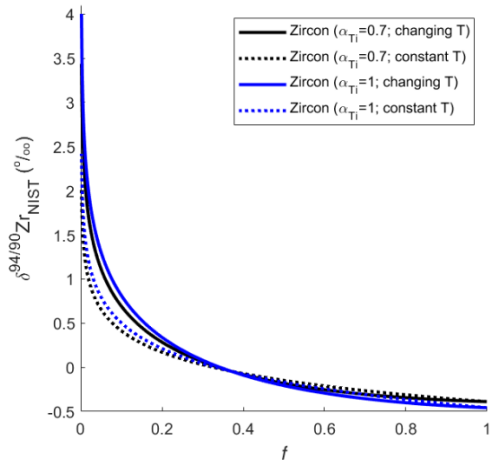

Figure 3.16: Fraction of Zr remaining (f) vs. $\delta^{94/90}$Zr (‰) for a modeled zircon where α_{Ti}=0.7 (black) and α_{Ti}=1.0 (blue) for constant (solid lines) vs. a constantly changing T (dot-dash lines).

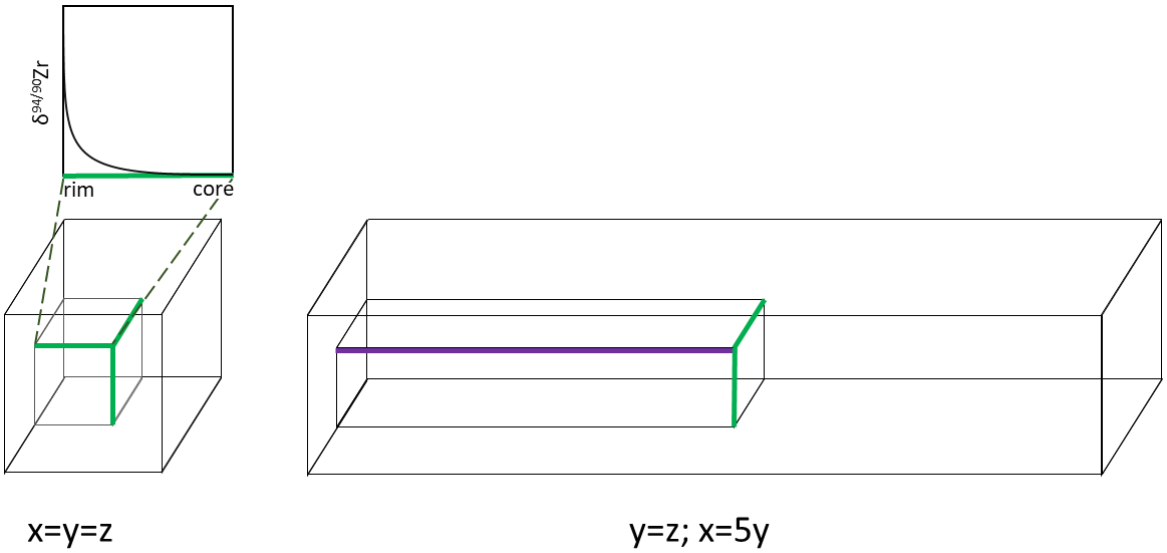

Figure 3.17: A physical model showing the two geometries of our hypothetical crystals.

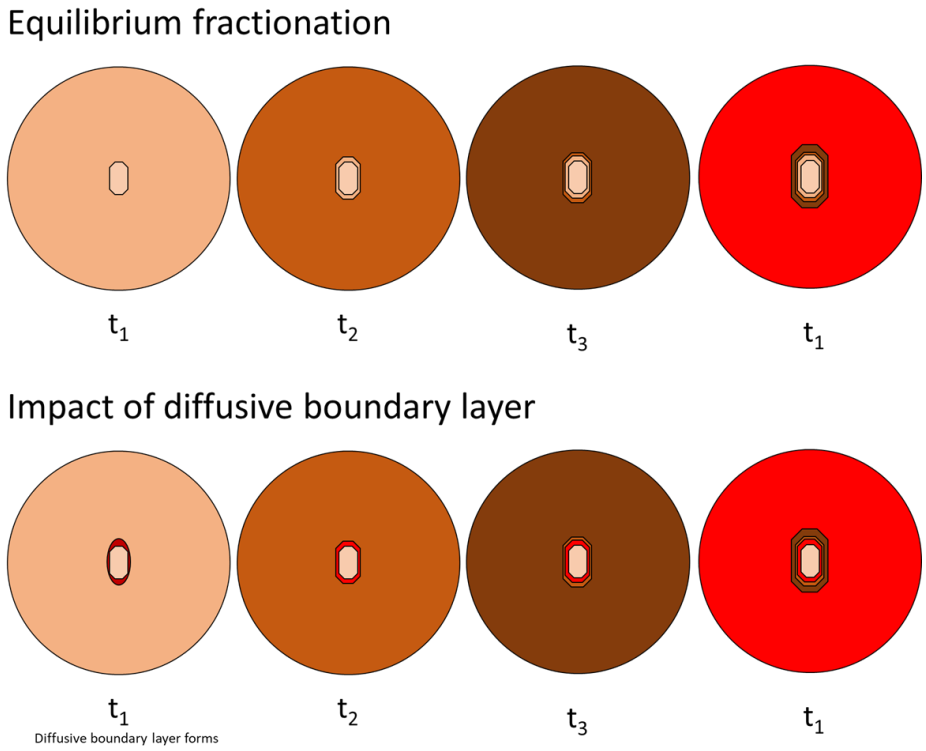

Figure 3.18: Schematic showing the impact of a diffusive boundary layer forming on crystal composition.